



Journal of Electromagnetic Analysis and Applications

ISSN: 1942-0730 (Print), 1942-0749 (Online)

Volume 2, Number 3, March 2010

www.scirp.org/journal/jemaa



Scientific
Research

JOURNAL EDITORIAL BOARD

ISSN: 1942-0730 (Print) 1942-0749 (Online)

<http://www.scirp.org/journal/jemaa>

Editors-in-Chief

Prof. James L. Drewniak University of Missouri-Rolla, USA

Prof. Yuanzhang Sun Wuhan University, China

Editorial Board

Dr. Mazen Abd El-Salam Assiut University, Egypt

Dr. Michail B. Belonenko Laboratory of Nanotechnologies, Volgograd Institute of Business, Russia

Dr. Boguslaw Butrylo Bialystok Technical University, Poland

Dr. Xijiang Han Harbin Institute of Technology, China

Dr. Eisuke Hanada Division of Medical Informatics, Shimane University Hospital, Japan

Dr. Isabel Jesus Institute of Engineering of Porto, Portugal

Dr. Ozlem Ozgun Middle East Technical University, Turkey

Prof. M. Ramamoorthy University of British Columbia, Canada

Dr. Jiangjun Ruan School of Electrical Engineering, Wuhan University, China

Dr. Yinbiao Shu Executive vice president of State Grid, China

Prof. Yonghua Song Tsinghua University, China

Prof. Felix Wu University of Hong Kong, China

Prof. Ryuichi Yokoyama Waseda University, Japan

Dr. Ben Young The University of Hong Kong, China

Dr. Wenhua Yu Pennsylvania State University University, USA

Dr. Jun Zou Zhejiang University, China

Dr. Yuchun Guo Xidian University, China

Dr. Abbasali Lotfi Iranian Research Institute for Electrical Engineering, Iran

Prof. Francisco Torrens Universitat of Valencia, Spain

Editorial Assistants

Zhenhua Sun Jemaa@scirp. org

Dao-Chun Huang Wuhan University, China

Guest Reviewers

Greeneche Jean-Marc
Ding Jun
Yongle Wu
HoonJae Lee
Isamu Watanabe
José Vicente Canto dos Santos
Yanyan Luo
Yanfei Wang
Marina Chukalina
Jyri Leskinen
Ivan Gerace
Han Zheng

Shen Chen
Josiah Munda
Alhabib Binkou
Pablo Gómez
Elisa Francomano
Zhenbao Ye
Jose Alfredo Tirado-Mendez
Isabelle Huynen
Rong-Fong Fung
M Alrashidi
Juan M. Ramirez
A. Rabiee

Amel Boufrioua
Metin Demirtas
Vitor Pires
Tine Marčič
Sedat Sunter
Jan Rusek
Pietro Prestininzi
Neville Dubash
Hussein. D. Al-Majali
Gilsoo Jang
Chi-Hshiung Lin
Tianyuan Tan

Shenghu Li
HamidReza Karami
Lin Li
Lars Magnus Hvattum
Yansong Wang
Man Weishi
Douglas.A.G.Vieira
Wiwat Tippachon
Jorge Pereira
Jamshid Aghaei
Célia de Jesus

TABLE OF CONTENTS

Volume 2 Number 3

March 2010

A Microwave-Based Invisible “Watermarking” Emulated by an Embedded Set of Electromagnetic Material in a Plastic Card

P. Neelakanta, S.-H. Lim.....121

The Additional Criterion for the Determination of the Time of Minimum of a Solar Cycle

H. I. Abdussamatov.....128

Modeling of the Earth’s Planetary Heat Balance with Electrical Circuit Analogy

H. I. Abdussamatov, A. I. Bogoyavlenskii, S. I. Khankov, Y. V. Lapovok.....133

Analysis of the Electromagnetic Pollution for a Pilot Region in Turkey

Ö. Genç, M. Bayrak, E. Yaldiz.....139

Modeling of Multi-Pulse VSC Based SSSC and STATCOM

P. Zuniga-Haro, J. M. Ramirez.....145

A Fundamental Equation of Thermodynamics that Embraces Electrical and Magnetic Potentials

S. Abdel-Hady.....162

Energy and Momentum Considerations in an Ideal Solenoid

S. M. AL-Jaber.....169

Exact Solutions of Equations for the Strongly-Conductive and Weakly-Conductive Magnetic Fluid Flow in a Horizontal Rectangular Channel

M. J. Li, X. R. Zhang, H. Yamaguchi.....174

A New Analysis Method for Locating the Focus and for Estimating the Size of the Focus of the Backscatter Light of a LIDAR System

N. W. Cao, W. Y. Wang, Y. H. Wu, F. Moshary, Z. R. Chen, J. S. Huang.....183

Design of the Control System about Central Signals in Electric Vehicle

Q. Q. Zhang, Y. Wang, T. M. Yin.....189

Journal of Electromagnetic Analysis and Applications (JEMAA)

Journal Information

SUBSCRIPTIONS

The *Journal of Electromagnetic Analysis and Applications* (Online at Scientific Research Publishing, www.SciRP.org) is published monthly by Scientific Research Publishing, Inc., USA.

Subscription rates:

Print: \$50 per issue.

To subscribe, please contact Journals Subscriptions Department, E-mail: sub@scirp.org

SERVICES

Advertisements

Advertisement Sales Department, E-mail: service@scirp.org

Reprints (minimum quantity 100 copies)

Reprints Co-ordinator, Scientific Research Publishing, Inc., USA.

E-mail: sub@scirp.org

COPYRIGHT

Copyright©2010 Scientific Research Publishing, Inc.

All Rights Reserved. No part of this publication may be reproduced, stored in a retrieval system, or transmitted, in any form or by any means, electronic, mechanical, photocopying, recording, scanning or otherwise, except as described below, without the permission in writing of the Publisher.

Copying of articles is not permitted except for personal and internal use, to the extent permitted by national copyright law, or under the terms of a license issued by the national Reproduction Rights Organization.

Requests for permission for other kinds of copying, such as copying for general distribution, for advertising or promotional purposes, for creating new collective works or for resale, and other enquiries should be addressed to the Publisher.

Statements and opinions expressed in the articles and communications are those of the individual contributors and not the statements and opinion of Scientific Research Publishing, Inc. We assume no responsibility or liability for any damage or injury to persons or property arising out of the use of any materials, instructions, methods or ideas contained herein. We expressly disclaim any implied warranties of merchantability or fitness for a particular purpose. If expert assistance is required, the services of a competent professional person should be sought.

PRODUCTION INFORMATION

For manuscripts that have been accepted for publication, please contact:

E-mail: jemaa@scirp.org

A Microwave-Based Invisible “Watermarking” Emulated by an Embedded Set of Electromagnetic Material in a Plastic Card

Perambur Neelakanta, Swee-Hock Lim

Department of Computer and Electrical Engineering and Computer Science, Florida Atlantic University, Boca Raton, USA.
Email: neelakan@fau.edu

Received November 25th, 2009; revised December 18th, 2009; accepted December 22nd, 2009.

ABSTRACT

This article describes a passive, economical strategy towards enhancing the security feature of conventional plastic cards by embedding a set of electromagnetic (EM) material that emulates an invisible “watermarking”. This is an overlay strategy to prevailing security measures and consists of incorporating (invisibly embedding, say by ink-jet printing or otherwise) a set of foil/film-like grids of electromagnetic (EM) material (such as high- μ material or high-conductivity metal) within the cross-section of the card. The test-card when exposed to a suitable excitation of microwave (ISM band) excitation, the embedment of EM material in the card is rendered to yield distinct path-loss to the traversing EM energy. That is, by making each element of embedment a grid-frame made of vertical or set of horizontal strips, (relative to the plane of polarization of EM excitation), each grid-frame will offer high (logic 1) or low (logic 0) transmissions when the card is swiped across the EM field. By sensing appropriately, this differentiable EM attenuation across the card would depict an output signal announcing the presence of a binary-logic encoding in the embedded “watermarking”. The proposed effort augments the existing security features of a plastic card design and robustly reduces the chances of malpractices, such as plastic card counterfeiting and misuse. The concept-design as proposed is positively verified through experimental test cards and also justified with theoretical considerations.

Keywords: Microwave-Based Watermarking, Plastic Cards, Electromagnetic Materials

1. Introduction

As well known, the plastic card is mostly used as a secured entity by individuals as personal identity (ID) cards/driver’s license as well as in business transactions. But, this security-featured card often becomes susceptible for counterfeiting and unauthorized copying, scanning and photo-imaging. Therefore, provisioning extra security features as an overlay effort in such cards is imminent and complements the dynamic needs of broad customer base.

Ideally a security feature incorporated in a plastic card should enable immediate onsite verification and prevent unauthorized authentication, duplication or forgeries. Existing designs towards security embedment in plastic cards include card personalization by thermal-imaging, holographic imprints, bar-coding, embossing, magnetic-stripe encoding and provisioning smart-card (chip-card) capabilities. The existing standard (ISO 7810) ensures the integrity and security of the card, with the performance to an acceptable level.

Yet another, security enhancement is proposed here (as an overlay technique to the prevailing security features) that offers a value-added two levels of authenticity to the customers. It is based on a simple, cost-effective technology using microwave principles. It consists of incorporating (invisibly embedding/burying) a set of electromagnetic (EM) material [1] (such as high- μ or good-conductivity material) in foil/film-like (or ink-jet printed [2] form of) grid-frames. This embedment enables two-levels of security as follows:

When the test card is exposed to a suitable high-frequency electromagnetic (EM) excitation, the very presence of EM material offers a preset (threshold) of attenuation and hence the detected microwave strategy declares the presence of the embedded material confirming the first-level of authentication. Further, the embedded EM material (structured as an array of grid-frames) is rendered to yield a distinct attenuation (power loss) to the EM energy traversing each frame when the card is swept. The distinct attenuation refers to realizing two-levels (of

high or low); and, it is accomplished with the grid design/structure having horizontal or vertical strips relative to the linear polarization of the EM excitation. The array of such vertical or horizontal grids would cause high or low attenuations to the EM wave. Sensing differential (high/low) level-changing corresponds to emulating a "watermarking" of a binary encoding of a logical (0, 1) signature. Thus, 1) by threshold-based, yes/no detection of embedded EM material and 2) by decoding the logical signature improvised by the array of grid structures of the EM material embedment, a two-prong enhancement on card identification/authenticity is realized.

Relevant concept-description, analysis, EM (microwave) excitation/sensor details, construction of a test-unit and testing are described below. Further, results are furnished towards the proof-of-the-concept. Suggested EM excitation conforms to the use of ISM 2450 MHz frequency [3]; and, the associated electromagnetics plus system considerations can be rendered not to interfere with the existing infrastructure on magnetic-core, chip-card and/or bar-code reading efforts. The proposed strategy of card authentication can be included as a part of existing/traditional card-swiping unit.

2. Embedding Information in Secured Plastic Cards: State-of-the-Art

The plastic card is a portable, wallet-size entity with embedded information and has been ushered into the society in various day-to-day applications where on-site card data retrieval is facilitated and security is implied. The generic versions of plastic cards in vogue can be listed as follows: 1) Magnetic stripe cards (ISO 7810 and ISO 7811) where data is stored in the magnetic stripe by modifying the magnetism of tiny iron-based magnetic particles placed/smeared as a band (on the magnetic stripe); 2) smart cards (ISO 7816) (also known as a chip card, or an integrated circuit card) is a critically secured card intended for financial, information technology (computer and/or communication access), government, healthcare, ID on Internet applications etc.; 3) bar-coded cards bearing bar coded information are used for simple ID as in library cards; and 4) proximity cards containing an embedded antenna transmits encoded information as a radio frequency (RF) signal (at 125 kHz or 13.56 MHz) towards identification (RFID). Picking up the encoded RF signal proximally identifies the card.

2.1 Concept of "Digital Watermarking"

Another level of security can be added to the plastic cards with "watermark" design (visible or invisible) [4]. Such watermarking decreases the illegal reproduction of the card and prevents fraud. The watermarking on plastic cards is a customized effort. It involves posting exclu-

sively ID pictures and details printed on plastic cards. Such cards need specific digital decoding by the reader to authenticate the card. In essence, watermarking provides tamper-proofing. One popular watermarking method in use today is known as digital watermarking. The technique of digital watermarking takes its name from "watermarking" of paper or currency improvised as a security measure. Such a watermark feature is a slight imprint on paper that is nearly imperceptible unless viewed carefully, under proper conditions of optical visibility.

Digital watermarking processes involve the insertion and extraction of watermarks. In watermark insertion, the original object and a secret key are combined to produce a "stego object", which consists of the original object with a watermark embedded in it. Later, to show authenticity or ownership of the stego object, the secret key and the stego object are combined in the process of watermark extraction, which recovers and/or verifies the presence of the watermark.

Some common types of watermarks are: 1) Visible watermarks, which depict an extension of the concept of logos. Here logos are inlaid into the image transparently; 2) invisible watermark is hidden in the content and can be detected by an authorized agency only; 3) public watermark allows reading or retrieval by anyone using a specialized algorithm; 4) fragile watermark is a tamper-proof watermarks destroyed upon data manipulation; 5) private watermark (or secure watermark) can be read only with a secret key; 6) a perceptual watermark exploits the aspects of human sensory system so as to provide invisible yet robust watermark; and 7) the so-called bit-stream watermarking is realized with compressed data (such as video).

2.2 Can a Plastic Card be Rendered with "Watermarking"?

Indicated in [4], a method of supporting traditional way of watermarking on photographic images laid on plastic cards. Presently, a microwave/EM-material based technique of "watermarking" is suggested. It is indicated as an enhanced security feature to plastic cards and is conceived by improvising an invisible watermark that can be detected (and its content analyzed) only by a special card-reading mechanism involving a microwave approach. When a card is forged, inasmuch as the implemented watermarking is absent, the card will not be authenticated by the reader as a first-level of security. Further, by proper design of the embedment set of EM material (in terms of number, size variations, and orientation of embedded elements relative to EM polarization), a digital (binary) sequence can be improvised into the "watermarking"; and, an EM sensor-cum-reading mechanism will decode this data for authentication/verification as a second-level of security. This concept of placing an

EM-based watermarking in plastic cards is novel and new. To the best of the authors’ knowledge, no relevant study has been done.

3. EM Material-Based Watermarking in Plastic Cards: Test Card Details

In summary, the (invisible) “watermarking” envisaged here refers to provisioning the plastic card with a buried configuration of (embedded) EM material that reacts to microwave radiation. Towards feasibility, the test EM materials being considered include: 1) High- μ material and 2) good conducting metals (like copper and aluminum). These EM materials advocated are required to be made in the form of foil/film-like grids (constituted by vertical or horizontal grid-strips) or can also be formed into the required grid structure using the modern art of conductive ink-jet printing [2]. The proposed “watermarking” is to include a set of any of the aforesaid materials (of suitable dimensions, in numbers and orientations in grid form) as a layer embedded within the standard plastic card as shown in **Figure 1**.

Suppose at the time of card-swiping, the card is illuminated by a linearly-polarized EM field at a microwave frequency, say, the ISM-band 2450 MHz [3]. Inasmuch as the grid set of EM material would offer attenuation to the microwave transmission across the card, the presence of such test EM material while the card in swiping mode, can be sensed; and, the detected signal will annunciate the presence or absence of invisibly embedded material “watermarking” and provides a first-level of go/no-go confirmation on the authenticity of the card. In addition, by having the embedded EM material formatted as a set of horizontal or vertical strip grid-frames, the extent of attenuation caused by each grid-frame to the linearly polarized microwave transmission while swiping the card can provide a logic word (signature) of 1’s and 0’s of a binary encoding upon detection. Hence, the detected and encoded signal facilitates a second level of ID and authentication of the test-card. The card is excited by a microwave source as shown in **Figure 2**.

Referring to the system and test-card described as above, suppose d_p be the thickness of the plastic card and d_s is the thickness of the embedded material, (such that $d_s \ll d_p$). Assuming a simple plane wave excitation (at a wavelength $\lambda \gg d_p$ or d_s), the magnitude of power transmission coefficient across electrically-thin (that is, $d_p \ll \lambda$) window due to the test card can be written as [5]: $\tau^2 = 1 - |\rho|^2$ where, ρ is the voltage reflection coefficient at the surface of the plastic card, which can be deduced as:

$$|\rho| \approx \left| j \frac{2\pi}{\lambda_2} \left(\frac{1}{\sqrt{\epsilon_p}} - \frac{\sqrt{\epsilon_p}}{1} \right) \right| \quad (1)$$

where $\lambda_2 = c/\sqrt{\epsilon_p}f$ with ϵ_p being the dielectric constant of the plastic material and f is the frequency of EM excitation. When the embedded set of grid-frames comes in the EM excitation zone while swiping, ρ would get modified or perturbed. This perturbation can be specified in terms of power losses suffered by the EM wave passing through the plastic card and encountering the EM material, which is assumed of good conductivity/high- μ characteristics.

Also, the embedded grid-frames are of small size (area) in relation to the area of the plastic card and are electrically thin. Correspondingly, the modified (perturbed) value of τ^2 can be written as:

$$\tau_m^2 = K_s \left[1 - |\rho|^2 \right] \exp(-2\alpha_m d_m) \quad (2)$$

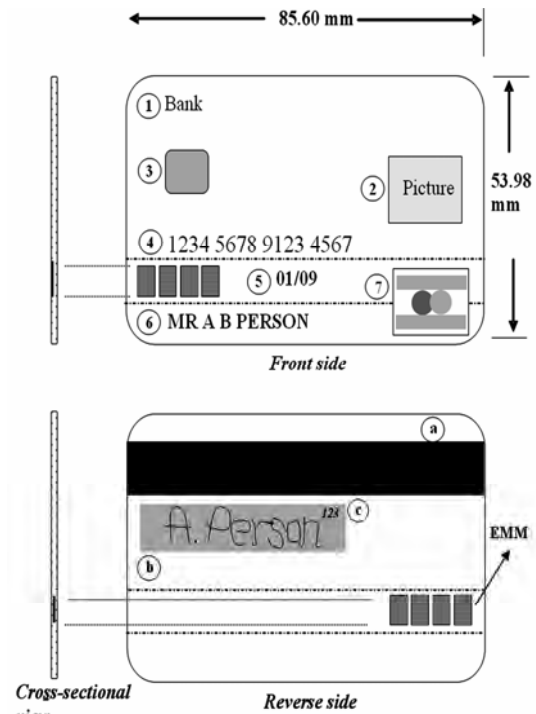


Figure 1. Embedding a set of frames of EM material in a standard plastic card. (EMM: Embedded EM material). Front side: 1) Issuing organization logo; 2) Hologram/photograph; 3) EMV (Europay MasterCard, Visa) chip; 4) Card number; 5) Expiry date; 6) Cardholder name; and 7) Card brand logo

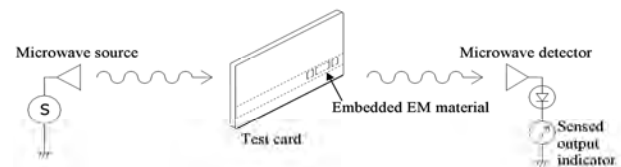


Figure 2. Excitation of the test card with microwave energy source

where the subscript m implies the embedment being present, α_m is the attenuation coefficient exclusively caused by the embedment and K_s is a scattering (power) loss coefficient due to the finite size of the embedded grid structure facing the EM radiation. Further, the attenuation coefficient (α_m) can be explicitly written as:

$$\alpha_m = \sqrt{\pi f \mu_o \mu_{rm} \sigma_m} \text{ nepers/meter} \quad (3)$$

with f being the frequency of microwave excitation in Hz. Further, μ_o is the free-space permeability ($4\pi \times 10^{-7}$ H/m) and μ_{rm} and σ_m S/m denote respectively, the relative permeability and the conductivity of the embedded material. Hence, it follows that:

$$\begin{aligned} \frac{\tau_m^2}{\tau^2} &= K_s \exp(-2\alpha d_m) \\ &= K_s \exp\left[\left(\sqrt{2\pi f \mu_o \mu_{rm} \sigma_m}\right) d_m\right] \end{aligned} \quad (4)$$

Therefore, in order to realize a good resolution of sensing the attenuation caused by the embedment (at a given frequency of operation), it is suggested to use a good conductivity plus high- μ characteristics material in making the embedded grid-frames.

Further, the embedment size (area = A_m) will implicitly decide the constant, K_s . That is, K_s is a function of A_m and d_m . The thickness (d_m) of the embedded grid-frames can be chosen almost film-like without significantly altering the thickness (d_p) of the plastic card, which is set by existing standards. Therefore, the value of A_m is a design parameter to be optimized.

3.1 Improvising Binary Encoding via Vertically/Horizontally Formatted Grid Structure of Embedded Material

As indicated before, suggested here a novel method of improvising a binary logic in the embedded set of EM material introduced within the plastic sheet. The method of approach is as follows: Each grid-frame is constructed with the test EM material in film/foil-like structure. It is taken in two forms: 1) A vertically-stacked stripes closely arranged to form a vertical grid structure as shown in **Figure 3(a)**; and 2) a horizontally- stacked stripes closely arranged to form a horizontal grid structure as shown in **Figure 3(b)**.

Further, a set of vertical and horizontal grid-frames of **Figure 3** can be embedded in the plastic sheet side-by-side so as to form a binary logic as illustrated in **Figure 4**.

Suppose the microwave excitation is set to a linear polarization, vertical (VP) or horizontal (HP). Then, the corresponding transmission coefficient of Equation (4) in the presence of a grid-frame gets modified as:

$$\tau_m^2 = K_s \left[1 - |\rho|^2\right] \exp\left[(-2\alpha_m d_m) \times s_{\parallel}\right] \quad (5)$$

Or,

$$\tau_m^2 = K_s \left[1 - |\rho|^2\right] \exp\left[(-2\alpha_m d_m) \times s_{\perp}\right] \quad (6)$$

Equation (5) applies to the transmission across the card when a vertically-polarized EM wave faces parallel grid structure and s_{\parallel} is the corresponding attenuating parameter. Likewise Equation (6) is valid when the same vertically-polarized EM wave traverses the card and faces the horizontal grid structure, which poses a corresponding attenuating parameter of s_{\perp} .

3.2 Designing and Testing a Concept Unit

Consistent with the concept described, different sets of test cards (of standard size as indicated in **Figure 1**) are designed and fabricated. These sets correspond to using different EM materials in making the grids. Specifically,

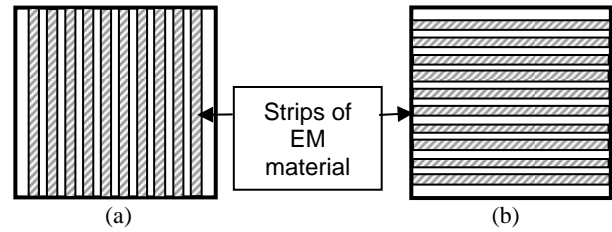


Figure 3. EM material conceived as film/foil of grid-frames for embedment in the plastic card. (a) Grid-frame of vertically-stacked strips and (b) Grid-frame of horizontally-stacked strips

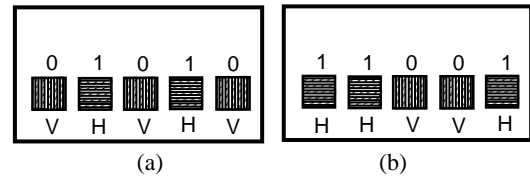


Figure 4. Emulation of a binary logic with vertical (V) and horizontal (H) grid-frames of EM material. Examples: (a) Logic 01010 and (b) Logic 11001

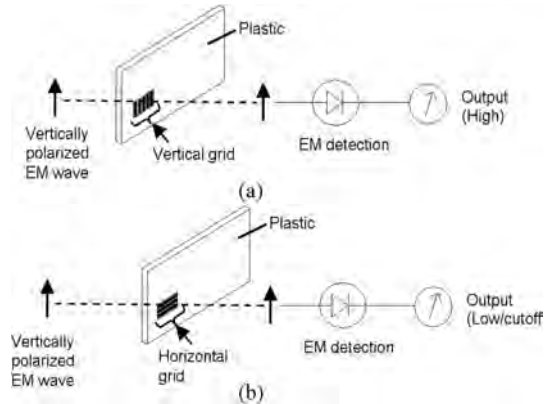


Figure 5. (a) High and (b) Low transmissions of a vertically-polarized EM wave traversing through vertical and horizontal grid structures, respectively

high- μ material and high-conductivity materials (copper and aluminum) are used.

The microwave setup illustrating the excitation of the test card and sensing the transmission coefficient are illustrated in **Figure 6**. As shown, the test card embedded with an EM material is illuminated with microwave radiation from a source and the corresponding transmission coefficient is measured. The recommended frequency for this operation is the license-free ISM band 2450 MHz. In the present study, however, for the purpose of demonstration a 10 GHz (X-band) source is used. But, relevant excitation/sensing considerations remain unaltered in using ISM 2450 MHz without any loss of generality.

Further illustrated in **Figure 7** (photograph) is a test card embedded with high- μ material grid-frames in alternate grid formats (of vertical and horizontal structures) set to form the logic of (1, 0, 1, 0).

4. Test Results: Measured Data on Sensed RF/Microwave Signals versus Test Cards Used

Different sets of test cards described earlier (having varying area of cross-sections with plain and grid-formatted structures) are subjected to testing. The measured results on microwave signal (power) attenuation due to the presence of embedded test EM materials *versus* the size of these materials are presented in **Tables 1** to **3**.

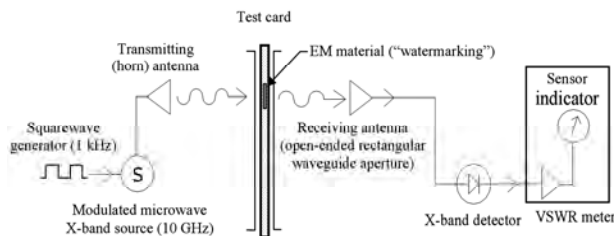


Figure 6. Laboratory set-up of microwave-plumbing for test card excitation and “watermarking” detection

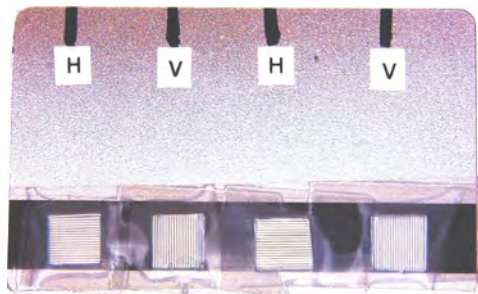


Figure 7. Photograph of the test card embedded with high- μ material in alternate grid formats (vertical and horizontal). H and V depict the (1, 0, 1, 0) logic expected with a vertically-polarized EM transmission (across a vertically-positioned test card being swiped)

5. Encoding-Improvised Test Card Using Grids with Vertical and Horizontal Strips

Next, a test card having a set of four high- μ grids of vertical and horizontal strips as shown in **Figure 8** is considered. Each grid frame used is dimensioned to be about $0.75 \text{ cm} \times 0.75 \text{ cm}$. As this card is swiped across the slot/groove, the measured microwave power level (in dB) depicting the encoding due to the embedded sheets are indicated in **Figure 8**.

6. Discussion and Closure

Referring to **Tables 1** to **3** and **Figure 8**, the following details can be inferred: As expected, the EM materials embedded in the plastic cards react differently to the EM excitation, by virtue of the associated conductivity and permeability characteristics. (See Equation (4)). In addition, vertical (V) or horizontal (H) formatted grids (of a given size) of the EM material embedment lead to distinguishable transmission response *vis-à-vis* the polarization of the microwave excitation incident on the grid. This feature offers distinguishing detected signal as high or low as seen in **Figure 8**. Hence, a binary word can be “watermarked” using an appropriate combination of vertical (M_V) and horizontal (M_H) grids.

Suppose a set of eight ($0.75 \text{ cm} \times 0.75 \text{ cm}$) vertical and horizontal grids are accommodated in the card as an array depicting an eight-bit binary word. This is quite feasible with conductive ink-jet printed material and

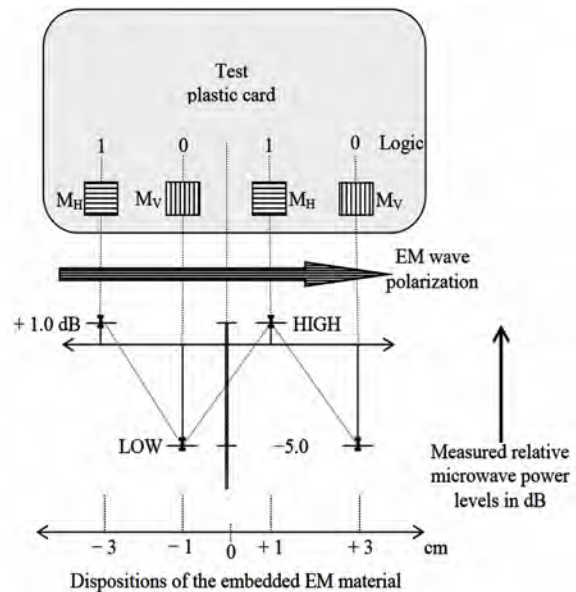


Figure 8. Measured microwave power levels (relative to a blank card) as the test card is swiped across the horizontally polarized EM excitation zone. (M_H : Horizontally structured high- μ grid; and M_V : Vertically structured high- μ grid)

Table 1. Relative transmitted microwave power (in dB) across the test plastic card *versus* dimension (area in cm²) of a single frame of embedded high- μ material. (The exciting EM wave (at 10 GHz) is horizontally polarized.)

Dimension (in cm ²) of the frame	Embedded single frame: Material and type		
	High- μ plain sheet	High- μ grid with vertical stack of strips	High- μ grid with hori- zontal stack of strips
0.0	0.0	0.0	0.0
0.25	-4.0	-3.5	-2.5
1.00	-10.0	-9.0	-4.5
4.00	-16.5	-15.5	-7.5

Table 2. Relative transmitted microwave power (in dB) across the test plastic card *versus* dimension (area in cm²) of a single frame of embedded copper. (The exciting EM wave (at 10 GHz) is horizontally polarized.)

Dimension (in cm ²) of the frame	Embedded single frame: Material and type		
	Copper plain sheet	Copper grid with vertical stack of strips	Copper grid with hori- zontal stack of strips
0.00	0.0	0.0	0.0
0.25	-2.3	-1.5	-0.5
1.00	-5.5	-4.5	-2.5
4.00	-8.0	-6.5	-3.5

Table 3. Relative transmitted microwave power (in dB) across the test plastic card *versus* dimension (area in cm²) of a single frame of embedded aluminum. (The exciting EM wave (at 10 GHz) is horizontally polarized.)

Dimension (in cm ²) of the frame	Embedded single frame: Material and type		
	Aluminum plain sheet	Aluminum grid with vertical stack of strips	Aluminum grid with horizontal stack of strips
0.00	0.0	0.0	0.0
0.25	-2.5	-1.5	-0.5
1.00	-7.5	-5.5	-3.5
4.00	-9.0	-7.5	-4.5

processing. This would allow a set of $2^8 = 256$ combinations of binary signatures. If narrower strips in the grid-frame are used, the word size can further be increased; however, it requires narrow field of excitation/reading warranting a careful design of microwave transceive antennas. (In the presence study, however, a simple slot in the H-plane is used and, therefore, only a resolution of four distinguishable grids is realized).

The overall observation of the results obtained supports the proof-of-the-concept and indicates the feasibil-

ity to enhance the security feature of plastic cards with the proposed "watermarking" strategy. With this additional/overlay layer of security in the cards, the buried "watermarking" remains invisible towards fraud and duplication. Together with the state-of-the-art security technology that prevails on a plastic card (such as holography, etching, microtext, photographic perforation, UV ink, ghost images, and digital watermarking, etc.), the proposed method can be regarded as a novel addition.

This EM-material based watermarking technique offers ample scope for further studies. The following can be listed thereof:

- As indicated earlier, the binary formatting of watermarking using a passive set of grids can be conveniently fabricated using conductive ink-jet printing within the plastic card. Unlike traditional etching or photolithographic designs, printed traces and lines of about 25 m can be realized as indicated in [2]. The conductivity of ink-jet varies from 0.4 to 2.5×10^7 S/m realized with silver nano-particles. This conductivity will offer required attenuation profile needed when used as the card embedment

- With the existing art of printed-antenna technology, the excitation and receiving (sensing) antennas can also be tailored to match the transceive aspects of the microwave across the test-card.

- In using low-power microwave standard ISM 2450 MHz [3] frequency source/detection methods can be adopted. Compatible RF transceivers available as surface-mounted modules for ISM 2450 MHz applications can be adopted for the present work. Such modules are also optionally available with integrated antenna. They are designed for control and industrial automation purposes. ADC capabilities are also built in.

- The superimposed microwave illumination will not interfere with 125 kHz HF illumination used in certain card-reading systems. Further, the proposed design can be introduced as a part of card-swiping unit without cross-interfering with magnetic stripe and/or chip-card processing electronics.

- Though binary formatting of watermarking indicated here uses a passive set of metallic grids, it may be possible to make such grids semi-active with a set of vertical and horizontal IC diodes, (which can be biased via metal contacts at the rim of the card during the swiping mode from a DC source made available in the card swiping unit). These biased diodes can emulate programmable grid structures as discussed by Neelakanta *et al.* in [8]. That is, depending upon the ON-OFF states of the diodes, the binary format can be dynamically changed. This provides additional security to the card, inasmuch as the binary ID format can be preprogrammed and changed dynamically. Such diode-based system can also be a part of any chip-embedded plastic cards.

- This is a noninvasive strategy and almost non-line-of-sight method.
- Larger the size of the sheets used, more will be the output signal, that is, more sensitivity.
- It is a "passive" method in the sense that it uses simple EM materials.
- The design optimization is aimed at maximizing the signal output and improving the sensitivity of the system. The following considerations are implied:
 - Location of transmitter and receiver modules with respect to the card slot: With the availability of surface-mounted devices, this consideration can be comfortably engineered in a compact and acceptable form.
 - Transmitter/oscillator power: The oscillator can be set in sleeping mode (with the power switched off) and can be made active only when the card is *in situ* for swiping.
 - The size of the grid-frames used vitally decides the sensitivity of the system and has to be optimized.

In summary, the proposed EM-material based invisible watermarking is a viable method and offers a prospective scope for a new security technology option for plastic card industry. As indicated, it provides two distinct aspects of security in plastic cards embedded with EM-material based watermarking: 1) The system first identifies/detects the presence of the embedded material. Any forged card with the absence of such buried material will be rejected; and, 2) with the vertical/horizontal grid structures, inclusion of encoding/decoding of a binary word is also feasible. Further, a crisscross formatted array of the test EM materials can be suitably tailored for binary encoding/decoding with dual/circularly polarized excitations. More studies in this direction are open questions and are in progress. 3) To the best of the authors' knowledge no similar idea and/or implementation of the concept indicated in this work has been deliberated in open literature. 4) The security features in plastic cards that currently exist do not *per se* are based on concealed EM material-specific binary signature described in the present work. The "watermarking" of the type indicated here is not visibly present and if tampered with, will not authenticate when the card is swept in the microwave set up improvised. As such it offers additional security to the

card more than the available (security) features on the card. 5) Improvising this new feature is not expensive and may not add appreciable cost to the existing plastic cards. 6) It is therefore aptly suited for commercial exploitation since there is no parallel competitive system available. 7) The system described here is largely a proof-of-concept design. More rigorous theoretical study can be directed towards design optimization especially in devising more number of vertical and horizontal EM stripes so as to obtain larger size of binary word towards authentication and for covering more number of cards.

REFERENCES

- [1] P. S. Neelakanta, "Handbook of electromagnetic materials – Monolithic and composite versions and their applications," FL: CRC Press, Boca Raton, 1995.
- [2] R. Rida, L. Yang, R. Vyas, and M. M. Tentzeris, "Conductive inkjet-printed antennas on flexible low-cost paper-based substrates for RFID and WSN applications," *IEEE Antennas and Propagation Magazine*, Vol. 51, No. 3, pp. 13–23, 2009.
- [3] ISO Standard 18000–Part 4: Air interface communications at 2.45 GHz.
- [4] F. Ros, J. Borla, F. Leclerc, R. Harba, and N. Launay, "An industrial watermarking process for plastic card supports," *Proceedings of IEEE International Conference on Industrial Technology (ICIT'06)*, Mumbai, pp. 2809–2814, 15–17 December 2006.
- [5] S. Ramo, J. R. Whinnery, and T. V. Duzer, "Fields and waves communication electronics," Wiley Eastern Private Limited, New Delhi, 1995.
- [6] A. F. Harvey, "Microwave engineering," Academic Press, London, pp. 601–605, 1963.
- [7] H. Jasik, "Antenna engineering handbook," McGraw-Hill Book Corporation, New York, Chapter 32, pp. 35–40. 1961.
- [8] P. S. Neelakanta, A. K. Stampalia, and D. DeGroff, "An actively-controlled microwave reflecting surface with binary pattern modulation," *Microwave Journal*, Vol. 46, No. 12, pp. 22–36, 2003.

The Additional Criterion for the Determination of the Time of Minimum of a Solar Cycle

Habibullo I. Abdussamatov

Pulkovo Observatory, St. Petersburg, Russia.
Email: abduss@gao.spb.ru

Received September 22nd, 2009; revised October 18th, 2009; accepted October 23rd, 2009.

ABSTRACT

The sunspot number is becoming an increasingly insufficiently reliable parameter for the determination of the time of minimum of a solar cycle during the prolonged and deep minimum of the 23rd solar cycle. Moreover, the sunspot number does not quantitatively reflect physical processes and is a practically conventional qualitative “noisy” parameter. Introduction of an additional criterion for the determination of the time of minimum of a solar cycle is becoming particularly topical due to the upcoming common descent of the level of the 2-secular cycle, when the amplitude of sunspot activity variation will sequentially decrease during several subsequent cycles (after the 23rd cycle). We propose the adoption of the smoothed minimal level of the total solar irradiance (TSI) as an additional physically justified criterion for the determination of the time of minimum of a solar cycle during the minimum of sunspot activity. The minimal level of the monthly average values of the TSI smoothed for 13 months when the last two of its values exceed the preceding value at the point of minimum will additionally indicate the time of minimum of a cycle. The additional criterion has been successfully used for the determination of the time of minima of the preceding 21st and 22nd cycles.

Keywords: Sun, Solar Cycle, Solar Cycle Minimum, TSI, Sunspot Activity

1. Introduction

The elapsing 23rd solar cycle is unique by its duration. It has become the longest (longer than 12.5 years) cycle among all reliably established and studied 11-year solar cycles for more than 150 years of their reliable observations (starting from the 10th cycle). The maximal duration of this cycle additionally confirms the approach of the active descent phase of the 2-secular solar cycle because the duration of an 11-year cycle in whole depends on the phase of a 2-secular solar cycle. Durations of 11-year cycles sequentially increase from the phase of growth to the phases of maximum and descent of a 2-secular cycle [2]. The determination of the exact time of minimum of the ongoing cycle and, consequently, of the beginning of the new 24th solar cycle is becoming more and more topical problem nowadays. The traditional method for the determination of the time of minimum of an 11-year cycle is mostly based on the computation of the sunspot number. Here, the main criterion for the determination of the time of minimum of an 11-year cycle is the minimum of monthly average values of the sunspot number smoothed for 13 months (other criteria are used as well). However the sunspot number does not quantitatively reflect physical aspects of the processes of cyclic variations on the Sun

and is practically a conventional qualitative “noisy” parameter. Additionally, during the prolonged and deep minimum of the ongoing 23rd cycle the appearance of sunspots has become a rare event. Due to very low fluctuations of the sunspot number it is becoming an increasingly unreliable quantitative physical parameter for the determination of the time of minimum of the solar cycle (**Figure 1**). This fact indicates the importance of the search for and introduction of an additional criterion for the determination of the time of minimum of a cycle. The additional criterion should be based on the accurate quantitative measurement of a global parameter of the Sun.

2. The Additional Criterion

Introduction of the additional criterion for the determination of the time of minimum of a solar cycle has become particularly topical due to the upcoming overall descent of the level of the 2-secular cycle, when the amplitude of the sunspot activity variation will sequentially decrease during several subsequent 11-year cycles [1,3,4,6]. Determination of the times of minima of the subsequent cycles (after the 23rd cycle) by the means of traditional method will be less accurate because of a more substantial decrease of the sunspot number and because of its near-zero

fluctuation for a long time during the periods of minima of the sunspot activity of these cycles. The uncertainty of determination of the time of minimum of the above cycles can last longer after the minimum takes place. It is known that being the consequences of the same processes occurring deeply inside the Sun, 11-year and 2-secular cyclic variations of the sunspot activity and total solar irradiance (TSI) are synchronized and cross-correlated both in phase and amplitude [1,3]. 11-year cyclic variations of the TSI

take place with respect to its 2-secular variation component (dashed line, revealed by us) (**Figure 2**). By the course of gradient variation of the 2-secular component of the TSI during the minima of three successive cycles one can determine the further course of both TSI and sunspot activity for not only the approaching cycle but also for several subsequent cycles (with somewhat less accuracy) [3].

We propose the use of a high-precision global physical parameter – the minimal level of smoothed TSI variation

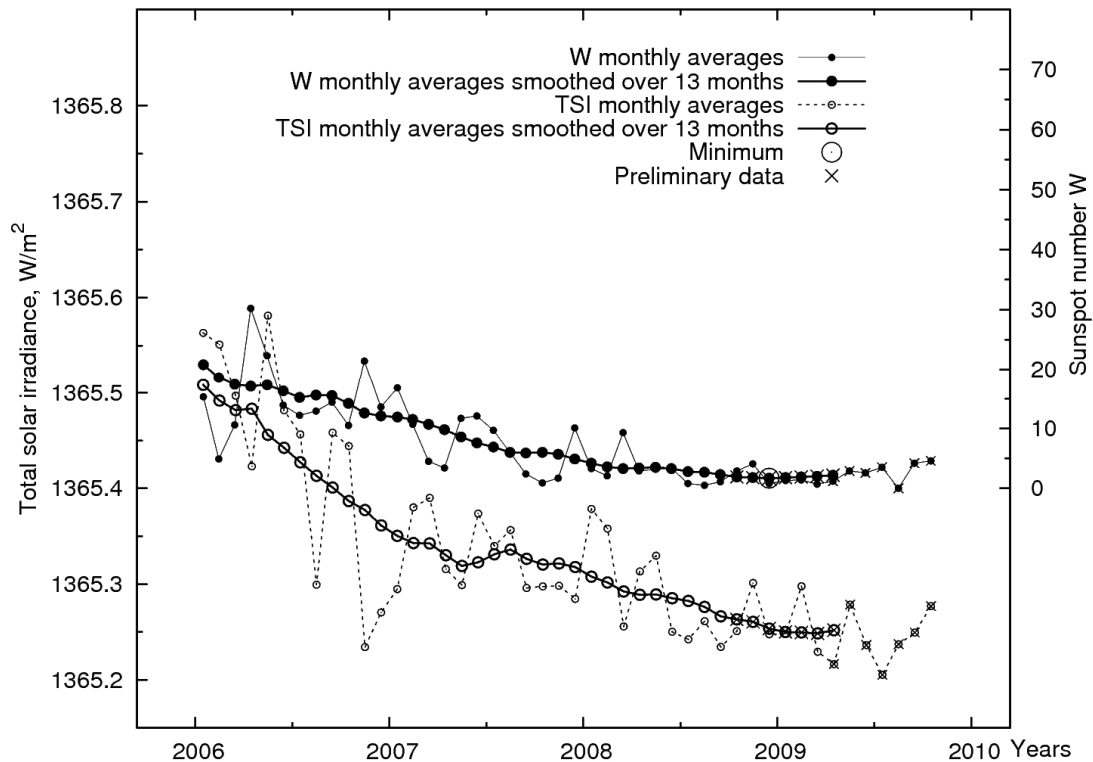


Figure 1. Variations of the monthly average values of the TSI (Fröhlich, 2009) and sunspot number (SIDC, 2009) and their values smoothed over 13 months during the period of minimum of the 23rd cycle in 2006-2009

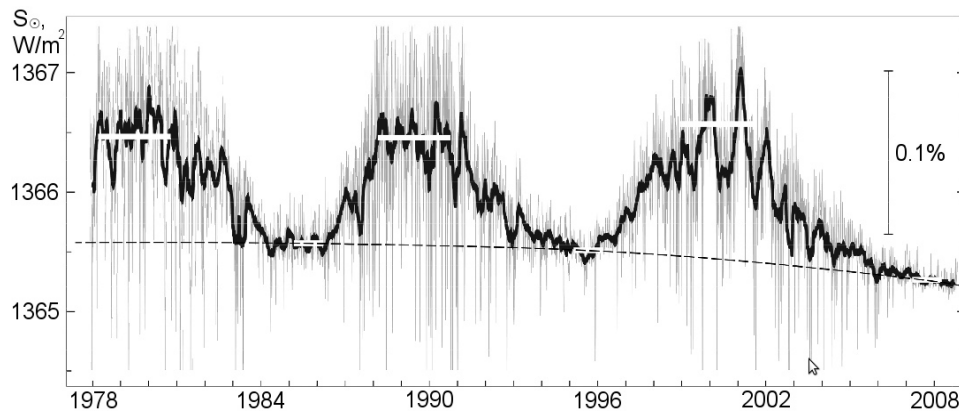


Figure 2. Variations of the TSI over the period from November 16, 1978 to October 24, 2009 (bold line) (Fröhlich, 2009) and of its 2-secular component (dashed line), revealed by us

measured more reliably during the period of minimum of sunspot activity – as an additional criterion for the determination of the time of minimum of a solar cycle. The measured values of the TSI are virtually free of distortions due to the minimal number of sunspots and faculae fields crossing the disc of the Sun during this period. The minimal level of the monthly average values of the TSI smoothed for 13 months when the last two of its values exceed the preceding value at the point of minimum indicates the time of minimum of a cycle. This method involving 13 months smoothing allows one to virtually get rid of the influence of random monthly fluctuations of the TSI which take place due to the transits of small sunspots and small faculae fields across the disc of the Sun during the period of minimum of the cycle.

The given method allows one to determine the time of minimum of a solar cycle with assured reliability. The gradual adoption of 11-month and later 9-month smoothing instead of 13-month will be possible when the direct measurements of the TSI become more reliable and accurate. The proposed additional method for the determination of the time of minimum of a cycle on the basis of the smoothed minimal level of the TSI will provide the possibility of a reliable determination of the dates of these events particularly for the future 11-year cycles which will take place during the phase of descent and minimum of the 2-secular cycle. Here, the smoothed

minimal level of the TSI entirely and quantitatively reflects physical aspects of the global cyclic variations of activity of the Sun and is not a practically conventional and more “noisy” qualitative parameter unlike the sunspot numbers.

In order to test the reliability and viability of the proposed method on the basis of the additional criterion we have used it for the determination of the dates of minima of the preceding 21st and 22nd cycles on the basis of the smoothed TSI values and compared them to the dates of these minima determined earlier on the basis of sunspot numbers. For comparison we have plotted the corresponding courses of variations of the monthly average values of the TSI [5], of the sunspot number [7] and of their smoothed values over 13 months during the periods of minima of sunspot activity within the 21st and 22nd cycles (**Figures 3 and 4**). It has been confirmed that according to the smoothed sunspot number the minimum of the 21st cycle had taken place in September 1986 and the minimum of the 22nd cycle in May 1996. According to the additional criterion based on the smoothed TSI the minimum of the 21st cycle had unambiguously taken place in October 1986 and the minimum of the 22nd cycle in June 1996 (see **Table 1**). Correlation coefficients between the series of W and TSI smoothed for 13 months near the minima of the 21st, 22nd and 23rd cycles are equal to 0.95, 0.97 and 0.97 respectively.

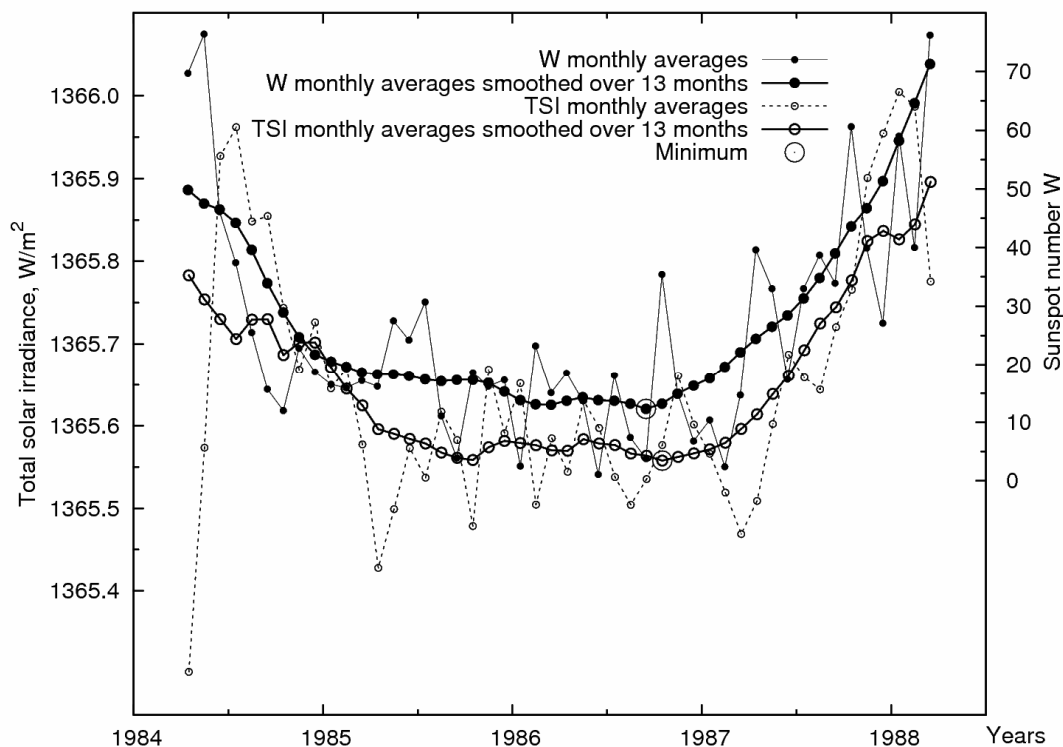


Figure 3. The same as on the Figure 1 for the period of minimum of the 21st cycle in 1984-1989

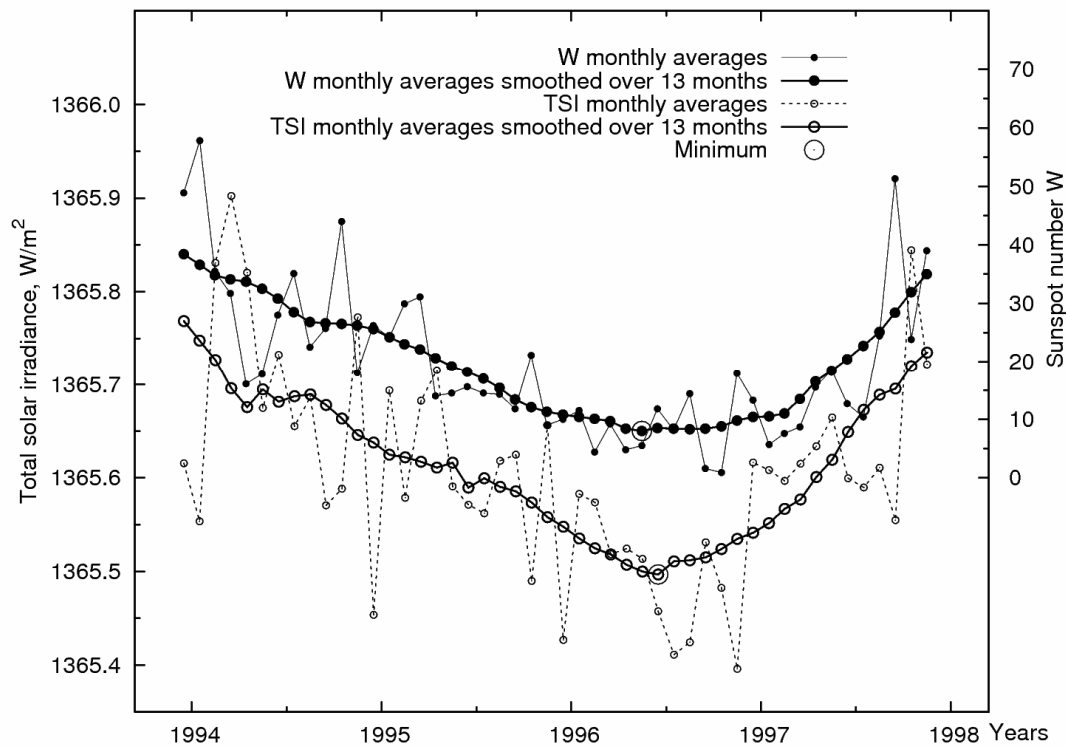


Figure 4. The same as on the Figure 1 for the period of minimum of the 22nd cycle in 1993-1998

Table 1. Values of the TSI and sunspot numbers smoothed over 13 months during the minima of the cycles 21-23 and the dates of minima of these cycles determined on the bases of the TSI and sunspot number

Solar cycle	Minimum of a cycle				
	Date on the basis of sunspot number	Date on the basis of TSI	Smoothed value of sunspot number	Smoothed value of TSI (W/m^2)	Difference in TSI with respect to the minimum of 1986 (W/m^2)
21	September 1986	October 1986	12.3	1365.57	0
22	May 1996	June 1996	8.0	1365.50	0.07
23	December 2008*	—	1.7* in December 2008	1365.25* in January 2009	0.32 in January 2009

The dates of minima determined by the means of the traditional method both in 21st and 22nd cycles lag one month behind the dates determined on the basis of the additional criterion. What is the reason of the mentioned time lag? The lag is observed doubtlessly due to the direct influence of the observed common descent of the TSI. This influence compensates the new 11-year cyclic rise of the TSI within a common (overall) course of observed TSI variation during a certain period of time (the period depends on the gradients of two-secular descent and 11-year rise). This leads to a certain offset (time lag) of the beginning of the new cycle. Anyway, this question deserves further dedicated research partly in order to determine more precisely the duration of the time lag in the descent phase of the two-secular cycle. We suggest that the time of minimum of a cycle determined by the

new additional criterion is closer to the truth especially in the period of a deep minimum because it is based on the smoothed quantitative global physical parameter. In the deep minimum of the 23rd cycle in January 2009 the value of TSI smoothed over 13 months reached the record low level of 1365.25 W/m^2 which is 0.32 W/m^2 and 0.25 W/m^2 less, than in the minima of the 21st (October 1986) and 22nd (June 1996) cycles respectively. The smoothed value of the sunspot number in December 2009 also reached the record low level and was equal to 1.7 (see Table 1).

REFERENCES

- [1] H. I. Abdussamatov, "Long-term variations of the integral radiation flux and possible temperature changes in the

- solar core,” *Kinematics and Physics of Celestial Bodies*, Vol. 21, No. 6, pp. 328–332, 2005.
- [2] H. I. Abdussamatov, “The time of the end of the current solar cycle and the relationship between duration of 11-year cycles and secular cycle phase,” *Kinematics and Physics of Celestial Bodies*, Vol. 22, pp. 141–143, 2006.
- [3] H. I. Abdussamatov, “Optimal prediction of the peak of the next 11-year activity cycle and of the peaks of several succeeding cycles on the basis of long-term variations in the solar radius or solar constant,” *Kinematics and Physics of Celestial Bodies*, Vol. 23, pp. 97–100, 2007.
- [4] S. Duhau, “An early prediction of maximum sunspot number in solar cycle 24,” *Solar Physics*, Vol. 213, pp. 203–212, 2003.
- [5] C. Fröhlich, “Solar constant,” 2009. <http://www.pmodwrc.ch/pmod.php?topic=tsi/composite/SolarConstant>
- [6] S. Sello, “Solar cycle activity: A preliminary prediction for cycle 24,” *Astronomy and Astrophysics*, Vol. 401, pp. 691–693, 2003.
- [7] SIDC (Solar Influences Data Analysis Center), 2009. <http://sidc.oma.be/sunspot-data/>

Modeling of the Earth's Planetary Heat Balance with Electrical Circuit Analogy

Habibullo I. Abdussamatov, Alexander I. Bogoyavlenskii, Sergey I. Khankov, Yevgeniy V. Lapovok

Pulkovo Observatory, St. Petersburg, Russia.
Email: abduss@gao.spb.ru

Received December 4th, 2009; revised January 12th, 2010; accepted January 17th, 2010.

ABSTRACT

The integral heat model for the system of the Earth's surface—the atmosphere—the open space based on the electrical circuit analogy is presented. Mathematical models of the heat balance for this system are proposed. Heat circuit which is analog of the electrical circuit for investigating the temperature dependencies on the key parameters in the clear form is presented.

Keywords: *Electrical Circuit Analogy, Planetary Heat Balance, Climate Trends*

1. Introduction

Electrical circuit analogy can be effectively used in thermophysical applications [1]. Ohm's and Kirchhoff's laws are work in equivalent schemes with lumped parameters; heat fluxes are analogues of currents, heat conductivity (or heat resistance) is analog of the electrical resistance, and temperatures are analogues of the electrical potential. The purpose of this work is to use this method for development of the integral analytical model of the heat balance based on the equivalence scheme for the system the surface—the atmosphere—the open space describing heat processes clearly.

Variations of surface and atmospheric radiative parameters and atmospheric transparency for the surface radiation have important influence on the Earth's climate. The simplest and convincing explanation of calculated dependencies is obtained with conversion from radiative characteristics to specific heat conductivities.

In this work we have restricted with analysis of how atmospheric transparency for the heat IR radiation from the surface influences on the climate. It is a topical problem, because nowadays this transparency is regarded as one of the cardinal factors making the climate. To reach the general result, we are investigated all range of the possible transparency changed from 0 to 1.

2. Physical Model

Method of the electrical circuit analogy can be used for a system of isothermal bodies having small heterogeneities, its make it possible to establish connection among sche-

matic nodes with heat conductivities, and nodes define temperatures. In other words, the electrical circuit analogy can be used for the heat exchange problem and can't be used for the heat conduction problem. So we regard the atmosphere as the homogeneous cover for the surface. The assumption is adopted that all atmospheric heterogeneities on the vertical dimension (pressure, density, temperature profiles) don't influence on heat conditions of the underlying surface. We operate the surface temperature averaged on the whole surface (including the land and the ocean) and the atmospheric temperature averaged on the atmospheric volume.

These simplifications are brought to the idealized model of the system which contains the isothermal spherical core inside the isothermal spherical cover. The heat sources caused by the incoming solar radiation acts on the cover surface and in the cover (in W/m^2). These heat sources are uniformly distributed.

In generally accepted practice the absorbed heat fluxes averaged and uniformly distributed on all the spherical surface are used [2]. It is reasonable by the Earth's rotation around terrestrial axis, and assumption is adopted that speed of this rotation is greater than warming or cooling rate (in days^{-1}). In other words, the Earth's orbital period is considerably smaller than the value of the thermal inertia. This fact justifies using of averaged atmospheric and surface temperatures as criteria of the climate state. The core and the cover are in the convective and radiative heat exchange with each other. The cover is partially transparent for the core heat radiation and also gives the heat energy with the radiation to the open space itself.

The developed equivalent scheme is shown in **Figure 1**. Three levels are notable: the first level corresponds to the surface with the highest temperature T_s , the second level corresponds to the atmospheric averaged on volume temperature T_a , and the third one corresponds to the open space temperature T_e assumed equals to zero, $T_e = 0\text{K}$. The biggest part of the surface is the ocean, so we use the heat capacity of the ocean describing transient behavior.

Heat sources Q_s and Q_a are analogues of current sources: Q_s —specific power of the heat emission on the surfaces of the land and the ocean; Q_a —specific power of the heat emission in the atmosphere. Sources of the temperature force, which are analogues of voltage, are omitted on the scheme as temperatures T_s and T_a are potentials depending on scheme parameters. Surface capacities of the ocean and the atmosphere C_s and C_a in $\text{J/m}^2\text{K}$ are analogues of the electrical capacity. Nodes are connected with conductivities, through its specific heat fluxes q_i are flowing. Radiative conductivities α_s , α_a , α_r presents as electrical resistance usually presents. The black frame denotes the specific heat conductivity α , which is resultant total convective and evaporating-condensation coefficient of the heat transfer from the ocean surface to the atmosphere in $\text{W/m}^2\text{K}$.

Flux q_s is a radiative flux transferred from the ocean surface to the open space directly through atmospheric window. Specific flux q_a is defining power of the heat radiation from the atmosphere to the open space, and q_r is the resultant radiative flux between the ocean and the atmosphere and it describes difference between fluxes transferred with the radiation from the ocean surface to the atmosphere and from the atmosphere to the ocean. Specific heat flux q is a resultant flux transferred by the convection and evaporating-condensation mechanism from the ocean to the atmosphere.

In the transient heat state the change of the heat con-

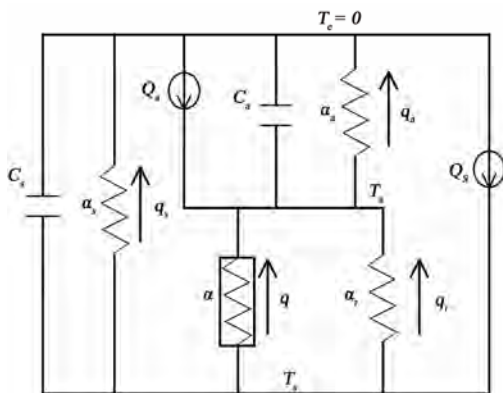


Figure 1. The equivalent thermal scheme based on the electrical circuit analogy corresponds to the model of planetary heat balance. Arrows shows the directions of the heat fluxes q . Q are sources of heat power. C are capacities. α are conductivities. See in text the detailed description of the scheme elements

tent in the atmosphere and the ocean mixed layer is taking into account with the flux from the capacities C_s and C_a . The isothermal active layer can be allocated for the ocean with the layer thickness l_o , its depth depends on the convective hashing of water in it. For the land it is necessary to take into account unevenness of temperature distribution in the soil thickness, it is attained with using the transient heat equation. On this stage we don't consider this problem, because the electrical circuit analogy can't be used to solve it.

Integral emissivities and basic values of atmospheric transmission in IR range are used to define coefficient of radiative heat transfer and heat fluxes. For specificity it is necessary to introduce some assumptions about its:

- surface emissivity is obtained as averaged on the whole ocean and land, it averaged value is defined from conditions of the heat balance;
- averaged values of atmospheric emissivity with regard to averaged cloudiness is obtained the same in the direction to the space and in the direction to the surface;
- radiative balance is described using net heat flux and transfer factor, last one is deduced through well-known way [1];
- atmospheric transmission for IR spectral range taking into account with it averaged values for atmospheric windows (main atmospheric window is the range $8.13\ \mu\text{m}$) [3].

There are two main reasons to use this model to analysis of the climatic global trends.

First, the ocean is the main part of the surface (more than 75% of it). The ocean has a very big thermal inertia caused by its very big thermal capacity. As it shown below, the constant of thermal inertia is about 8.5 years or more. As result, the surface temperature doesn't change seriously during one day for both lighted and shadowed parts of the surface. That's why the averaged temperature of surface can be used. This fact presents on the scheme with node having temperature T_s .

The values of the atmospheric density and the atmospheric capacity are an additional factor to the first one described above. Both factors make it valid and efficient to investigate the global climatic trends with the model based on the equivalent thermal scheme, which is build with electrical circuit analogy.

3. Mathematical Model

For composing the heat balance of the system of the surface—the atmosphere, the general equation system describing the heat exchange among isothermal bodies is introduced [1]. In the most general case the heat exchange among n bodies is described by the ordinary differential equation system, which contains n equations [1]

$$C_{\Sigma i} \frac{dT_i}{d\tau} + \sum_{j=1}^n P_{ij} + P_{ie} = P_i \quad (1)$$

Initial conditions are usually setting in form

$$T_i(\tau = 0) = T_{i0} \quad (2)$$

In our case it is convenient to use the specific heat fluxes q_{ij} , q_{ie} and Q_i defined by rates $q_{ij} = P_{ij}/S_i$, $q_{ie} = P_{ie}/S_i$, $Q_i = P_i/S_i$; here S_i – surface area of body no. i taking part in heat exchange. As result, the equations from the system (1) are expressed as

$$C_{\Sigma i} \frac{dT_i}{d\tau} + \sum_{j=1}^n q_{ij} + q_{ie} = Q_i \quad (3)$$

Surface densities of total capacities C_i are defined from rates $C_i = C_{\Sigma i}/S_i$.

Specific heat fluxes can be setting in form

$$\begin{aligned} q_{ij} &= \alpha_{ij}(T_i - T_j); \\ q_{ie} &= \alpha_{ie}(T_i - T_e) \end{aligned} \quad (4)$$

Here α_{ij} and α_{ie} —conductivities for heat transfer from body no. i to body no. j and from body no. i to environment, respectively; T_i , T_j and T_e —absolute temperature of bodies i , j and environment.

In the beginning we use the simplified steady-state situation corresponded to the mathematical description (3) of the scheme in **Figure 1**.

$$\begin{aligned} -q_r - q + q_a &= Q_a \\ q_r + q + q_s &= Q_s \end{aligned} \quad (5)$$

Fluxes in the system (5) are defined from rates

$$\begin{aligned} q_r &= \alpha_r(T_s - T_a); \\ q &= \alpha(T_s - T_a); \\ q_a &= \alpha_a(T_a - T_e) = \alpha_a T_a; \\ q_s &= \alpha_s(T_s - T_e) = \alpha_s T_s; \end{aligned} \quad (6)$$

This system (5) contains the four unknowns (q_r , q , q_a , q_s) and two equations, so it can't be solved unequivocally. However, for the heat circuit the problem is simplified as parameters of this circuit (α_r , α_a , α_s) are estimated definitely throw the potentials—temperatures T_s and T_a .

In rates (6) the conductivities (except α) are estimated with formulas

$$\begin{aligned} \alpha_r &= F\sigma(T_s^4 - T_a^4)/(T_s - T_a); \\ \alpha_a &= (1 - \gamma\delta_a)\varepsilon_a\sigma T_a^3; \\ \alpha_s &= \gamma\delta_s\varepsilon_s\sigma T_s^3 \end{aligned} \quad (7)$$

Here ε_a , ε_s —emissivities of the atmosphere and the ocean; F —transfer factor for the system of the ocean—the atmosphere; δ_s —the fraction of the ocean emissive power contained in atmospheric windows; δ_a —the fraction of the atmospheric emissive power contained in atmospheric windows; $\sigma = 5.67 \cdot 10^{-8} \text{ W/m}^2\text{K}^4$ —the Stefan-Boltzmann constant; γ —atmospheric transmission for the heat radiation in atmospheric windows.

As it follows from (7), scheme in **Figure 1** is considerably nonlinear because the scheme parameters α_i depends sharply on the temperatures.

With regard to (6) and (7), system (3) can be expressed as

$$\begin{aligned} C_a \frac{dT_a}{d\tau} + F\sigma(T_a^4 - T_s^4) + \alpha(T_a - T_s) \\ + (1 - \gamma\delta_a)\varepsilon_a\sigma T_a^4 &= Q_a; \\ C_s \frac{dT_s}{d\tau} + F\sigma(T_s^4 - T_a^4) + \alpha(T_s - T_a) \\ + \gamma\delta_s\varepsilon_s\sigma T_s^4 &= Q_s; \\ F &= \{1/[(1 - \gamma\delta_s)\varepsilon_s] + [(1 - \gamma\delta_s)\varepsilon_s] - 1\}^{-1} \end{aligned} \quad (8)$$

To solve the system (8), initial conditions must be adopted, and the set of parameters satisfied to known components of the heat balance Q_a , Q_s , q_s , and T_s must be defined.

It is important to establish the conductivities α correctly. It depends on small variations of T_s and T_a weakly. Arrhenius [4] examined the surface only without analysis of atmospheric temperature situation. He assumed the convective—mass-transfer flux q to be constant. However, as it shows below, condition $\alpha = \text{const}$ is more correct. Initial value of α defined from heat transfer equations depends on key parameters included in systems (8) and (5), but it is assumed that α is constant in following calculations of the dependence of T_s and T_a on variations of any parameter.

4. Parameters of Heat Balance for Transient and Steady-State Conditions

Following values were chosen as initial defining components of the heat balance [2] $Q_s = 168 \text{ W/m}^2$; $Q_a = 67 \text{ W/m}^2$; $q_s = 40 \text{ W/m}^2$; $q_a = 195 \text{ W/m}^2$ and $T_s = 287 \text{ K}$ [5]. Surface heat capacity of the atmosphere is obtained from known mass and specific heat capacity of air [3] $C_a = 10^7 \text{ J/m}^2\text{K}$. For the ocean the heat capacity is obtained throw the specific heat capacity and the density, so $C_s = 4.2 \cdot 10^6 l_o$, l_o is the depth of the ocean mixed layer specified in meters.

Values introduced above are enough to estimate thermal inertia characteristics of the Earth investigated as the whole planet. Impact of parameters variations should be calculated numerically in the non-linear statement of the problem to avoid errors.

We begin with analysis of termoinertia characteristics of the system of the surface—the atmosphere.

Adding up left and right parts of first and second equations from the system (8), we obtain

$$\begin{aligned} C_a \frac{dT_a}{d\tau} + C_s \frac{dT_s}{d\tau} + \alpha_a T_a + \alpha_s T_s &= Q_{\Sigma} \\ Q_{\Sigma} &= Q_a + Q_s = 235 \text{ W/m}^2 \end{aligned} \quad (9)$$

For the simplest estimations we assume that the difference between temperatures T_s and T_a is small:

$$T_a \approx T_s = T \quad (10)$$

In this case (9) can be introduced in form:

$$t \frac{dT}{d\tau} + T = \Theta; \quad (11)$$

$$t = \frac{C_a + C_s}{\alpha_p}; \quad \Theta = \frac{Q_\Sigma}{\alpha_p}; \quad \alpha_p = \alpha_s + \alpha_a$$

here t —thermal inertia constant for the system of the ocean—the atmosphere; θ —steady-state planetary temperature of the Earth; Q_Σ —total power of heat sources in the system of the ocean—the atmosphere; α_p —planetary conductivity for heat radiation from the Earth to the space.

Equation (11) makes it possible to get the very simple but reliable estimations. It is confirmed by results of our additional non-linear calculations, which makes it seen that the temperature change in time is not strictly exponential, but the duration of the transition condition is estimated exactly with the linear problem definition.

To get estimations, we assume $\theta \approx 287\text{K}$ and $Q_\Sigma = 235 \text{ Wm}^2$, and we obtain $\alpha_p \approx 0.82 \text{ W/m}^2\text{K}$. Substituting this value and values of C_a and C_s to formula for the thermal inertia, we find

$$t = \frac{1 + 0.42l_o}{0.82} \cdot 10^7 \text{ s} = 0.386(1 + 0.42l_o) \text{ year} \quad (12)$$

Assuming the depth of the ocean mixed layer $l_o = 50 \text{ m}$ (accuracy of this value is not so important for demonstrative estimate), the Earth's thermal inertia constant is obtained to be $t = 8.5$ years. If any key parameter (atmospheric transmission, solar constant etc.) changes in the spurts manner, the new steady-state condition would form over the time, which approximately equals to three thermal inertia values, in our case $\tau = 3t = 25.5$ years. If key parameters changes slowly then transient process will be much longer.

Next step is to find values of parameters in case of steady-state conditions—when $dT_i/d\tau = 0$. We begin with analysis of the connection among transmission γ and emissivities ε_s and ε_a .

It is known [3] that main atmospheric window corresponds to the spectral range $8..13 \mu\text{m}$. In range $13..17.5 \mu\text{m}$ the radiation is close to be totally absorbed by CO_2 molecules and water vapor (overlap of absorption band-width). In range $> 17.5 \mu\text{m}$ total contribution of transparency lines on order of magnitude in compare with $8..13 \mu\text{m}$. We have obtained the energy fraction $\delta \approx 0.31$ with $T_s = 287\text{K}$. Our calculations have shown that accounting of all atmospheric windows doesn't change the final result of calculations. From (6) and (7) it is possible to obtain following rate:

$$\gamma_{init} \varepsilon_s = q_s / q^*; \quad q^* = \delta_s \sigma T_s^4 \quad (13)$$

here γ_{init} —assumed initial value of transmission, γ is vary relative to it; q^* —specific heat flux from the surface with $\varepsilon_s = 1$ to the space throw atmospheric window with absolute transmission $\gamma = 1$.

Assuming $T_s = 287\text{K}$ and $\delta_s = 0.31$, we find $q^* = 120 \text{ W/m}^2$. When $q_s = 40 \text{ W/m}^2$ [2] it is following from (13):

$$\gamma_{init} \varepsilon_s = 1/3 \approx 0.333 \quad (14)$$

From (14) the limitation follows: minimum values γ_{init} and ε_s equal to 0.333, as $\gamma_{init} \leq 1$ and $\varepsilon_s \leq 1$. From (6) and (7) it can be obtained

$$\varepsilon_a = q_a \left[(1 - \gamma_{init} \delta_a) \sigma T_a^4 \right]^{-1} \quad (15)$$

There is a problem on this stage. To study the parameters variations impact on the temperatures from the system (8) when $dT_i/d\tau = 0$, it is necessary to define initial values of T_a and α which are desired quantity. And we should set initial values of γ_{init} , ε_s and ε_a . However, there is indeterminacy as accurate values of these parameters are not known.

To overcome the indeterminacy, we set initial value $\gamma = 0.8$ for preliminary calculations. This value looks reliably for the standard atmosphere. Substituting the initial parameter values in the heat balance equations, following values are obtained: $T_a = 284.25\text{K}$; $\varepsilon_a = 0.7$; $\alpha = 45.56 \text{ W/m}^2\text{K}$. Value ε_s has been defined from (14) directly. Substituting $\gamma_{init} = 0.8$ in (14), we obtain the required value $\varepsilon_s = 0.417$. This value satisfies the assumed heat flux throw transparency window. Assumed value of ε_a is arbitrary to a certain extent, but it corresponds to conceptions of planetary heat balance and planetary temperature.

5. Calculations Results

Assuming parameters values, numerical calculations has been performed how the temperatures, the heat fluxes and the heat conductivities depend on atmospheric transmission γ at steady-state conditions.

Plots in **Figures 2–4** present these dependencies in all range of transmission change $0 \leq \gamma \leq 1$ when conductivity between the ocean and the atmosphere α is constant. Calculations show that in case of constant heat flux q it is the intersection between temperature dependencies. This intersection doesn't correspond to the assumption $q = \text{const}$. So, we use the assumption $\alpha = \text{const}$ in following calculations.

Dependencies of derivatives $N_s = dT_s/d\gamma$ and $N_a = dT_a/d\gamma$ on the radiative heat flux from the surface to the space throw atmospheric window were investigated. We found that the decreasing of atmospheric transparency cause the decreasing of T_i when $q_s < 50 \text{ Wm}^2$, because in the range of value $0 < q_s < 50 \text{ Wm}^2$ the derivatives are positive. For such conditions it is found that decrease of atmospheric transparency (for example, as result of the growing of the greenhouse gases concentration) causes to the increasing of the heat power emitted by the atmosphere to the space,

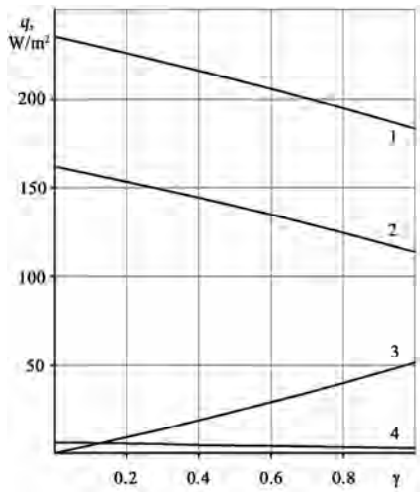


Figure 2. Dependencies of the heat fluxes on atmospheric transmission: 1 – q_a ; 2 – q_r ; 3 – q_s ; 4 – q_r

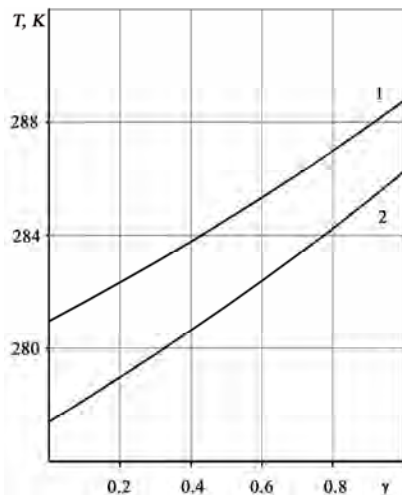


Figure 3. Dependencies of the temperatures on atmospheric transmission: 1 – T_s ; 2 – T_a

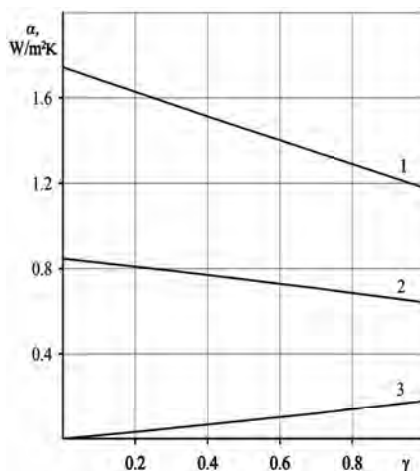


Figure 4. Dependencies of the conductivities on atmospheric transmission: 1 – α_r ; 2 – α_a ; 3 – α_s

and this heat power increases faster than the heat power absorbed by the atmosphere from the surface radiation. Note, that this result corresponds to conclusion from [6] obtained using the other approach.

Greenhouse effect and global warming in the traditional interpretation take place in the case of the unusually heat fluxes from the surface to the space—when $q_s > 50 \text{ W/m}^2$, and also in case of small initial values of γ . If the inequality $\varepsilon_s > \varepsilon_a$ is satisfied, then decreasing of γ would cause warming.

6. Analysis

Dependencies shown in **Figures 2–4** are approximated:

For the fluxes:

$$\left. \begin{aligned} q_s &= a_1\gamma + b_1\gamma^2 \\ q_r &= q_{r1}\gamma + a_2\gamma + b_2\gamma^2 \\ q &= q_1\gamma + a_3\gamma + b_3\gamma^2 \\ q_a &= q_{a1}\gamma + a_4\gamma + b_4\gamma^2 \end{aligned} \right\} \quad (16)$$

For the temperatures:

$$\left. \begin{aligned} T_s &= T_{s0} + c_1\gamma + d_1\gamma^2 \\ T_a &= T_{a0} + c_2\gamma + d_2\gamma^2 \end{aligned} \right\} \quad (17)$$

For the conductivities:

$$\left. \begin{aligned} \alpha_s &= k_1\gamma + l_1\gamma^2 \\ \alpha_r &= \alpha_{r1} + k_2\gamma + l_2\gamma^2 \\ \alpha_a &= \alpha_{a1} + k_3\gamma + l_3\gamma^2 \end{aligned} \right\} \quad (18)$$

Conditions caused by (5) and (16)–(18) should fulfill with any value γ

1) $q_a - q_r - q = Q_a = 67 \text{ W/m}^2$, from where $q_{a1} - q_{r1} - q_1 + (a_4 - a_3 - a_2)\gamma + (b_4 - b_3 - b_2)\gamma^2 = 67$.

2) $q_s + q_a = 235 \text{ W/m}^2$ or $q_{a1} + (a_1 + a_4)\gamma + (b_1 + b_4)\gamma^2 = 235$.

3) $q_s + q_r + q = 168 \text{ W/m}^2$ or $q_1 + q_{r1} + (a_1 + a_2 + a_3)\gamma + (b_1 + b_2 + b_3)\gamma^2 = 168$.

4) $\Delta T = (T_r - T_a) = (T_{s0} - T_{a0}) + (c_1 - c_2)\gamma + (d_1 - d_2)\gamma^2$.
From $q = \alpha \Delta T$ it follows $q_1 + a_3\gamma + b_3\gamma^2 = \alpha(T_{s0} - T_{a0}) + \alpha(c_1 - c_2)\gamma + \alpha(d_1 - d_2)\gamma^2$.

$q_1 = \alpha(T_{s0} - T_{a0})$; $a_3 = \alpha(c_1 - c_2)$; $b_3 = \alpha(d_1 - d_2)$.

Approximation coefficients are in good agreements with each other. Being round to second sign after dot for the fluxes and the temperatures and to fourth sign after dot for conductivities, its substitution to (16)–(18) makes it possible to get formulas for qualitative calculations with error less than 0.3% (except q_s and α_s , for its less than 1%) in form

$$\left. \begin{aligned} q_r &= 6.2 - 3.67\gamma + 0.41\gamma^2; \\ q &= 162 - 40.26\gamma - 8\gamma^2; \\ q_a &= 235 - 44\gamma - 7.6\gamma^2; \\ q_s &= 44\gamma + 7.6\gamma^2; \\ T_a &= 277.4 + 7.5\gamma + 1.37\gamma^2; \\ T_s &= 281 + 6.6\gamma + 1.97\gamma^2; \\ \alpha_r &= 1.744 - 0.573\gamma + 7.486 \cdot 10^{-3}\gamma^2; \\ \alpha_a &= 0.847 - 0.182\gamma - 0.0238\gamma^2; \\ \alpha_s &= 0.158\gamma + 0.0206\gamma^2; \end{aligned} \right\}$$

7. Conclusions

Described research has shown that it is convenient to use the electrical circuit analogy for analysis of the integral heat balance in the system of the surface—the atmosphere—the open space. Reducing of this system to the three-level scheme with lumped parameters (α_i) makes the analysis more obvious. This scheme contains some indeterminacy. However, the analytical dependencies connect all coefficients of the radiative heat transfer and specific fluxes with temperatures. So, it is possible to describe the fluxes, temperatures and conductivities as dependencies on any initial parameter. Particularly, its can depend on atmospheric transmission in form (16)–(18).

The parameters γ_{init} and ε_s are connected by the ratio $\gamma_{init}\varepsilon_s = 1/3$, and T_a and ε_a are connected by the more compound dependence on γ_{init} , so the heat balance contains the indeterminacy in specific values of these parameters. With the more reliable values of listed parameters, there are quantitative dependencies (19).

It is found that if $q_s \leq 50 \text{ W/m}^2$ and $\varepsilon_a > \varepsilon_s$ then atmospheric transparency decreases and the averaged temperatures decrease. It can be seen from (19) that if γ decreases then q_s decreases, but the flux q_a from the atmosphere to the open space increases on the same value. Also the atmospheric temperature T_a decreases in spite of increasing of the resultant convective—evaporating flux q . However, $q < q_a$, and the increasing of the flux q can't compensate the increasing of the flux q_a given by the

planet to the space. The decreasing of the cover (atmospheric) temperature causes the decreasing of the core (surface) temperature. Anti-greenhouse effect realizes on this way, and the decreasing of atmospheric transmission causes global cooling. It is found as the additional result that the radiative heat transfer q_r has small influence on the integral heat balance.

Greenhouse effect in its traditional interpretation realizes when one of the following conditions is satisfied: $q_s > 50 \text{ W/m}^2$; $\varepsilon_s > \varepsilon_a$; $\gamma < 0.4$.

It is found that trends of the climate change caused by the increasing of the carbon dioxide emission depends on the whole set of parameters realized actually nowadays. There is the great interest to determine the values of the parameters as reliably and quickly as possible. Small changes of the basic parameter values established after 12 years [7] don't influence on our results.

REFERENCES

- [1] J. H. Lienhard IV and J. H. Lienhard V, "A heat transfer textbook," 3rd Ed., Cambridge, MA, Phlogiston Press, 2008.
- [2] J. T. Keihl and K. E. Trenberth, "Earth's annual global mean energy budget," *Bulletin of the American Meteorological Society*, Vol. 78, No. 2, pp. 197–208, 1997.
- [3] A. P. Babichev, N. A. Babushkina, A. M. Bratkovskii, *et al.*, "Physical values: Handbook energoatomizdat," I. S. Grigor'eva and E. Z. Melikhova, Ed., Moscow, Russian, 1991.
- [4] S. Arrhenius, "On the influence of carbonic acid in the air upon the temperature of the ground," *Philosophical Magazine and Journal of Science*, Vol. 5, No. 41, pp. 237–276, 1896.
- [5] C. N. Hewitt and A. V. Jackson, "Handbook of atmospheric science: Principles and applications," C. N. Hewitt and A. V. Jackson, Ed., Blackwell Publishing, 2003.
- [6] G. V. Chilingar, L. F. Khilyuk, and O. G. Sorokhtin, "Cooling of atmosphere due to CO₂ emission," *Energy Sources, Part A: Recovery, Utilization and Environmental Effects*, Vol. 30, pp. 1–9, 2008.
- [7] K. E. Trenberth, J. T. Fasullo, and J. T. Keihl, "Earth's global energy budget," *Bulletin of the American Meteorological Society*, Vol. 90, No. 3, pp. 311–323, 2009.

Analysis of the Electromagnetic Pollution for a Pilot Region in Turkey

Özgür Genç, Mehmet Bayrak, Ercan Yaldiz

Faculty of Engineering and Architecture, Department of Electrical and Electronics Engineering, Selçuk University, Konya, Turkey.
Email: erylaldiz@gmail.com, ozgurgenctr@yahoo.com

Received November 10th, 2009; revised December 11th, 2009; accepted December 15th, 2009.

ABSTRACT

In this paper, electromagnetic (EM) pollution (or radiation) measurements in a transmitter region were performed and statistical analysis of values recorded for the EM sources causing pollution was carried out. The actual measurement values and the estimated values by the analysis model obtained through the statistical analysis were compared. EM radiation levels were measured in the districts of Turkish capital Ankara where cellular base stations and TV/Radio stations are densely populated. EM Radiation (EMR) levels were measured for the GSM900, GSM1800, UHF4, VHF4 and VHF5 stations for certain spectrum ranges under far-field conditions by utilizing isotropic field probe and selective spectrum analyzer. The obtained measurement levels were compared with the limit values given by International Commission for Non-Ionizing Radiation Protection (ICNIRP). The results are discussed, regarding both the obtained values that influence the measurements.

Keywords: Electromagnetic Pollution, Statistical Analysis, Electromagnetic Radiation

1. Introduction

The use of EMR for communication increased significantly in the recent years (radio, television and cellular) and consequently the environmental level of EMR has increased. The massive proliferation of mobile communications equipment raised a special concern regarding the safety of population and personnel exposed to radiofrequency (RF) radiation emitted by either the base-station antennas [1].

The potential health effects of EMR from the transmitters for broadcasting of radio/TV and mobile communication are the subject of on-going researches [2,3] and a significant amount of public debate. The distribution and levels of EM pollution in the crowded residential areas are very important.

Exposure standards for RF region of EM spectrum, applicable at national or international level give for the UHF and VHF band of interest the RMS electric field strength maximum accepted values as reference levels for occupational or population exposure [1] in the far field region of the sources.

EM pollution measurements within the scope of this study were executed in a chosen pilot region, the city centre of Ankara, Turkey. The measurements were specifically in Dikmen Caldagi Hill transmitter region where many EM pollution sources are located.

In the present, there are three public mobile communication operators in Turkey: Vodafone (GSM 900 MHz), Turkcell (GSM 900 MHz), AVEA (GSM 1800 MHz or DCS 1800 MHz).

From the statistical analysis of the measurement results, EM radiation levels can be modeled through various calculations and formulas retrieved under certain conditions and within acceptable correctness. EM pollution measurement results are examined by means of time series analysis whether these results are suitable for predicting through the created model. Estimation or determination of the dependant variable *total EM pollution* is realized as based on the modeling.

2. Measurement of EM Pollution

In this EM pollution measurement study; it is assumed that only far field conditions exist for the cellular (GSM900 and GSM1800), TV and radio transmitters since these installations are most of the time mounted on high towers or hills.

It is essential to measure the combined field levels for all different signal sources in the environment like as shown **Figure 1**. In practice, many of the directional antennas with high gains are not suitable for this purpose since they don't allow measurements of signals from all directions and different polarizations and therefore not



Figure 1. Some EM pollution sources in the measurement areas

allowing quick measurements. The system we used is designed for measurements of the *E*-field strength. This ensures that optimum settings are used and allows evaluation according to single frequencies, complete services and total emission. Since the tri-axis sensor (antenna) has got an isotropic characteristic, the measurement is done independent from direction or polarization of the emitter [1].

In the measurements, the wide band spectrum (75 MHz – 3 GHz) antenna probes that can measure from all directions and different polarizations [4,5,6] were used.

The measurements were fulfilled by using NARDA SRM3000 radiation meter with isotropic antenna that can be utilized in 75 MHz – 3 GHz frequency range. The measurement system comprises of an isotropic broad band antenna that is connected via combiner to a portable spectrum analyzer. The electric field probe was based at 2m height from the ground level. The EMR meter was interfaced with a portable computer. Measurement results recorded by using SRM3000 were saved to a computer [5]. Random measurements were performed in the transmitter region, far from GSM base station and radio/TV transmitters in far-field points. The antenna was mounted on a tripod. The signal from the EMR meter is expressed in Volt units convertible to electric field strengths (V/m) using the antenna factor parameter. All measurements were divided according to their relevant frequencies into groups (Radio, TV, Cellular, etc). For each measurement E_{average} (V/m) was recorded [8]. The duration of each measurement was 6 minutes [7,8]. The experimental set-up is depicted in Figure 2.

The measurements include the sources listed in Table 1 and the other sources within the spectrum up to 3 GHz.

3. Statistical Analysis of EM Pollution Measurements

The measurement results are analyzed by means of the SPSS 17.0 and E-views software. Firstly, stability of the obtained time series was examined using Dickey-Fuller (D-F) test in order to determine if the time series are suitable for estimation. In the second stage, the relationship between the variables was examined using correlation and regression analyses. Finally, variance analysis

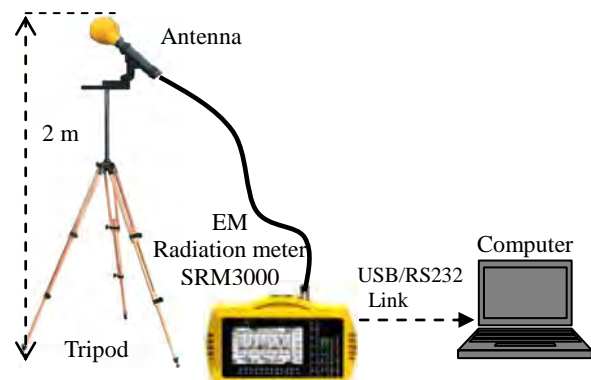


Figure 2. Equipment used for the measurements

Table 1. Measured EM pollution sources and their frequency ranges

EM Source	Frequency Range
UHF5	605-861 MHz
VHF4	174-230 MHz
UHF4	605-861 MHz
GSM900	870-960 MHz
GSM1800	1.77-1.85 GHz

was utilized to determine the model's significance and the prediction model for total EM pollution was obtained.

A time series is a group of measurement results recorded over a time for a certain variable in hand. The purpose of this analysis related to time series is to understand the reality represented by the observation set and determination of the predicted values of the variables in the time series. First step of predicting is to test the stability of the series. If the average or variance of the time series does not present a symmetrical change or the series is free of periodical fluctuations, these series are called "stable time series" [9]. D-F test is utilized for stability tests.

3.1 Dickey-Fuller Unit Root Test

Unit root test analyses are applied for each time series of different measurement variables (GSM900, GSM1800, etc.) by using Equation (1) which is also utilized when testing the stability of series using D-F test [10].

$$\Delta Y_t = \beta_1 + \beta_2 t + \delta Y_{t-1} + \sum_{i=1}^m \alpha_i \Delta Y_{t-i} + \varepsilon_t \quad (1)$$

In Equation.1, Δ is the first difference processor and represents the difference between two consecutive values. Here, ε_t is the consecutive independent probable error term with zero average and unchanged σ^2 variance and conforms to classic assumptions. $\delta = \rho - 1$ and ρ is a significance coefficient. If $\rho = 1$, then constant of Y_{t-1} becomes zero and this indicates that the time series is un-

stable meaning that it does not have a unit root. β_1 is a constant and β_2 is the coefficient at t time. t represents trend and m is maximum delay [9,10]. Whether the series has a unit root while using D-F test or not are determined by trying the following hypothesis.

$H_0: \rho = 1$ or $\delta = 0$ (Series has unit root, are not stable)

$H_1: \rho < 1$ or $\delta < 0$ (Series does not have unit root, are stable).

Critical values for testing stability are the τ statistical values calculated by the D-F method. Acceptable limits (critical values) of this test according to the 5% level are calculated according to the Monte Carlo Simulation by MacKinnon. These values are called *MacKinnon critical values*. Known t statistics calculated by the statistical analysis programs are called τ statistics or *D-F test statistics* in this hypothesis test [10].

If the D-F test statistics' absolute values are smaller than the MacKinnon Critical Values' absolute values, H_0 hypothesis is accepted and this indicates that the series is not stable. If the D-F tests statistics' absolute values are greater than the MacKinnon Critical Values' absolute values, H_0 hypothesis is rejected and this indicates that the series is stable. If the original state of the series is not stable, first difference of the series is taken and the D-F test is applied again. If this is also not stable, second difference of the series is taken and the D-F test is re-applied [9,10].

According to the results in **Table 2**; when examined the values of each series, absolute values of τ statistics are greater than the absolute values of the critical values at 5% significance level. Therefore, the H_0 hypothesis is rejected for the level values of each series examined [9]. In other words, all of the series (Total, GSM900, etc.) do not have unit root at level and are called stable. Using these data multiple regression can be utilized and future predictions can be made.

3.2 Regression and Correlation Analysis

Regression analysis is an analysis method used to examine the relation between a dependant variable and one or more independent variables [11]. With multiple regression the relation between a dependant variable Y and more than one independent variables (X_1, X_2, \dots, X_n) is examined (Equation (2)).

Multiple Linear Regression Model: If Y is total EM pollution value, multiple linear regression model is given by

$$Y = \beta_0 + \beta_1\chi_1 + \dots + \beta_n\chi_n + \varepsilon \quad (2)$$

where β_0 is a constant, β_1 is the correlation coefficient of 1st variable, χ_1 is the actual measurement value of the 1st variable, and ε is the error term.

The slope direction and the degree of the relationship among the variables contributing to the EM pollution in the environment are examined analytically by means of

the correlation test and comparisons of the variable pairs. The influences of variables to each other are analyzed as shown in Table 4 for this study.

As shown in **Table 3**, total pollution value was recorded average **3.658** V/m and its standard deviation was **0.538** according to the 68 measurement results taken from various locations in the city centre. GSM1800 average pollution value was calculated **1.276** V/m while GSM900 average pollution value was **0.102** V/m.

According to **Table 4**, VHF4 was found being the highest correlation relation of **0.606** with total variable. UHF5 was the second highest variable with correlation of **0.583**.

Table 2. D-F unit root test results for series

Series	D-F Test (τ) Value	Critical Value
Total	4.042	3.482
UHF5	4.452	3.478
VHF4	4.779	3.478
UHF4	5.886	3.478
GSM900	4.358	3.479
GSM1800	5.058	3.478
Others	5.879	3.478

Table 3. Descriptive statistics related to the variables

Series	Average E Value (V/m)	Standard Deviation
Total	3.658	0.538
UHF5	2.395	0.693
VHF4	1.514	0.303
UHF4	1.583	0.795
GSM900	0.102	.0364
GSM1800	1.276	0.587
Others	0.252	0.005

Table 4. Correlation related to the variables

Correlation	Total	VHF4	UHF4	UHF5	GSM900	GSM1800	Others
Total	1.000	0.606	-0.103	0.583	0.553	-0.462	-0.025
VHF4	0.606	1.000	-0.001	-0.131	0.460	-0.294	-0.098
UHF4	-0.103	-0.001	1.000	-0.421	-0.393	0.410	-0.082
UHF5	0.583	-0.131	-0.421	1.000	0.568	-0.660	0.053
GSM900	0.553	0.460	-0.393	0.568	1.000	-0.808	-0.052
GSM1800	-0.462	-0.294	0.410	-0.660	-0.808	1.000	-0.087
Others	-0.025	-0.098	-0.082	0.053	-0.052	-0.087	1.000

Functional form of the relation between the variables is examined using regression analysis and its reliability degree is determined using correlation analysis. In **Table 5**, R^2 multiple certainty factor and corrected multiple certainty factor $R^2_{corrected}$ are used to determine the best regression model.

Model's explanation strength is determined using the R^2 multiple certainty factor. R^2 value is a measure indicating what percentage of the total variation of a dependant variable can be explained by variations of the independent variables [11].

Durbin Watson test is utilized while testing the assumption of successive dependency (autocorrelation) between the data set observations requirement in order to apply the multiple linear regression method. R^2 which is an indication of how good the independent variables describe the dependant variable was **92.7% (0.927)** meaning that the EM pollution changes by **92.7%** depending on these factors. R^2 increases by adding more variables to the model, but this alone is not sufficient for testing the significance of the model. If the Durbin Watson Value is between **1.5** and **2.5**, then autocorrelation does not exist and the prediction model is considered as deterministic [10]. Durbin Watson test statistics being **2.003** indicates absence of autocorrelation.

3.3 Variance Analysis and t Test

Significance column value (or p value) of variance analysis table (**Table 6**) indicates that the relationship between the variables is statistically significant if it is at ($p < 0.05$) level. The model's overall significance is tested by F test [9]. Hypothesis:

H_0 : Coefficients are greater than 0.05. The model is not significant.

H_1 : Coefficients are little than 0.05. The model is significant.

If the relationship in **Table 6** is formulized, the probability value F calculated according to $p = 0.05$ is

Table 5. Regression model summary for significance test

R	R^2	Corrected R^2	Std. Error of the Estimation	Durbin-Watson
0.963	0.927	0.920	0.15207	2.003

Table 6. Variance analysis

	Sum of Squares	Degree of Freedom	Mean Square	F	p
Regression	17.948	6	2.991	129.35	0.00
Residual	1.411	61	0.023		
Total	19.359	67			

$p = \mathbf{0.000} < 0.05$, then the H_0 hypothesis is rejected and the model is called to be significant.

The test is applied for significance of the coefficients in the regression model and the insignificant values are taken off from the model. For this purpose, t test is applied. When the t values which calculated according to $p = 0.05$ in **Table 7** are tested, the H_0 hypothesis is rejected for each coefficient.

H_0 : Regression coefficients are greater than 0.05. Relationship is not significant.

H_1 : Regression coefficients are little than 0.05. Relationship is significant.

Whether the significance level of independent variables is sufficient for the model or not is decided by looking at the p probability values. If $p < 0.05$, then the variable effects the dependent variable and is included to the model, otherwise it is assumed that it does not statistically effect the dependent variable and is not included in the model [9].

According to the results retrieved from the environmental measurements values, since the probability values (p values) of VHF4, UHF4, UHF5 and GSM1800 variables are smaller than **0.05**, they are included to the

Table 7. Variable coefficients for EM pollution analysis model

Variable	Unstandardized Coefficients		Standardized Coefficients	t	p
	Beta	Standard Error	Beta		
Constant	-0.233	0.191		-1.036	0.304
VHF4	0.707	0.036	0.911	19.512	0.000
UHF4	0.283	0.070	0.159	4.049	0.000
UHF5	0.723	0.037	1.070	19.508	0.000
GSM900	-1.847	1.018	-0.125	-1.814	0.075
GSM1800	0.321	0.061	0.351	5.289	0.000
Others	5.593	4.478	0.044	1.249	0.216

model, but it is concluded that the GSM900 and Others variables are not significant for the model. As shown in **Table 7**, GSM900 and Others variables' p probability values are respectively **0.75**, **0.216** and are greater than **0.05**. Hence, they can not be included to the prediction model. The multiple regression model is obtained as the following:

$$\text{Total EM pollution value} = -0.233 + 0.707.VHF4 + 0.283.UHF4 + 0.723.UHF5 + 0.321.GSM1800 \quad (3)$$

The independent variables that affect the total variable were tested using the multiple linear regression analysis, were included to the model, and were studied. According to the data collected during the measurements, the effect of VHF4 frequencies to the overall total pollution is around **0.707**. The effect of UHF4 to the total pollution is **0.283**, UHF5 is **0.723**, GSM1800 is **0.321**.

It is necessary that the errors are distributed normally in order to the obtained model to be significant. It is concluded that the distribution of the total pollution errors are normal since the measurement values are scattered around a 45° linear line when tested with the Probability-Probability (P-P) graphics method. A probability plot is a graphical technique for comparing two data sets, either two sets of empirical observations, one empirical set against a theoretical set, or more rarely two theoretical sets against each other [12,13]. Distribution of the values for the estimated regression models is shown in **Figure 3**.

The estimated model is valid when the observed and expected values' distribution is examined.

3.4 Comparison of the Measurement Results by Means of Statistical Model

As a result of the D-F unit root tests applied to the measurements taken from the measurement region in general, the H_0 hypothesis is rejected for level values of each series examined (as shown in **Table 8**). This indicates that the series do not have unit root at the level and are stable. Consequently, it is possible to utilize multiple regressions using the obtained results and it is concluded that predictions for future can be made.

The calculated value by the model (Equation (3)) is **3.96 V/m** while the actual total pollution value is **4.094 V/m** (as shown in **Table 8**). Hence, the prediction model is significant and valid when examined the observed and predicted values' distribution. Having valid models obtained for the measurement regions indicates that the EM pollution values are suitable for prediction future pollution levels. The studies indicated that very close values are recorded when compared the prediction result of the model obtained from the analysis made by using the SPSS17.0 analysis program and the actual measurement results.

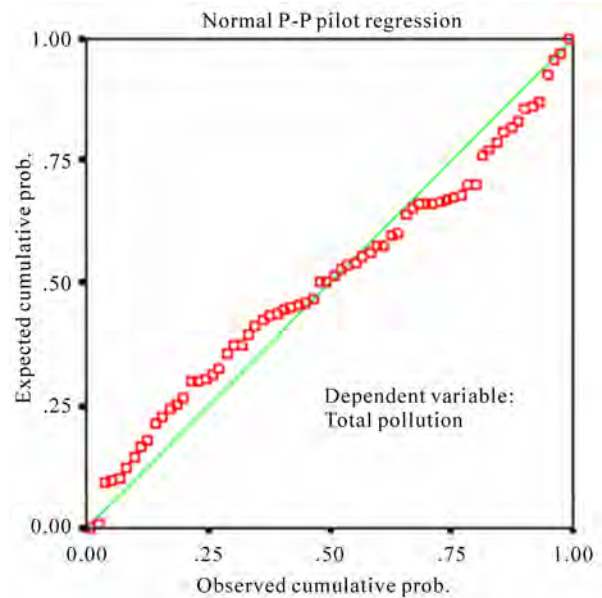


Figure 3. Observed and expected cumulative probability graphics for total EM pollution

Table 8. Sample comparison of environmental measurement results

Variable	Measured Electrical Field Levels (V/m)				
	1	2	3	4	5
VHF4	2.9	2.59	2.87	2.38	2.32
UHF4	2.085	1.51	1.69	1.2	1.5
UHF5	1.6	1.68	0.94	1.02	1.26
GSM900	0.071	0.072	0.120	0.071	0.074
GSM1800	1.234	1.38	1.48	1.96	2.32
Others	0.243	0.245	0.247	0.245	0.246
Measured total	4.094	3.885	3.023	3.384	3.532
Model total	3.960	3.683	3.429	3.156	3.487

4. Conclusions

The study involved **68** measurements to determine the EM field levels in Dikmen Caldagi Hill transmitter region in the Ankara city centre. The precise experimental determination of E -field of RF radiation in a complex environment is a difficult task. This is mainly due to the existence of three fundamental physical properties of electromagnetic waves: reflection, absorption and interference. Under uncontrolled conditions, for instance in a complicated environment, different measurements can lead to quite different results due to changing conditions.

Moreover, the settings of the measurement equipment may affect sensible the measured values [1].

As shown in Table 3, total pollution value was recorded as average **3.658** V/m and its standard deviation was **0.538** according to the **68** measurement results taken from various locations in the city centre. GSM1800 average pollution value was calculated as **1.276** V/m and its standard deviation was calculated **0.587**. GSM900 average pollution value was **0.102** V/m and its standard deviation was calculated **0.0364**. The electric field level of GSM900 base stations were measured maximum **0.483** V/m and minimum **0.078** V/m during the measurements. For GSM1800, maximum **2.32** V/m and minimum **0.09** V/m electric field levels were measured. Average total pollution values were measured as maximum **5.21** V/m and minimum **2.53** V/m. VHF4 average pollution value was found being the highest correlation relation of **0.606** with total EM pollution value. GSM900 average pollution value was found **0.553** correlation relation with total value. In other words, total EM pollution is affected by **55.3%** due to variation in pollution of GSM900 and by **46.2%** for GSM1800.

Results indicated that the EM pollution levels were below the **41.25** V/m limit for 900 MHz and **58.34** V/m limit for 1800 MHz according to ICNIRP's recommendations [14].

REFERENCES

- [1] S. Miclausi and P. Bechet, "Estimated and measured values of the RF radiation power density around cellular base stations," *Environment Physics*, Bucharest, Vol. 52, No. 3, pp. 429–440, 2007.
- [2] B. I. Wu, A. I. Cox, and J. A. Kong, "Experimental methodology for non-thermal effects of electromagnetic radiation on biologics," *Journal of Electromagnetic Waves and Applications*, Vol. 21, No. 4, pp. 533–548, 2007.
- [3] C. Giliberti, F. Boella, *et al.*, "Electromagnetic mapping of urban areas: The example of Monselice (Italy)," *PIERS Online*, Vol. 5, No. 1, pp. 56–60, 2009.
- [4] A. R. Ozdemir, "Radio frequency electromagnetic fields levels in urban areas of Istanbul, Ankara and Izmir and protection techniques," Thesis for Expertise, Telecommunication Society, Ankara, Turkey, 2004.
- [5] A. Shachar, R. Hareuveny, M. Margalio, and G. Shani, "Measurements and analysis of environmental radio frequency electromagnetic radiation in various locations in Israel," Soreq Nuclear Research Center, Israel, 2004.
- [6] K. Voudouris and P. Grammatikakis, "Radiation measurements at short wave antenna park," Department of Electronic, Technological Educational Institute of Athens, Athens, 2005.
- [7] R. Hamid, M. Cetintas, *et al.*, "Measurement of electromagnetic radiation from GSM base stations," *IEEE International Symposium on EMC, TUBITAK-UME*, Gebze, 2003.
- [8] P. Getsov, D. Teodosiev, *et al.*, "Methods for monitoring electromagnetic pollution in the Western Balkan environment," *SENS'2007, 3rd Scientific Conference with International Participation Space, Ecology, Nanotechnology, Safety*, Varna, 2007.
- [9] D. Gujarati, "Basic econometrics," Literature Publishing, Turkey, 2001.
- [10] M. Sevuktekin and M. Nargelecekenler, "Time series analysis," Nobel Publishing, Turkey, 2005.
- [11] H. Emec, "Time series econometry I: Stability, unit roots," IIBF, Dokuz Eylul University, Izmir, 2007.
- [12] H. C. Thode, "Methods of probability plotting," CRC Press, 2006.
- [13] J. Gibbons and S. Chakraborti, "Nonparametric statistical inference," 4th Ed., CRC Press, 2003.
- [14] ICNIRP, "Guidelines for limiting exposure to time-varying electric, magnetic and electromagnetic fields (up to 300 GHz)," *Health Physics*, Vol. 74, No. 4, pp. 494–522, 1998.

Modeling of Multi-Pulse VSC Based SSSC and STATCOM

Pavel Zuniga-Haro¹, Juan Manuel Ramirez²

¹Graduate Program in Electrical Engineering, CUCEI University of Guadalajara, Guadalajara, Mexico; ²Power Systems Department, CINVESTAV, Guadalajara, Mexico.

Email: pavel.zuniga@cucei.udg.mx, jramirez@gdl.cinvestav.mx

Received October 27th, 2009; revised November 16th, 2009; accepted November 19th, 2009.

ABSTRACT

The aim of this paper is to contribute to the dynamic modeling of multi-pulse voltage sourced converter based static synchronous series compensator and static synchronous compensator. Details about the internal functioning and topology connections are given in order to understand the multi-pulse converter. Using the 24 and 48-pulse topologies switching functions models are presented. The models correctly represent commutations of semiconductor devices in multi-pulse converters, which consequently allows a precise representation of harmonic components. Additionally, time domain models that represent harmonic components are derived based on the switching functions models. Switching functions, as well as time domain models are carried out in the original abc power system coordinates. Effectiveness and precision of the models are validated against simulations performed in Matlab/Simulink®. Additionally, in order to accomplish a more realistic comparison, a laboratory prototype set up is used to assess simulated waveforms.

Keywords: Commutations, Harmonics, Multi-Pulse, Modeling, SSSC, STATCOM

1. Introduction

Most of the existing converter based Flexible AC Transmission Systems (FACTS) devices rated above 80MVAR use either 24 or 48-pulse converters [1–5], because they exhibit several advantages over other Voltage Sourced Converter (VSC) configurations. Some of the key advantages include harmonic content, switching frequency and dc capacitor rating.

The harmonic content of the output voltage generated by a multi-pulse converter is low; the converter harmonic components are in the order of $n = 6km \pm 1$, where $m = 0, 1, 2, \dots$, and k is the number of 6-pulse units used to construct the VSC. The harmonic amplitudes of these components are $2k/n\pi$ times the dc side voltage magnitude used by the converter. This reduces the harmonics injected by the VSC to the power system. In comparison to other VSC topologies the multi-pulse converter has a superior total harmonic distortion for a given number of semiconductor switches [6].

The switching frequency of the commutating devices for a power converter is severely limited and must be kept low. The multi-pulse converter has the same switching frequency as the fundamental frequency of the output voltage, which is also very low, 60 Hz

switching frequency for a 60 Hz utility voltage. This limits the switching losses as well as the heat in the commutating devices.

The rated voltage of the dc capacitor is low, which reduces physical volume of the multi-pulse VSC in favor of economical considerations. The capacitor voltage ripple decreases as the number of pulses of a given configuration increase; therefore, in high pulse configurations the dc capacitor rating can be reduced without compromising the ripple level of the dc voltage.

Frequently, the multi-pulse VSC dynamic models used are the $dq0$ [5–12], and the Fundamental Frequency (FF) models in abc coordinates [5–9]. $dq0$ models are widely used due to simplification of model computations specially when working with the synchronous generator, because they convert balanced three phase sinusoidal signals into constants. The set of abc quantities are transformed into a synchronously rotating reference frame using the so called $dq0$ or Park's transformation; as a result, the inverse transformation is needed if the phase quantities have to be obtained from $dq0$ signals. On the other hand three phase models are derived directly from the system; therefore, the obtained signals are in their original abc coordinates. FF models represent VSC's with fundamental frequency components only and do not take into

This work was supported in part by PROMEP under grant 103.5/09/1420.

account harmonics in their signals. To overcome the lack of proper harmonic representation in simplified models, Switching Functions (SF) modeling in abc coordinates is accomplished, so as to obtain realistic characterization of VSC devices performance inserted in a power system. Moreover, reduced Time Domain (TD) models that also consider harmonic components are obtained using the derived SF models. In addition, since the SF and TD models include ac and dc side converter harmonics, control strategies as well as the power system, other controllers, system protections, etc. would be subjected to a more realistic interpretation of a VSC device than when using simplified models.

2. Multi-Pulse VSC Topology

The objective of a VSC is to generate three phase ac voltages using a dc voltage. The basic 6-pulse VSC configuration depicted in **Figure 1** shows asymmetric turn-off devices with a parallel diode connected in reverse [13]. The frequency and phase of the three phase voltages generated by the 6-pulse VSC configuration are determined by the gate pulse pattern (GPP) of the commutating devices shown in **Figure 2** [14]. The amplitude of the three phase ac voltages is determined by the magnitude of the dc voltage, v_{dc} . The *on-off* sequence depicted in **Figure 2** applied to the 6-pulse VSC shown in **Figure 1** results in phase, v_{a6} , and line, v_{ab6} , voltages for phase a like the ones exhibited in **Figure 3**. The harmonic components of these signals are in the order of $n = 6m \pm 1$, where $m = 0, 1, 2, \dots$, and the peak amplitude of the fundamental and harmonic components of v_{a6} and v_{ab6} are given by $v_{a6n} = 2v_{dc}/n\pi$ and $v_{ab6n} = 2\sqrt{3} v_{dc}/n\pi$, respectively.

Signals $gs_1, gs_2, gs_3, gs_4, gs_5$ and gs_6 are gate pulses of switches S_1, S_2, S_3, S_4, S_5 and S_6 in **Figure 1**, respectively. The gate signals can only take values of 0 or 1 for the switching devices to be *off* or *on*, respectively.

Inspecting **Figure 3** it can be seen that even though these 6-pulse voltages are ac waveforms, they are not sinusoidal; this is due to a high harmonic content present in them.

In order to reduce the harmonic content of the resulting voltages, higher pulse configurations are needed, so as to cancel specific harmonic components. These arrangements are achieved combining 6-pulse VSC's in order to produce an output voltage with reduced harmonics. The combination is made using transformer arrangements in a magnetic coupling circuit (MCC) and phase shifting transformer (PST). As a result, combining two 6-pulse VSC's a 12-pulse configuration is attained, two 12-pulse converters achieve a 24-pulse topology and two 24-pulse arrangements result in a 48-pulse VSC. The 24 and 48-pulse converter configurations are depicted in **Figure 4**.

To combine the output voltages of the two 6-pulse VSC's needed to achieve a 12-pulse configuration, a

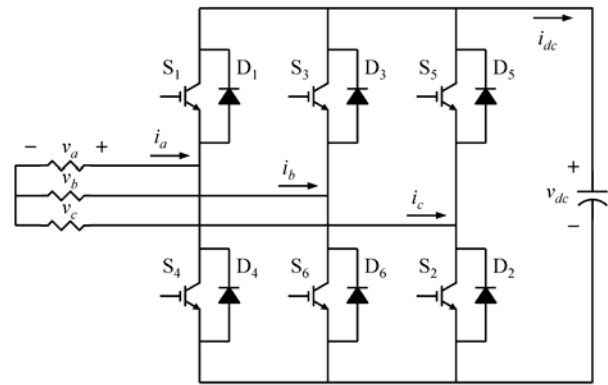


Figure 1. Configuration of 6-pulse VSC

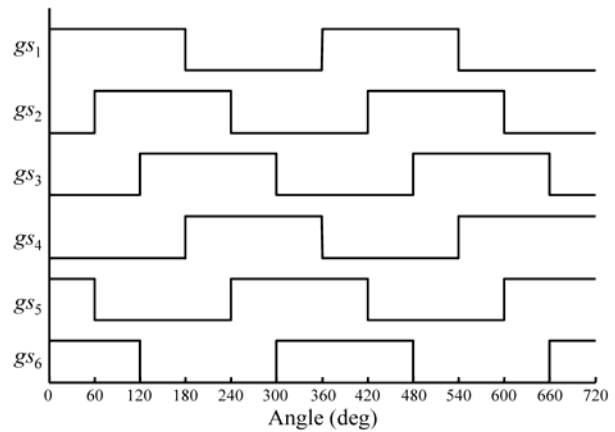


Figure 2. Gate pulse pattern of 6-pulse VSC

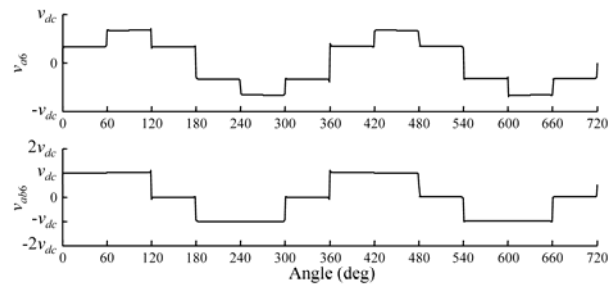


Figure 3. Phase and line voltages of 6-pulse VSC

MCC is needed in order to align and scale the harmonic components to be cancelled. The circuit consists of two transformers, a star-star (Y-Y) transformer with a turn ratio of 1:1 and a delta-star (Δ -Y) transformer with a turn ratio of $1:1/\sqrt{3}$. Also, the GPP of one VSC must lag 30° the phase angle of the other one. However, in order to obtain an appropriate output voltage, the combination of 6-pulse VSC's to construct 24 or 48-pulse converters is achieved via a MCC and PST's.

Due to the reduced harmonics of the 24 and 48-pulse VSC's, these are configurations suitable for connection to the power system [1–3].

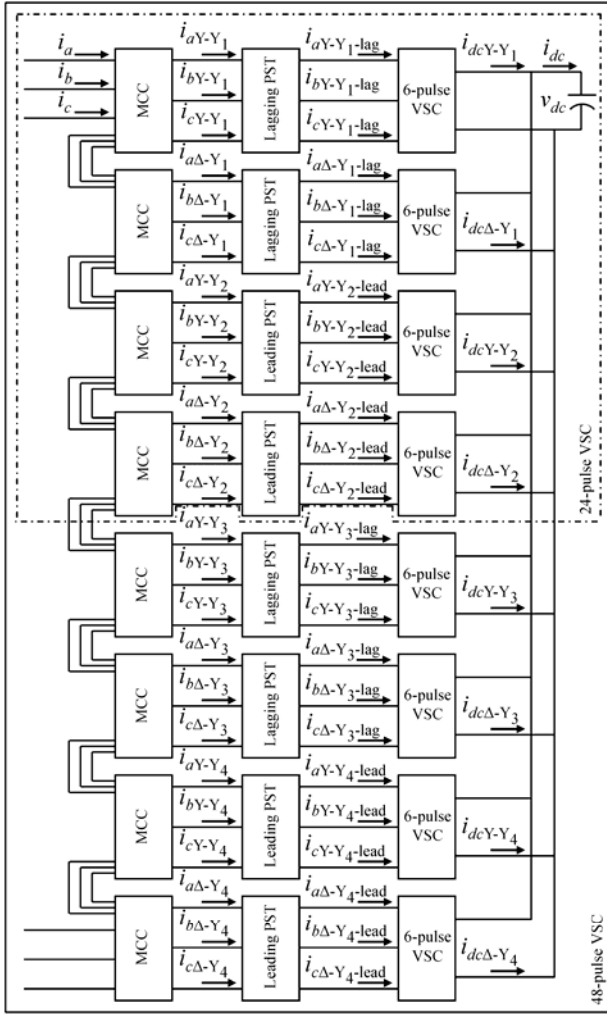


Figure 4. Topologies of 24 and 48-pulse VSC's

In order to create a 24 or 48-pulse waveform with a harmonic content of $n = 24m \pm 1$ or $n = 48m \pm 1$, respectively, where $m = 0, 1, 2, \dots$, the 6-pulse converters need relative phase displacements accomplished via the GPP that determines the angle of the resulting three phase output voltages. Also, PST's are needed connected in series with the phase voltages in the primary side of the MCC transformers to add voltage components in quadrature. These quadrature voltages are obtained from the three phase output voltages of each VSC. The relations that produce the desired phase shifts are given by,

$$\begin{aligned} v_a' &= v_a \pm v_{bc} \\ v_b' &= v_b \pm v_{ca} \\ v_c' &= v_c \pm v_{ab} \end{aligned} \quad (1)$$

where v_a' , v_b' and v_c' are the desired phase shifted voltages. The line voltages are added in order to generate a

lagging phase voltage and subtracted to create a leading one.

Voltages v_{bc} , v_{ca} and v_{ab} must have the specific amplitude to produce the desired phase shift angle; these amplitudes are determined by the transformation ratio of the PST's, given by $\zeta = \tan(\varphi)/\sqrt{3}$, where φ is the desired phase shift angle.

The analysis of the currents of the VSC topologies shown in Figure 4 is now addressed. The derivation of the expressions starts with the line currents, i_a , i_b and i_c flowing into the VSC and finishes with the derivation of the dc current, i_{dc} .

Let us begin from the basic 6-pulse VSC shown in Figure 1. To derive the currents flowing into the VSC it is necessary to account for the configuration of the coupling transformer.

Neglecting losses, the currents flowing in the secondary side equals the currents in the primary side in a Y-Y configuration; therefore, the line currents match the VSC currents,

$$i_{nY-Y} = i_n \quad (2)$$

where $n = a, b, c$.

Once these currents are derived, the capacitor current, i_{dc} , is determined. The dc current is constructed adding segments of line currents [7]. The segments depend on which switch-diode, S-D, pair is conducting. Analyzing the upper S-D pairs of the 6-pulse VSC shown in Figure 1, it is observed that pairs S_1 - D_1 , S_3 - D_3 and S_5 - D_5 participate in i_{dc} , thus,

$$i_{dc} = g_{s1} i_a + g_{s3} i_b + g_{s5} i_c \quad (3)$$

The above is a simple procedure useful for the analysis of higher pulse arrangements. Using this procedure and considering the configuration of the MCC, the 12-pulse current is obtained.

In the Δ -Y arrangement both the configuration and the turn ratio must be taken into account. Neglecting losses, the currents flowing out of the Δ -Y configuration are derived using the following relations,

$$\begin{aligned} i_{a\Delta-Y} &= \frac{i_a - i_c}{\sqrt{3}} \\ i_{b\Delta-Y} &= \frac{i_b - i_a}{\sqrt{3}} \\ i_{c\Delta-Y} &= \frac{i_c - i_b}{\sqrt{3}} \end{aligned} \quad (4)$$

where $i_{a\Delta-Y}$, $i_{b\Delta-Y}$ and $i_{c\Delta-Y}$ are the currents flowing out of the Δ -Y arrangement.

Since the currents flowing out of the MCC are the ones entering the 6-pulse units, these are used to obtain the two 6-pulse dc currents that shape the 12-pulse capacitor current.

Using (3) in each of the two 6-pulse units both components of the 12-pulse dc current are calculated, which together become the 12-pulse capacitor current, given by,

$$i_{dc} = i_{dcY-Y} + i_{dc\Delta-Y} \quad (5)$$

where i_{dcY-Y} and $i_{dc\Delta-Y}$ are the 6-pulse dc currents flowing out of the Y-Y and Δ -Y transformers, respectively.

To derive the 24-pulse VSC currents, not only the MCC, but also the PST's have to be included.

The 24-pulse VSC is constructed with two 12-pulse VSC's, therefore the MCC operates using two Y-Y and two Δ -Y transformers. To calculate the currents of each Y-Y and Δ -Y transformer the same procedure as for the 12-pulse SSSC is carried out, therefore (2) and (4) are used. The effect of each PST has to be considered for the currents of the Y-Y and Δ -Y transformers as follows.

For the lagging configuration of the corresponding PST's the relations are given by,

$$\begin{aligned} i_{aY-Y-lag} &= i_{aY-Y} + \xi i_{cY-Y} - \xi i_{bY-Y} \\ i_{bY-Y-lag} &= i_{bY-Y} + \xi i_{aY-Y} - \xi i_{cY-Y} \\ i_{cY-Y-lag} &= i_{cY-Y} + \xi i_{bY-Y} - \xi i_{aY-Y} \end{aligned} \quad (6)$$

where ξ is the transformation ratio to achieve the desired phase shift angle; i_{aY-Y} , i_{bY-Y} and i_{cY-Y} are currents that come out of the Y-Y coupling transformers but can be interchanged for currents from the Δ -Y coupling transformers as needed; $i_{aY-Y-lag}$, $i_{bY-Y-lag}$ and $i_{cY-Y-lag}$ are currents that come out of the PST's in the lagging configuration connected to the Y-Y coupling transformers.

For the leading configuration of the corresponding PST's the relations are shown below,

$$\begin{aligned} i_{aY-Y-lead} &= i_{aY-Y} + \xi i_{bY-Y} - \xi i_{cY-Y} \\ i_{bY-Y-lead} &= i_{bY-Y} + \xi i_{cY-Y} - \xi i_{aY-Y} \\ i_{cY-Y-lead} &= i_{cY-Y} + \xi i_{aY-Y} - \xi i_{bY-Y} \end{aligned} \quad (7)$$

where $i_{aY-Y-lead}$, $i_{bY-Y-lead}$ and $i_{cY-Y-lead}$ are the currents that come out of the PST's in the leading configuration connected to the Y-Y coupling transformers. The currents coming out of the PST's in both cases are the VSC currents. Now the contribution of each VSC to i_{dc} can be derived and is given by,

$$i_{dc} = i_{dcY-Y1} + i_{dc\Delta-Y1} + i_{dcY-Y2} + i_{dc\Delta-Y2} \quad (8)$$

For the 48-pulse VSC, the configuration has to be taken into account as shown in **Figure 4**, however, the relations that apply to the 24-pulse converter also are valid for the 48-pulse topology. The contribution of each VSC to the capacitor current can be derived and is given by,

$$i_{dc} = \sum_{i=1,4} (i_{dcY-Yi} + i_{dc\Delta-Yi}) \quad (9)$$

The calculation of the VSC currents is made backwards, starting from the capacitor current equation and

substituting the appropriate relations based on the line currents. The procedure is explained now step by step:

- 1) - Use the i_{dc} Equation, (8) for the 24-pulse VSC.
- 2) - Substitute in i_{dc} the corresponding current contribution of each 6-pulse unit, based in (3).
- 3) - For the 24-pulse VSC, the line currents are not used in (3), instead, the currents used are the ones flowing out of the PST's depending on the configuration needed; the Equations used for these currents are (6) and (7) for the lagging and leading configurations, respectively.
- 4) - Finally, substitute the corresponding currents flowing into the PST's in terms of the line currents as given by (2) and (4) for the Y-Y and Δ -Y configurations, respectively.

A similar procedure is used for the 48-pulse VSC currents, taking into account the appropriate relations.

Calculation of the voltages is achieved in a similar manner as derivation of the currents. Therefore, the MCC, PST's and GPP have to be taken into account. For a thorough description of 24 and 48-pulse VSC's refer to [15,16].

3. Multi-Pulse VSC Modeling

The multi-pulse VSC arrangements shown in **Figure 4** are the building blocks of several FACTS devices, including the ones presented in this article.

The proposed mathematical models are derived using equivalent circuits for Static Synchronous Series Compensator (SSSC) and Static Synchronous Compensator (STATCOM). The connection of the devices to the power system depends on the type of compensation needed. The modeling of the devices is similar because their building block is the VSC; the difference is in their connection to the power system.

The main function of the SSSC is to provide series reactive compensation of transmission lines in order to regulate power flow; therefore, it is connected in series to a transmission line. The STATCOM major purpose is to provide shunt reactive compensation of voltage nodes in order to regulate voltage magnitudes; hence, it is shunt connected to a voltage node.

The control variable of the VSC, regardless of the connection to the power system and the multi-pulse configuration, is the phase angle applied to the gate pulse pattern of the commutating devices.

The modeling of SSSC and STATCOM take into account the number of 6-pulse VSC units in each multi-pulse configuration by considering the gate pulse pattern applied, as well as magnetic coupling circuit arrangement and phase shifting transformers.

3.1 Switching Functions Modeling

The SSSC model is derived using the system of **Figure 5**. The figure shows the SSSC equivalent circuit connected in series to a transmission line. The SSSC injected volt-

ages are denoted by v_{ase} , v_{bse} and v_{cse} . Parameters R_{se} and L_{se} represent the common influence of both, series MCC and transmission line between sending and receiving end nodes denoted by subscripts s and r , respectively. The dc side of the SSSC is represented by a current source connected to a capacitor. Shunt connection of a resistance enables representation of converter losses.

From **Figure 5** the equations that describe the currents of phases a , b and c are expressed as,

$$\frac{di_{nse}}{dt} = \frac{1}{L_{nse}}(v_{sn} - v_{rn} - v_{nse}) - \frac{R_{nse}}{L_{nse}}i_{nse} \quad (10)$$

$n=a, b, c$

For the dc circuit the expression that describes the behavior of the dc voltage is given by,

$$\frac{dv_{dc}}{dt} = \frac{1}{C}i_{dc} - \frac{1}{CR_C}v_{dc} \quad (11)$$

In order to derive the SF models, the configuration of the VSC, MCC and PST's, as well as the GPP of the commutating devices have to be taken into account.

Let us begin from the basic 6-pulse VSC shown in **Figure 1**. To derive the 6-pulse SSSC SF model, the 6-pulse output voltages and the corresponding capacitor current need to be substituted in (10–11).

The SF model takes into account the 6-pulse converter gate signals shown in **Figure 2**.

Considering the GPP of **Figure 2**, the line and phase voltages of a 6-pulse VSC in terms of its gate signals yield,

$$\begin{aligned} v_{ab} &= (gs_1 - gs_3)v_{dc} \\ v_{bc} &= (gs_3 - gs_5)v_{dc} \\ v_{ca} &= (gs_5 - gs_1)v_{dc} \end{aligned} \quad (12)$$

and

$$\begin{aligned} v_a &= \frac{2gs_1 - gs_3 - gs_5}{3}v_{dc} \\ v_b &= \frac{2gs_3 - gs_1 - gs_5}{3}v_{dc} \\ v_c &= \frac{2gs_5 - gs_1 - gs_3}{3}v_{dc} \end{aligned} \quad (13)$$

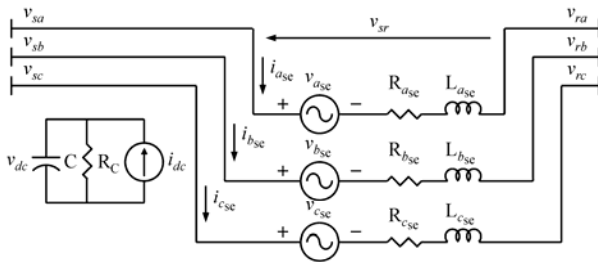


Figure 5. SSSC equivalent circuit connected in series to a transmission line

These are the switching functions voltages present in a VSC like the one shown in **Figure 1**.

Substituting the 6-pulse voltages of (13) in (10) and the 6-pulse capacitor current of (3) in (11) and arranging in state space form, the 6-pulse SF model results,

$$\frac{d}{dt}\mathbf{x}_{se}^{SF} = \mathbf{A}_{se}^{SF}\mathbf{x}_{se}^{SF} + \mathbf{B}_{se}^{SF}\mathbf{u}_{se}^{SF} \quad (14)$$

$$\mathbf{x}_{se}^{SF} = \begin{bmatrix} i_{ase} \\ i_{bse} \\ i_{cse} \\ v_{dc} \end{bmatrix}, \quad \mathbf{u}_{se}^{SF} = \begin{bmatrix} v_{sra} \\ v_{srb} \\ v_{src} \\ 0 \end{bmatrix}$$

$$\mathbf{B}_{se}^{SF} = \begin{bmatrix} \frac{1}{L_{ase}} & 0 & 0 & 0 \\ 0 & \frac{1}{L_{bse}} & 0 & 0 \\ 0 & 0 & \frac{1}{L_{cse}} & 0 \\ 0 & 0 & 0 & 0 \end{bmatrix}$$

$$\mathbf{A}_{se}^{SF} = \begin{bmatrix} \mathbf{A}_{se}^{3 \times 3} & \mathbf{A}_{se}^{3 \times 1} \\ \mathbf{A}_{se}^{1 \times 3} & -1/CR_C \end{bmatrix}, \quad \mathbf{A}_{se}^{1 \times 3} = \begin{bmatrix} \frac{a_{41}}{C} & \frac{a_{42}}{C} & \frac{a_{43}}{C} \end{bmatrix}$$

$$\mathbf{A}_{se}^{3 \times 3} = \begin{bmatrix} -\frac{R_{ase}}{L_{ase}} & 0 & 0 \\ 0 & -\frac{R_{bse}}{L_{bse}} & 0 \\ 0 & 0 & -\frac{R_{cse}}{L_{cse}} \end{bmatrix}, \quad \mathbf{A}_{se}^{3 \times 1} = \begin{bmatrix} -\frac{a_{14}}{L_{ase}} \\ -\frac{a_{24}}{L_{bse}} \\ -\frac{a_{34}}{L_{cse}} \end{bmatrix}$$

where superscript SF denotes switching functions model vectors and matrices.

Coefficients in \mathbf{A}_{se}^{SF} are given by,

$$a_{14}^6 = \frac{2gs_1 - gs_3 - gs_5}{3}, \quad a_{24}^6 = \frac{2gs_3 - gs_1 - gs_5}{3}$$

$$a_{34}^6 = \frac{2gs_5 - gs_1 - gs_3}{3}$$

$$a_{41}^6 = gs_1, \quad a_{42}^6 = gs_3, \quad a_{43}^6 = gs_5$$

where superscript 6 denotes 6-pulse model coefficients.

As for the 6-pulse SF model, the elements needed to derive higher pulse SF models are the VSC output voltages and the corresponding capacitor current. The multi-pulse VSC configurations shown in **Figure 4** are used to derive the corresponding VSC currents and voltages.

The resulting 12, 24 and 48-pulse SF models are similar to (14) except that coefficients in \mathbf{A}_{se}^{SF} are given in appendix A.

Additionally, the representation in (14) can be expressed in pu system as,

$$\frac{d}{dt} \mathbf{x}_{se\ pu}^{SF} = \mathbf{A}_{se\ pu}^{SF} \mathbf{x}_{se\ pu}^{SF} + \mathbf{B}_{se\ pu}^{SF} \mathbf{u}_{se\ pu}^{SF} \quad (15)$$

$$\mathbf{x}_{se\ pu}^{SF} = \begin{bmatrix} i_{asepu} \\ i_{bsepu} \\ i_{csepu} \\ v_{dc\ pu} \end{bmatrix}, \quad \mathbf{u}_{se\ pu}^{SF} = \begin{bmatrix} v_{srapu} \\ v_{srbpu} \\ v_{srcpu} \\ 0 \end{bmatrix}$$

$$\mathbf{B}_{se\ pu}^{SF} = \begin{bmatrix} \frac{\omega}{X_{Lasepu}} & 0 & 0 & 0 \\ 0 & \frac{\omega}{X_{Lbsepu}} & 0 & 0 \\ 0 & 0 & \frac{\omega}{X_{Lcsepu}} & 0 \\ 0 & 0 & 0 & 0 \end{bmatrix}$$

$$\mathbf{A}_{se\ pu}^{SF} = \begin{bmatrix} \mathbf{A}_{se\ pu}^{3 \times 3} & \mathbf{A}_{se\ pu}^{3 \times 1} \\ \mathbf{A}_{se\ pu}^{1 \times 3} & -\omega X_{Cpu} / R_{Cpu} \end{bmatrix}$$

$$\mathbf{A}_{se\ pu}^{3 \times 3} = \begin{bmatrix} -\frac{\omega R_{asepu}}{X_{Lasepu}} & 0 & 0 \\ 0 & -\frac{\omega R_{bsepu}}{X_{Lbsepu}} & 0 \\ 0 & 0 & -\frac{\omega R_{csepu}}{X_{Lcsepu}} \end{bmatrix}$$

$$\mathbf{A}_{se\ pu}^{3 \times 1} = \begin{bmatrix} -\frac{\omega a_{14}}{X_{Lasepu}} \\ -\frac{\omega a_{24}}{X_{Lbsepu}} \\ -\frac{\omega a_{34}}{X_{Lcsepu}} \end{bmatrix}$$

$$\mathbf{A}_{se\ pu}^{1 \times 3} = \begin{bmatrix} \omega X_{Cpu} a_{41} & \omega X_{Cpu} a_{42} & \omega X_{Cpu} a_{43} \end{bmatrix}$$

$$i_{pu} = i / I_{base}, \quad v_{pu} = v / V_{base}, \quad R_{pu} = R / X_{base}$$

$$X_{Lpu} = \omega L / X_{base}, \quad X_{Cpu} = 1 / \omega C X_{base}$$

where subscript pu denotes variables and parameters in per unit system.

The coefficients of the SF models in pu for 12, 24 and 48-pulse arrangements are given in appendix A.

Now, the STATCOM modeling is addressed based on the similarities with the SSSC. The model is derived using the equivalent circuit of **Figure 6**. The figure shows the STATCOM connected to a voltage node. On the ac side the STATCOM is characterized by a three phase shunt connected sinusoidal voltage source that denotes its voltage injections for phases *a*, *b* and *c* expressed by v_{ash} , v_{bsh} and v_{csh} , respectively. Parameters R_{sh} and L_{sh} represent the influence of the shunt coupling transformer connected to a voltage node denoted by subscript *s*. The dc side of the STATCOM is represented by a current source connected to a capacitor. Shunt connection of a resistance enables representation of converter losses.

By simple examination it can be seen that the SSSC and STATCOM schematic diagrams are very similar. If the receiving end node, v_r , in **Figure 5** is considered to be zero potential (ground), the resulting circuit is the one shown in **Figure 6**. Therefore, the equations that describe the STATCOM phase currents are similar to (10), except that the receiving end node voltages, v_r , are zero. The dc

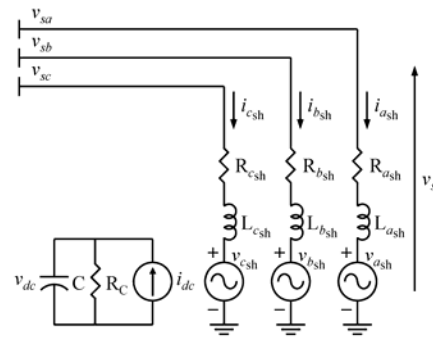


Figure 6. STATCOM equivalent circuit shunt connected to a voltage node

circuit expression that describes the behavior of the dc voltage is (11).

Considering the dc circuit equation (11) and the modified ac one (10), the SF modeling of STATCOM becomes,

$$\frac{d}{dt} \mathbf{x}_{sh}^{SF} = \mathbf{A}_{sh}^{SF} \mathbf{x}_{sh}^{SF} + \mathbf{B}_{sh}^{SF} \mathbf{u}_{sh}^{SF} \quad (16)$$

$$\mathbf{x}_{sh}^{SF} = \mathbf{x}_{se}^{SF}, \quad \mathbf{B}_{sh}^{SF} = \mathbf{B}_{se}^{SF}, \quad \mathbf{A}_{sh}^{SF} = \mathbf{A}_{se}^{SF}, \quad \mathbf{u}_{sh}^{SF} = \begin{bmatrix} v_{sa} \\ v_{sb} \\ v_{sc} \\ 0 \end{bmatrix}$$

The model in (16) is very similar to the one in (14), except for vector \mathbf{u}_{sh}^{SF} ; also the variables and parameters for the SSSC models denoted by subscript se, are substituted for the STATCOM ones denoted by subscript sh.

The coefficients in \mathbf{A}_{sh}^{SF} are the ones in \mathbf{A}_{se}^{SF} for 6, 12, 24 and 48-pulse SF models, and are given in appendix A.

Similar to the SSSC modeling, (16) can be expressed in pu system as,

$$\frac{d}{dt} \mathbf{x}_{sh\ pu}^{SF} = \mathbf{A}_{sh\ pu}^{SF} \mathbf{x}_{sh\ pu}^{SF} + \mathbf{B}_{sh\ pu}^{SF} \mathbf{u}_{sh\ pu}^{SF} \quad (17)$$

$$\mathbf{x}_{sh\ pu}^{SF} = \mathbf{x}_{se\ pu}^{SF}, \quad \mathbf{B}_{sh\ pu}^{SF} = \mathbf{B}_{se\ pu}^{SF}, \quad \mathbf{A}_{sh\ pu}^{SF} = \mathbf{A}_{se\ pu}^{SF}$$

$$\mathbf{u}_{sh\ pu}^{SF} = \begin{bmatrix} v_{sa\ pu} \\ v_{sb\ pu} \\ v_{sc\ pu} \\ 0 \end{bmatrix}$$

The representation in (17) is very similar to the one in (15), except for vector $\mathbf{u}_{sh\ pu}^{SF}$; also the variables and parameters for the SSSC model denoted by subscript se, are substituted for the STATCOM model ones denoted by subscript sh. The pu variables and parameters are given in (15). The coefficients of the SF models in pu for 12, 24 and 48-pulse topologies are given in Appendix A.

3.2 Time Domain Modeling Considering Harmonics

The time domain models that consider harmonic components are obtained directly from the switching functions models, therefore, they are in three phase *abc* coordinates.

The TD models derived are intended to be reduced

order models that enable simulation of multi-pulse SSSC and STATCOM devices, however, although they are reduced models, still represent harmonic components in waveforms of VSC devices.

The SSSC model is derived using the system shown in **Figure 5**. Therefore, the equations that describe the three phase currents and dc circuit voltage of the SSSC are given by (10) and (11).

The TD models are obtained using the state space SF representation given in (14). The derivation of the models is based on the representation of each converter switching functions by its Fourier series. Truncation of the Fourier series is selected to represent suitable harmonic content. Here, a maximum of 50 harmonic components are considered.

In order to derive the TD models, the Fourier series of the switching function of each switch is calculated and then truncated to a suitable number of harmonic components. Substituting these truncated Fourier series representation of switching functions in the SF modeling given in (14), the SSSC TD models that consider harmonic components are achieved.

Rearranging and reducing terms, the TD models finally give,

$$\frac{d}{dt} \mathbf{x}_{se}^{TD} = \mathbf{A}_{se}^{TD} \mathbf{x}_{se}^{TD} + \mathbf{B}_{se}^{TD} \mathbf{u}_{se}^{TD} \quad (18)$$

$$\mathbf{x}_{se}^{TD} = \mathbf{x}_{se}^{SF}, \quad \mathbf{B}_{se}^{TD} = \mathbf{B}_{se}^{SF}, \quad \mathbf{A}_{se}^{TD} = \mathbf{A}_{se}^{SF}, \quad \mathbf{u}_{se}^{TD} = \mathbf{u}_{se}^{SF}$$

where superscript TD denotes time domain modeling vectors and matrices.

It should be noted that the SSSC TD representation in (18) has the same structure as the SF one in (14), which is to be expected since it is derived using the switching functions modeling. Differences arise when taking into account the coefficients in \mathbf{A}_{se}^{TD} . The coefficients for the TD models considering harmonics are given in appendix B, for 12, 24 and 48-pulse VSC configurations.

In the same manner as for the SF models, the representation in (18) can be expressed in pu system as,

$$\frac{d}{dt} \mathbf{x}_{se\ pu}^{TD} = \mathbf{A}_{se\ pu}^{TD} \mathbf{x}_{se\ pu}^{TD} + \mathbf{B}_{se\ pu}^{TD} \mathbf{u}_{se\ pu}^{TD} \quad (19)$$

$$\mathbf{x}_{se\ pu}^{TD} = \mathbf{x}_{se\ pu}^{SF}, \quad \mathbf{B}_{se\ pu}^{TD} = \mathbf{B}_{se\ pu}^{SF}, \quad \mathbf{A}_{se\ pu}^{TD} = \mathbf{A}_{se\ pu}^{SF}$$

$$\mathbf{u}_{se\ pu}^{TD} = \mathbf{u}_{se\ pu}^{SF}$$

$$i_{pu} = i/I_{base}, \quad v_{pu} = v/V_{base}, \quad R_{pu} = R/X_{base}$$

$$X_{L\ pu} = \omega L/X_{base}, \quad X_{C\ pu} = 1/\omega C X_{base}$$

where subscript pu denotes variables and parameters in per unit system.

The coefficients of the TD models in pu for 12, 24 and 48-pulse arrangements are given in Appendix B.

Now, the TD STATCOM modeling is addressed based on the similarities with the SSSC models. The time domain models are derived using the equivalent circuit of **Figure 6**. Therefore, the STATCOM modeling is very similar to (18), except that the receiving end node voltages, v_r , are zero.

Considering the differences between SSSC and STATCOM equivalent circuits, the TD modeling of the STATCOM becomes,

$$\frac{d}{dt} \mathbf{x}_{sh}^{TD} = \mathbf{A}_{sh}^{TD} \mathbf{x}_{sh}^{TD} + \mathbf{B}_{sh}^{TD} \mathbf{u}_{sh}^{TD} \quad (20)$$

$$\mathbf{x}_{sh}^{TD} = \mathbf{x}_{se}^{TD}, \quad \mathbf{B}_{sh}^{TD} = \mathbf{B}_{se}^{TD}, \quad \mathbf{A}_{sh}^{TD} = \mathbf{A}_{se}^{TD}, \quad \mathbf{u}_{sh}^{TD} = \begin{bmatrix} v_{sa} \\ v_{sb} \\ v_{sc} \\ 0 \end{bmatrix}$$

The STATCOM representation in (20) is very similar to the one in (18), except for vector \mathbf{u}_{sh}^{TD} ; also the variables and parameters for the TD SSSC models denoted by subscript se, are substituted for the STATCOM ones denoted by subscript sh.

The coefficients in \mathbf{A}_{sh}^{TD} are the ones in \mathbf{A}_{se}^{TD} for the 12, 24 and 48-pulse TD models, and are given in appendix B.

Similar to the SSSC modeling, (20) can be expressed in pu system as,

$$\frac{d}{dt} \mathbf{x}_{sh\ pu}^{TD} = \mathbf{A}_{sh\ pu}^{TD} \mathbf{x}_{sh\ pu}^{TD} + \mathbf{B}_{sh\ pu}^{TD} \mathbf{u}_{sh\ pu}^{TD} \quad (21)$$

$$\mathbf{x}_{sh\ pu}^{TD} = \mathbf{x}_{se\ pu}^{TD}, \quad \mathbf{B}_{sh\ pu}^{TD} = \mathbf{B}_{se\ pu}^{TD}, \quad \mathbf{A}_{sh\ pu}^{TD} = \mathbf{A}_{se\ pu}^{TD}$$

$$\mathbf{u}_{sh\ pu}^{TD} = \begin{bmatrix} v_{sa\ pu} \\ v_{sb\ pu} \\ v_{sc\ pu} \\ 0 \end{bmatrix}$$

The representation in (21) is very similar to the one in (19), except for vector $\mathbf{u}_{sh\ pu}^{TD}$; also the variables and parameters for the SSSC models denoted by subscript se, are substituted for the STATCOM ones denoted by subscript sh. The pu variables and parameters are given in (19). The coefficients of the TD models in pu for 12, 24 and 48-pulse topologies are given in Appendix B.

4. Simulation Results

In order to assess the effectiveness and precision of the 24 and 48-pulse VSC models, comparison using the SF and TD models, and simulations carried out in Matlab/Simulink® are presented. Comparison is given for the SSSC SF and TD models only. Since SF and TD models represent the behavior of multi-pulse VSC's and the difference between the FACTS devices presented in this paper is in their connection to the power system, generalization about the SF and TD models performance for the STATCOM is possible.

Simulations are carried out using the SSSC circuit shown in **Figure 5** with the following parameters: $R = 10 \Omega$, $L = 700 \text{ mH}$, $C = 2200 \mu\text{F}$ and three phase peak line voltages $v_s = V_m \angle 30^\circ$ and $v_r = V_m \angle 0^\circ$, $V_m = 230\sqrt{2}/\sqrt{3} \text{ kV}$, for a utility system frequency of 60Hz, resistances and inductances of the three phases are equal to R and L , respectively. The simulations presented suppose that the transient response has already passed and the steady state remains. No control is included in the system; in order to maintain the dc voltage magnitude, the appropriate VSC phase angle is used. The simulations consider dc capacitor voltages of approximately 25 kV and 12.5 kV for the 24 and 48-pulse VSC's, respectively, and are carried out in the capacitive operating mode, which is the normal operating mode for a SSSC. All harmonic components are normalized in magnitude and frequency by the 60 Hz fundamental component.

The SSSC 24-pulse arrangement output and capacitor voltages are shown in the upper and lower graphs of **Figure 7**, respectively. It can be noticed that signals obtained using Matlab/Simulink®, as well as the SF and TD models show good agreement between them, and appropriately represent the switching behavior of the converter and its harmonic content. This is corroborated in **Figure 8** where the harmonic components are depicted in the upper and lower graphs, respectively, for the SSSC output and capacitor voltages shown in **Figure 7**. The harmonic components and its magnitudes are comparable between them, which confirms the similarity of the output and capacitor voltage waveforms.

In the upper graph of **Figure 7** harmonic distorted output voltage waveforms are shown that correctly represent the harmonic content present. In the lower graph of **Figure 7** SSSC capacitor voltage waveforms are depicted, where the simulations using Matlab/Simulink®, as well as the SF and TD models are comparable between them, hence, properly representing the switching behavior of the SSSC.

The SSSC 48-pulse arrangement output and capacitor voltages are depicted in the upper and lower graphs of **Figure 9**, respectively. As in the case of the 24-pulse arrangement, the signals obtained using Matlab/Simulink®, as well as the SF and TD models show good agreement

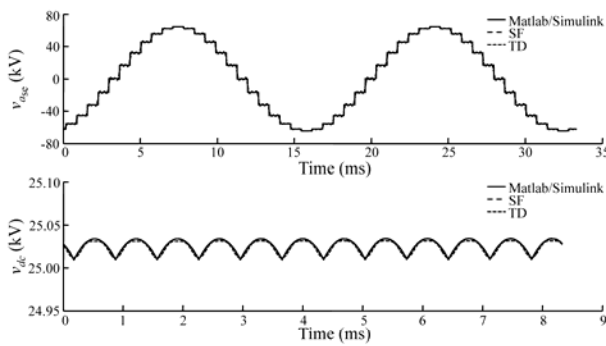


Figure 7. 24-pulse output and dc voltages

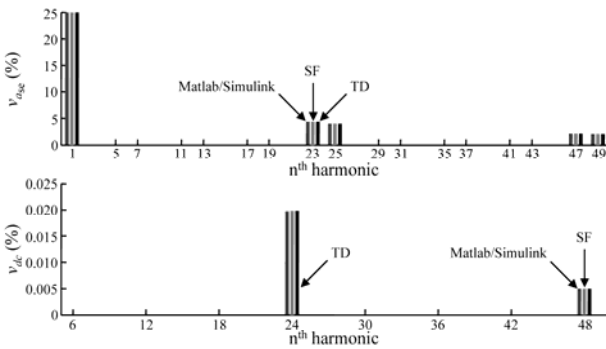


Figure 8. Harmonics of 24-pulse of output and dc voltages

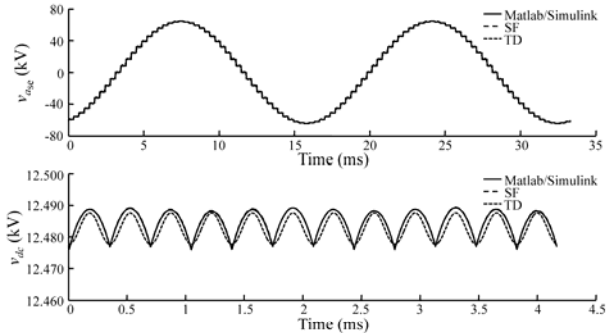


Figure 9. 48-pulse output and dc voltages

between them. **Figure 10** exhibits the harmonic components for the SSSC output and capacitor voltages shown in **Figure 9**, in the upper and lower graphs, respectively, which corroborates the similarities of the voltage waveforms. The harmonic components depicted in **Figure 10** and its magnitudes are comparable between them.

Although signals using Matlab/Simulink® as well as the SF and TD models are very similar, the difference between them arises from variations in the simulations, e.g., in the SF and TD models, the turn-off devices and transformers are assumed to be ideal and lossless, unlike the components in Matlab/Simulink® where a small transformer reactance has to be included; discrepancy in the numerical methods also contributes to disparity be-

tween the signals. Furthermore, since the TD representation is a reduced order model, differences with the detailed simulations are expected; however, the TD models still correctly represent the harmonic components present in VSC signals.

Now, dynamic simulations comparing waveforms using the SF and TD models in pu system are carried out in order to assess the performance of the reduced TD models against the detailed SF ones.

For these dynamic simulations PI control systems are used in order to regulate active power flow over a transmission line.

The simulations are carried out in a system similar to the one illustrated in **Figure 5**, except that the impedance of each phase in composed of two branches in parallel, as depicted in **Figure 11**. The test circuit shows the arrangement for phase *a* where $R_1 = R_2 = 0.0378$ pu, $X_{L1} = X_{L2} = 0.9978$ pu, $v_s = V_{sm} \angle 30^\circ$ pu and $v_r = V_{rm} \angle 0^\circ$ pu, $V_{sm} = V_{rm} = 0.5774 \sqrt{2}$. Phases *b* and *c* are similar to *a*, except for phase shifted voltages. The frequency is 60Hz and the dc capacitor value is $X_C = 0.005$ pu. Simulations are carried out as follows; at the start of the simulation both impedance branches are connected, the dc capacitor voltage is zero and the reference value of the active power which the system has to reach is $P_{ref} = 0.52$ pu. At $t = 0.5$ s one of the branches is disconnected from the system, leaving only R_1 and X_{L1} connected. At $t = 1$ s the missing branch is reconnected, returning the system to its initial configuration. Finally, at $t = 1.5$ s the reference value of the active power changes to $P_{ref} = 0.72$ pu.

The PI control gains are chosen as $k_p = 50$ and $T_i = 1$ because of the fast response produced.

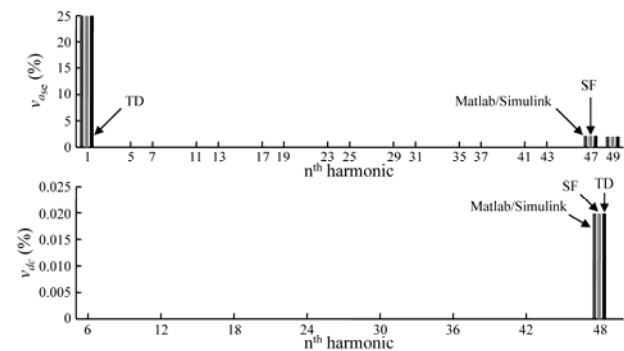


Figure 10. Harmonics of 48-pulse output and dc voltages

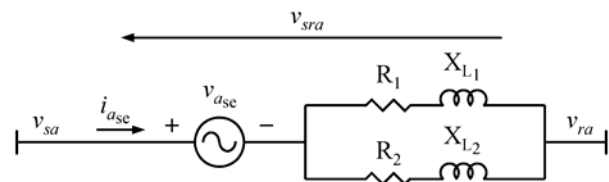


Figure 11. Test circuit of SSSC connected to a transmission line

The output and dc voltages of the 24-pulse converter are exhibited in **Figure 12** for the SF and TD models. It can be seen from the waveforms that both simulations show comparable results. In order to compare these signals in more detail, a close-up is taken on two intervals of each waveform. Again, the waveforms show good agreement between them as illustrated in **Figure 13**.

Current and active power through the line are depicted in **Figure 14**, for the 24-pulse converter. The waveforms of the SF and TD simulations are comparable between them. Close-up intervals are also shown for both signals in **Figure 15** which exhibit good agreement between them.

As for the 24-pulse converter, the output and dc voltages of the 48-pulse device are exhibited in **Figure 16** for the SF and TD models. Again, close-up intervals are shown in **Figure 17** for both signals resulting in comparable results between waveforms.

In addition, current and active power through the transmission line are depicted in **Figure 18**, for the 48-pulse converter SF and TD models. The waveforms of both simulations are comparable between them, which is confirmed in the close-up intervals presented for both signals in **Figure 19**.

The simulations presented show that in steady, as well as in transient state, the SF and TD models show good agreement between them, and can correctly represent the

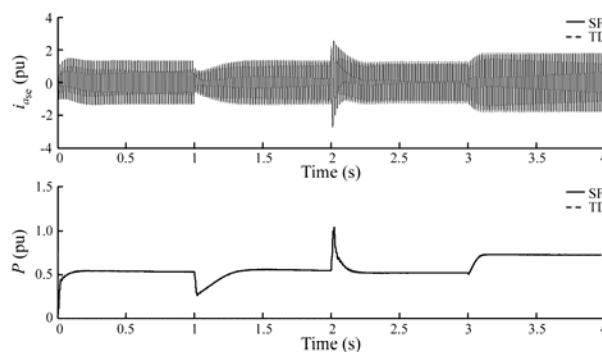


Figure 14. 24-pulse current and active power

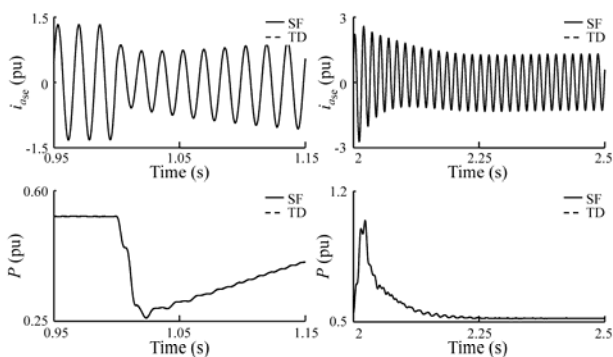


Figure 15. Close-up of 24-pulse current and active power

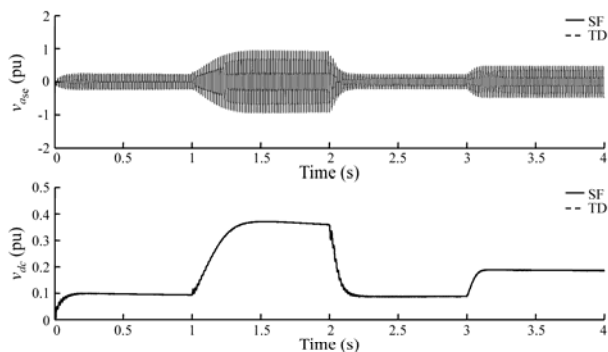


Figure 12. 24-pulse output and dc voltages

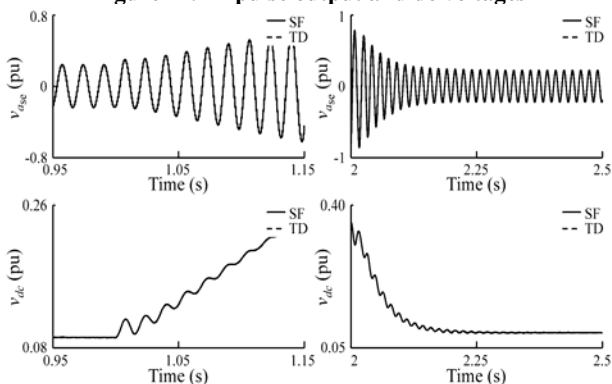


Figure 13. Close-up of 24-pulse output and dc voltages

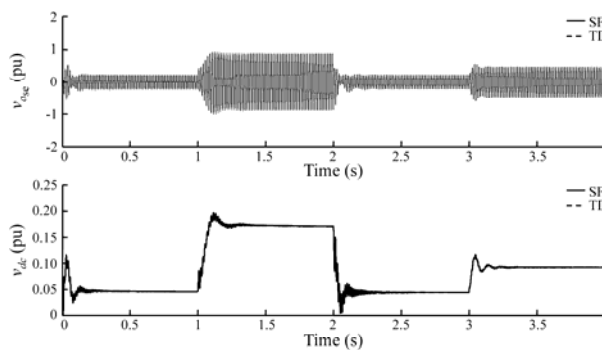


Figure 16. 48-pulse output and dc voltages

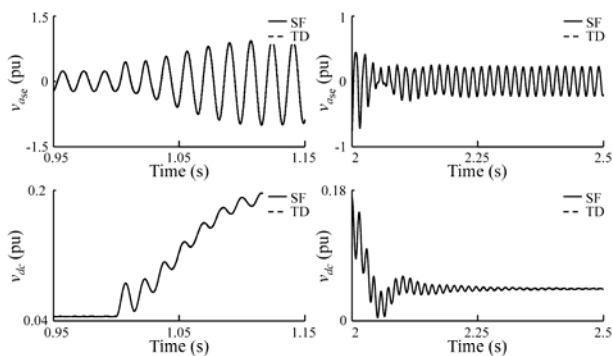


Figure 17. Close-up of 48-pulse output and dc voltages

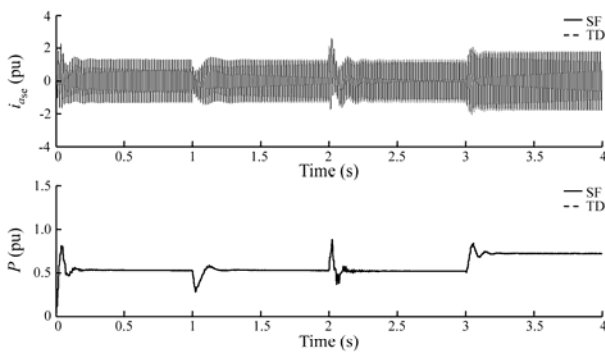


Figure 18. 48-pulse current and active power

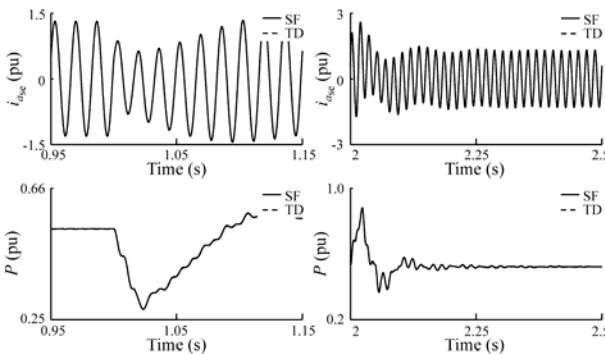


Figure 19. Close-up of 48-pulse current and active power

switching behavior of the multi-pulse converter arrangements.

Also, it is noteworthy to mention that as the number of pulses in the VSC configuration becomes higher, the TD modeling results in an **A** matrix with less elements, as opposed to the SF representation. Therefore, the TD is a much less complex modeling than the SF one in terms of calculation requirements. Since the SF is a detailed more complex representation, while the TD is a less complex one that still correctly represents VSC signals, the decision to use the SF or TD models is in relation to the level of detail and calculation requirements of the desired simulation.

5. Experimental Results

A laboratory implementation of a SSSC device is used for comparison of real and simulated signals in order to assess the SF and TD models performance.

The converter implementation consists of a dc voltage source, a GPP generator, two 6-pulse inverters, and a MCC. The implementation is divided in three stages: GPP generation, voltage inversion and output voltage development. Details of each stage are presented in **Figure 20**.

The GPP generation stage is based on an Atmel AT90S2313 microcontroller running at 10 MHz.

As depicted in **Figure 20(a)** the line current of phase *a* is used as a synchronization signal to coordinate the GPP

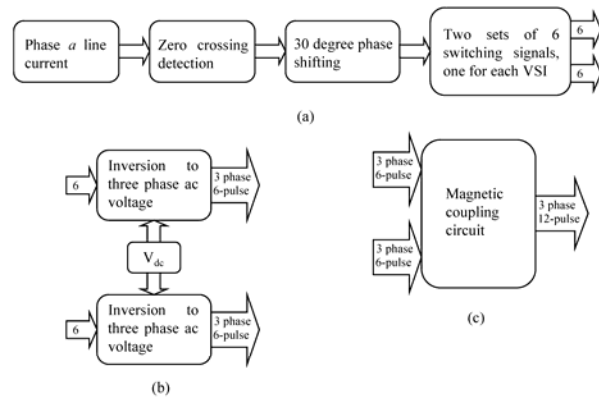


Figure 20. Diagrams of the (a) Gate pulse pattern generation, (b) Voltage inversion and (c) Output voltage development stages

of the commutating devices, and since it is a balanced inverter, phases *b* and *c* have a similar behavior, except that are phase shifted 120° and 240° , respectively. Due to this, the switching signals for phases *b* and *c* are also phase shifted.

The SSSC needs its output voltage synchronized in quadrature with the line current; in order for the synchronization to take place, the line current signal goes through a zero crossing detection sub-stage, which synchronizes the switching signals of the converter *a* branch with the line current of phase *a*. Once these signals are synchronized, the switching pattern can be phase shifted with respect to the synchronizing signal so as to have the desired performance. This synchronization is applied directly to one of the 6-pulse inverters; the other one has to be phase shifted 30° from the first one in order to generate the right 6-pulse voltages needed for the 12-pulse device.

Finally, the stage delivers a GPP with the correct phase shifting consisting of 12 switching signals, accommodated in two sets of six signals apiece, one for each 6-pulse VSC.

From a practical viewpoint the GPP generator stage acquires the current signal of phase *a* from a current sensor. This current signal enters a comparator circuit which sends an indication of the zero crossing events and its slope to a microcontroller. Once the slope and the occurrence of the zero crossings are determined, the microcontroller generates GPP's like the one shown in **Figure 2**, with a delay time proportional to the phase shift angle desired.

The voltage inversion stage consists of the two 6-pulse inverters, each one generating a set of three phase ac voltages with the appropriate phase shift between them.

The three phase inverter bridges are accomplished using Powerex PS21353-GP modules. Each module consists of a three phase IGBT bridge, along with reverse diodes.

As shown in **Figure 20(b)** the two 6-pulse inverters

have two inputs each one. The first input is a GPP, consisting of six switching signals coming from the GPP generation stage; the second one is a dc voltage.

Each inverter employs the appropriate gate signals to achieve three phase 6-pulse ac voltages using the dc voltage source. Both 6-pulse converters share the dc voltage source.

The GPP sets are fed to the 6-pulse inverter modules using optocouplers in order to optically isolate the logic and power circuits. **Figure 21** depicts the prototype test system where two 6-pulse inverters are shown, each one of them has the configuration exhibited in **Figure 1**.

The output voltage construction stage consists of two three phase transformers arranged in the correct configuration. One of the transformers has a delta configuration with a turn ratio of 1:1, the other one has a star arrangement with a turn ratio of $1:1/\sqrt{3}$. The secondary sides of the two transformers are connected in series between them and with the test circuit transmission line. **Figure 21** shows the arrangement of the MCC transformers and their connection with the test system.

As shown in **Figure 20(c)**, the inputs of this stage are the two sets of three phase 6-pulse ac voltages generated by the voltage inversion process which using the MCC are combined to achieve three phase 12-pulse voltages that become the SSSC outputs.

The test circuit of the SSSC prototype is depicted in **Figure 21** and is similar to the one from where the SF and TD models were derived. The circuit is comprised of two voltage sources named sending and receiving end three phase nodes. The angle of the two nodes is phase shifted to enable power transmission. A resistance, R , and an inductance, L , are included in order to represent test circuit line impedance. The three phase sinusoidal voltage source inserted in series with the line represents the SSSC voltage injections.

The test power system parameters are, $R = 0.0165\text{ pu}$, $X_L = 0.1714\text{ pu}$, the three phase ac voltages of the sending and receiving end nodes are respectively, $v_s = V_m \angle 30^\circ$, and $v_r = V_m \angle 0^\circ$, where $V_m = 0.5774\sqrt{2}\text{ pu}$. The system frequency is 60 Hz and the SSSC dc capacitor value is $X_C = 0.0014\text{ pu}$.

The base values considered for power and voltage are, $P_{\text{base}} = 25\text{ W}$ and $V_{\text{base}} = 220\text{ V}$, respectively.

Although the ratings of this laboratory implementation are not comparable in magnitude with those of an actual device, the system provides a basis from which to predict the behavior and performance of a much bigger installation. Furthermore, the verification of the SF and TD models can be directly applicable to higher rating devices.

Actual signals obtained from the laboratory prototype are compared with simulated signals achieved using the SF and TD models. All simulations are carried out using the test power system described with the parameters previously established. The comparison is accomplished in

the capacitive mode of operation, since it is the normal operating mode for a SSSC. The current and voltage signals are all in per unit system.

The systems from which the actual SSSC and simulated signals are obtained suppose that the transient response has already passed and that the steady state remains. For the experiment, the magnitude of the SSSC dc voltage is 0.2045 pu.

The SSSC phase a line current and phase a output voltage are exhibited in **Figure 22**, in the upper and lower graphs, respectively. It can be noticed that the simulations using the SF and TD models, as well as the actual SSSC signals show comparable results. This helps to assess the effectiveness of the SF and TD models, since they adequately represent the switching behavior of the commutating devices in the power converter.

Besides, from the lower graph of **Figure 22**, each commutation in the multi-pulse simulated and actual

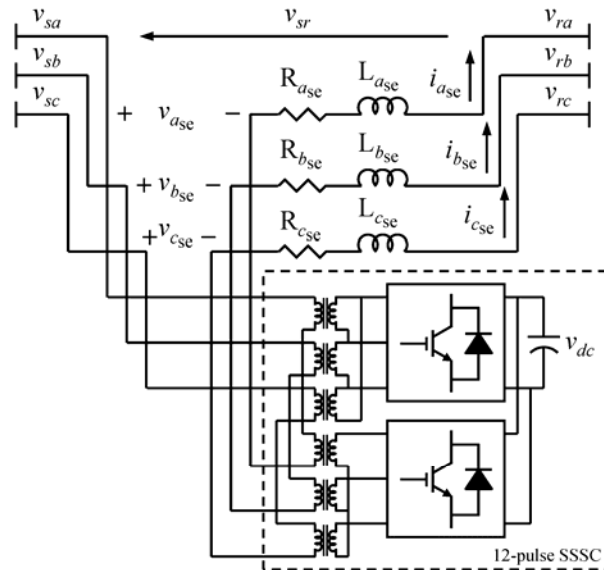


Figure 21. Prototype circuit of SSSC connected to a transmission line

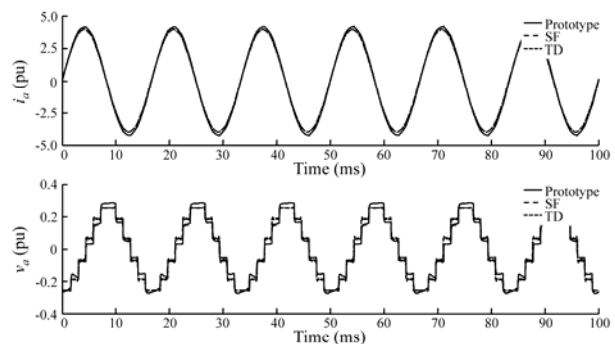


Figure 22. SSSC phase a line current and output voltage

waveforms show good agreement; therefore, switching of devices needed to achieve the output voltage are correctly represented.

The actual and simulated waveforms do not match exactly which can be due to several reasons. First of all, it is reasonable to think that simulated and experimental signals differ. Leaving aside the obvious, which are the assumptions made to derive the models and the differences in parameters, among the possible causes are the following. Since a 12-pulse SSSC configuration is balanced, differences in the values of the elements in each phase cause imbalance. Discrepancies in the magnetic coupling of each phase cause imbalance as well. The imbalance causes the converter not to work properly and, for instance, the MCC could not be achieving the exact construction of the simulated 12-pulse voltage for which it was designed.

Although the SF and TD models verification is made with a laboratory device rated at very small magnitudes compared to actual converter installations, the results obtained with the experiment can be extended to those higher rated systems.

Once the models have been validated, these can be included in simulations containing a diversity of equipment which would be hard to test or use in a laboratory. Also, several tests can be conducted in simulations using the models, which due to laboratory constraints would be very hard to perform in an actual experiment.

The SF modeling offers an accurate method of simulating multi-pulse based VSC devices, such as the SSSC and STATCOM, for studies in which the nature of the analysis demands it. However, although the TD representation is not a detailed model, but a reduced order one, it is accurate enough to correctly represent the harmonic components present in the VSC signals.

The prototype is a 12-pulse VSC due to a higher topology signifies an increase in the device elements, like components or transformers, which represents much higher cost.

Although the models verified are 12-pulse ones, the results can be extended to higher pulse models like the 24 or 48-pulse SF and TD models in order to predict their precision and performance.

6. Conclusions

The paper presents the derivation of multi-pulse VSC based SF and TD models. The models are then compared with Matlab/Simulink® simulations showing good results.

The SF models are intended to represent in detail the behavior of multi-pulse VSC devices, maintaining a compromise between complexity and accuracy. On the other hand, TD models are reduced representations that enable good performance of multi-pulse VSC based FACTS, combined with less calculation requirements than the SF models.

A laboratory prototype was constructed to compare the signals generated with the 12-pulse SF and TD models in order to assess their performance. The comparison of the signals shows adequate results.

Since the effectiveness and precision of the models have been verified and show good results, these can furthermore be included in power system studies where detailed representations of SSSC and STATCOM devices are needed.

REFERENCES

- [1] S. Mori, K. Matsuno, M. Takeda, M. Seto, T. Hasegawa, S. Ohnishi, S. Murakami, and F. Ishiguro, "Development of a large static VAR generator using self-commutated inverters for improving power system stability," *IEEE Transactions on Power Systems*, Vol. 8, No. 1, pp. 371–377, February 1993.
- [2] C. Schauder, M. Gernhardt, E. Stacey, T. Lemak, L. Gyugyi, T. W. Cease, and A. Edris, "Development of a ± 100 MVAR static condenser for voltage control of transmission systems," *IEEE Transactions on Power Delivery*, Vol. 10, No. 3, pp. 1486–1493, July 1995.
- [3] C. Schauder, "The unified power flow controller—A concept becomes reality," *IEE Colloquium: Flexible AC Transmission Systems—The FACTS*, Vol. 1998, No. 500, pp. 7–12, November 1998.
- [4] K. K. Sen, "SSSC – Static synchronous series compensator: Theory, modeling, and applications," *IEEE Transactions on Power Delivery*, Vol. 13, No. 1, pp. 241–246, January 1998.
- [5] L. S. Kumar and A. Ghosh, "Modeling and control design of a static synchronous series compensator," *IEEE Transactions on Power Delivery*, Vol. 14, No. 4, pp. 1448–1453, October 1999.
- [6] D. Soto and T. C. Green, "A comparison of high-power converter topologies for the implementation of FACTS controllers," *IEEE Transactions on Industrial Electronics*, Vol. 49, No. 5, pp. 1072–1080, October 2002.
- [7] A. Nabavi-Niaki and M. R. Iravani, "Steady-state and dynamic models of unified power flow controller (UPFC) for power system studies," *IEEE Transactions on Power Systems*, Vol. 11, pp. 1937–1943, November 1996.
- [8] K. R. Padiyar and A. M. Kulkarni, "Design of reactive current and voltage controller of static condenser," *Electrical Power & Energy Systems*, Vol. 19, No. 6, pp. 397–410, August 1997.
- [9] R. Mihalic and I. Papic, "Static synchronous series compensator—a mean for dynamic power flow control in electric power systems," *Electric Power Systems Research*, Vol. 45, No. 1, pp. 65–72, April 1998.
- [10] A. Sonnenmoser and P. W. Lehn, "Line current balancing with a unified power flow controller," *IEEE Transactions on Power Delivery*, Vol. 14, No. 3, pp. 1151–1157, July 1999.
- [11] I. Papic, "Mathematical analysis of FACTS devices based on a voltage sourced converter Part 1: Mathematical mod-

- els,” *Electric Power Systems Research*, Vol. 56, No. 2, pp. 139–148, November 2000.
- [12] P. García-González and A. G. Cerrada, “Detailed analysis and experimental results of the control system of a UPFC,” *IEE Proceedings of Generation, Transmission and Distribution*, Vol. 150, No. 2, pp. 147–154, March 1996.
- [13] N. G. Hingorani and L. Gyugyi, “Understanding FACTS: Concepts and technology of flexible AC transmission systems,” IEEE Press, 1999.
- [14] M. Mohaddes, A. M. Gole, and Sladjana Elez, “Steady state frequency response of STATCOM,” *IEEE Transactions on Power Delivery*, Vol. 16, No. 11, pp. 18–23, January 2001.
- [15] P. Zúñiga-Haro and J. M. Ramírez, “Multipulse VSC based SSSC,” *Proceedings of 2008 IEEE Power Engineering Society General Meeting*, Pittsburgh, pp. 1–8, 2008.
- [16] P. Zúñiga-Haro and J. M. Ramírez, “Static synchronous series compensator operation based on 48-pulse VSC,” *Proceedings of 2005 IEEE Power Engineering Society 37th Annual North American Power Symposium*, pp. 102–109, 2005.

Appendix A

12, 24 and 48-pulse SF models coefficients
12-pulse SF model coefficients.

$$a_{14}^{12} = \theta + \beta, \quad a_{41}^{12} = gs_{1Y-Y_i} + \beta$$

$$a_{24}^{12} = \delta + \sigma, \quad a_{42}^{12} = gs_{3Y-Y_i} + \sigma$$

$$a_{34}^{12} = \varepsilon + \tau, \quad a_{43}^{12} = gs_{5Y-Y_i} + \tau$$

where $i=1$.

24-pulse SF model coefficients.

$$a_{14}^{24} = \sum_{i=1}^2 (\theta + \beta) + \psi \sum_{\substack{i=1,2 \\ j=2,1}} \eta$$

$$a_{41}^{24} = \sum_{i=1}^2 (gs_{1Y-Y_i} + \beta) + \psi \sum_{\substack{i=1,2 \\ j=2,1}} \eta$$

$$a_{24}^{24} = \sum_{i=1}^2 (\delta + \sigma) + \psi \sum_{\substack{i=1,2 \\ j=2,1}} \rho$$

$$a_{42}^{24} = \sum_{i=1}^2 (gs_{3Y-Y_i} + \sigma) + \psi \sum_{\substack{i=1,2 \\ j=2,1}} \rho$$

$$a_{34}^{24} = \sum_{i=1}^2 (\varepsilon + \tau) + \psi \sum_{\substack{i=1,2 \\ j=2,1}} \gamma$$

$$a_{43}^{24} = \sum_{i=1}^2 (gs_{5Y-Y_i} + \tau) + \psi \sum_{\substack{i=1,2 \\ j=2,1}} \gamma$$

48-pulse SF model coefficients.

$$a_{14}^{48} = \sum_{i=1}^4 (\theta + \beta) + \varphi \sum_{\substack{i=1,4 \\ j=2,1}} \eta + \zeta \sum_{\substack{i=2,3 \\ j=1,2}} \eta$$

$$a_{41}^{48} = \sum_{i=1}^4 (gs_{1Y-Y_i} + \beta) + \varphi \sum_{\substack{i=1,4 \\ j=2,1}} \eta + \zeta \sum_{\substack{i=2,3 \\ j=1,2}} \eta$$

$$a_{24}^{48} = \sum_{i=1}^4 (\delta + \sigma) + \varphi \sum_{\substack{i=1,4 \\ j=2,1}} \rho + \zeta \sum_{\substack{i=2,3 \\ j=1,2}} \rho$$

$$a_{42}^{48} = \sum_{i=1}^4 (gs_{3Y-Y_i} + \sigma) + \varphi \sum_{\substack{i=1,4 \\ j=2,1}} \rho + \zeta \sum_{\substack{i=2,3 \\ j=1,2}} \rho$$

$$a_{34}^{48} = \sum_{i=1}^4 (\varepsilon + \tau) + \varphi \sum_{\substack{i=1,4 \\ j=2,1}} \gamma + \zeta \sum_{\substack{i=2,3 \\ j=1,2}} \gamma$$

$$a_{43}^{48} = \sum_{i=1}^4 (gs_{5Y-Y_i} + \tau) + \varphi \sum_{\substack{i=1,4 \\ j=2,1}} \gamma + \zeta \sum_{\substack{i=2,3 \\ j=1,2}} \gamma$$

The superscripts 12, 24 and 48 denotes 12, 24 and 48-pulse SF models coefficients, respectively; subscripts Y-Y and Δ-Y correspond to the configuration of the coupling transformer of each VSC in the multi-pulse con-

figuration as detailed in [15, 16], and the coefficients elements are given by,

$$\theta = \frac{2gs_{1Y-Y_i} - gs_{3Y-Y_i} - gs_{5Y-Y_i}}{3}$$

$$\beta = \frac{gs_{1\Delta-Y_i} - gs_{3\Delta-Y_i}}{\sqrt{3}}$$

$$\delta = \frac{2gs_{3Y-Y_i} - gs_{1Y-Y_i} - gs_{5Y-Y_i}}{3}$$

$$\sigma = \frac{gs_{3\Delta-Y_i} - gs_{5\Delta-Y_i}}{\sqrt{3}}$$

$$\varepsilon = \frac{2gs_{5Y-Y_i} - gs_{1Y-Y_i} - gs_{3Y-Y_i}}{3}$$

$$\tau = \frac{gs_{5\Delta-Y_i} - gs_{1\Delta-Y_i}}{\sqrt{3}}$$

$$\eta = (-1)^j \left(gs_{3Y-Y_i} - gs_{5Y-Y_i} + \frac{gs_{3\Delta-Y_i} - 2gs_{5\Delta-Y_i} + gs_{1\Delta-Y_i}}{\sqrt{3}} \right)$$

$$\rho = (-1)^j \left(gs_{5Y-Y_i} - gs_{1Y-Y_i} + \frac{gs_{5\Delta-Y_i} - 2gs_{1\Delta-Y_i} + gs_{3\Delta-Y_i}}{\sqrt{3}} \right)$$

$$\gamma = (-1)^j \left(gs_{1Y-Y_i} - gs_{3Y-Y_i} + \frac{gs_{1\Delta-Y_i} - 2gs_{3\Delta-Y_i} + gs_{5\Delta-Y_i}}{\sqrt{3}} \right)$$

$$\psi = \tan(\pi/24)/\sqrt{3}, \quad \varphi = \tan(\pi/16)/\sqrt{3}$$

$$\zeta = \tan(\pi/48)/\sqrt{3}$$

Appendix B

12, 24 and 48-pulse TD models coefficients
12-pulse TD model coefficients.

$$a_{14} = k_0^{14} + \sum_{\substack{n=12m\pm1 \\ m=0,1,2,3,4}} ks_n^{14} \sin(n(\omega t + \alpha)) + kc_n^{14} \cos(n(\omega t + \alpha))$$

$$a_{24} = k_0^{24} + \sum_{\substack{n=12m\pm1 \\ m=0,1,2,3,4}} ks_n^{24} \sin(n(\omega t + \alpha)) + kc_n^{24} \cos(n(\omega t + \alpha))$$

$$a_{34} = k_0^{34} + \sum_{\substack{n=12m\pm1 \\ m=0,1,2,3,4}} k s_n^{34} \sin(n(\omega t + \alpha)) + k c_n^{34} \cos(n(\omega t + \alpha))$$

where,

$$k_0^{14} = 0, \quad k s_1^{14} = \frac{452}{355}, \quad k c_1^{14} = 0, \quad k s_{11}^{14} = \frac{452}{3905}$$

$$k c_{11}^{14} = 0, \quad k s_{13}^{14} = \frac{452}{4615}, \quad k c_{13}^{14} = 0, \quad k s_{23}^{14} = \frac{265}{4787}$$

$$k c_{23}^{14} = 0, \quad k s_{25}^{14} = \frac{452}{8875}, \quad k c_{25}^{14} = 0, \quad k s_{35}^{14} = \frac{497}{13662}$$

$$k c_{35}^{14} = 0, \quad k s_{37}^{14} = \frac{519}{15082}, \quad k c_{37}^{14} = 0, \quad k s_{47}^{14} = \frac{197}{7272}$$

$$k c_{47}^{14} = 0, \quad k s_{49}^{14} = \frac{97}{3733}, \quad k c_{49}^{14} = 0$$

$$k_0^{24} = 0, \quad k s_1^{24} = -\frac{226}{355}, \quad k c_1^{24} = -\frac{1203}{1091}, \quad k s_{11}^{24} = -\frac{226}{3905}$$

$$k c_{11}^{24} = \frac{83}{828}, \quad k s_{13}^{24} = -\frac{226}{4615}, \quad k c_{13}^{24} = -\frac{233}{2747}$$

$$k s_{23}^{24} = -\frac{226}{8165}, \quad k c_{23}^{24} = \frac{92}{1919}, \quad k s_{25}^{24} = -\frac{226}{8875}$$

$$k c_{25}^{24} = -\frac{229}{5192}, \quad k s_{35}^{24} = -\frac{226}{12425}, \quad k c_{35}^{24} = \frac{147}{4666}$$

$$k s_{37}^{24} = -\frac{226}{13135}, \quad k c_{37}^{24} = -\frac{416}{13959}, \quad k s_{47}^{24} = -\frac{226}{16685}$$

$$k c_{47}^{24} = \frac{173}{7374}, \quad k s_{49}^{24} = -\frac{129}{9929}, \quad k c_{49}^{24} = -\frac{105}{4666}$$

$$k_0^{34} = 0, \quad k s_1^{34} = k s_1^{24}, \quad k c_1^{34} = -k c_1^{24}, \quad k s_{11}^{34} = k s_{11}^{24}$$

$$k c_{11}^{34} = -k c_{11}^{24}, \quad k s_{13}^{34} = k s_{13}^{24}, \quad k c_{13}^{34} = -k c_{13}^{24}, \quad k s_{23}^{34} = k s_{23}^{24}$$

$$k c_{23}^{34} = -k c_{23}^{24}, \quad k s_{25}^{34} = k s_{25}^{24}, \quad k c_{25}^{34} = -k c_{25}^{24}, \quad k s_{35}^{34} = k s_{35}^{24}$$

$$k c_{35}^{34} = -k c_{35}^{24}, \quad k s_{37}^{34} = k s_{37}^{24}, \quad k c_{37}^{34} = -k c_{37}^{24}, \quad k s_{47}^{34} = k s_{47}^{24}$$

$$k c_{47}^{34} = -k c_{47}^{24}, \quad k s_{49}^{34} = k s_{49}^{24}, \quad k c_{49}^{34} = -k c_{49}^{24}$$

Coefficients a_{41} , a_{42} and a_{43} have the same structure as a_{14} , a_{24} and a_{34} , respectively, except that constants k_0^{14} , k_0^{24} and k_0^{34} are equal to 1/2.

24-pulse TD model coefficients.

$$a_{14} = k_0^{14} + \sum_{\substack{n=24m\pm1 \\ m=0,1,2}} k s_n^{14} \sin(n(\omega t + \alpha)) + k c_n^{14} \cos(n(\omega t + \alpha))$$

$$a_{24} = k_0^{24} + \sum_{\substack{n=24m\pm1 \\ m=0,1,2}} k s_n^{24} \sin(n(\omega t + \alpha)) + k c_n^{24} \cos(n(\omega t + \alpha))$$

$$a_{34} = k_0^{34} + \sum_{\substack{n=24m\pm1 \\ m=0,1,2}} k s_n^{34} \sin(n(\omega t + \alpha)) + k c_n^{34} \cos(n(\omega t + \alpha))$$

where,

$$k_0^{14} = 0, \quad k s_1^{14} = \frac{863}{336}, \quad k c_1^{14} = 0, \quad k s_{23}^{14} = -\frac{177}{1585}$$

$$k c_{23}^{14} = 0, \quad k s_{25}^{14} = -\frac{439}{4273}, \quad k c_{25}^{14} = 0, \quad k s_{47}^{14} = \frac{97}{1775}$$

$$k c_{47}^{14} = 0, \quad k s_{49}^{14} = \frac{322}{6143}, \quad k c_{49}^{14} = 0$$

$$k_0^{24} = 0, \quad k s_1^{24} = -\frac{863}{672}, \quad k c_1^{24} = -\frac{932}{419}, \quad k s_{23}^{24} = \frac{177}{3170}$$

$$k c_{23}^{24} = -\frac{491}{5077}, \quad k s_{25}^{24} = \frac{212}{4127}, \quad k c_{25}^{24} = \frac{163}{1832}$$

$$k s_{47}^{24} = -\frac{97}{3550}, \quad k c_{47}^{24} = \frac{208}{4395}, \quad k s_{49}^{24} = -\frac{161}{6143}$$

$$k c_{49}^{24} = -\frac{449}{9891}$$

$$k_0^{34} = 0, \quad k s_1^{34} = k s_1^{24}, \quad k c_1^{34} = -k c_1^{24}, \quad k s_{23}^{34} = k s_{23}^{24}$$

$$k c_{23}^{34} = -k c_{23}^{24}, \quad k s_{25}^{34} = k s_{25}^{24}, \quad k c_{25}^{34} = -k c_{25}^{24}, \quad k s_{47}^{34} = k s_{47}^{24}$$

$$k c_{47}^{34} = -k c_{47}^{24}, \quad k s_{49}^{34} = k s_{49}^{24}, \quad k c_{49}^{34} = -k c_{49}^{24}$$

Coefficients a_{41} , a_{42} and a_{43} have the same structure as a_{14} , a_{24} and a_{34} , respectively, except that constants k_0^{14} , k_0^{24} and k_0^{34} are equal to 1.

48-pulse TD model coefficients.

$$a_{14} = k_0^{14} + \sum_{\substack{n=48m\pm1 \\ m=0,1}} k s_n^{14} \sin(n(\omega t + \alpha)) + k c_n^{14} \cos(n(\omega t + \alpha))$$

$$a_{24} = k_0^{24} + \sum_{\substack{n=48m\pm1 \\ m=0,1}} k s_n^{24} \sin(n(\omega t + \alpha)) + k c_n^{24} \cos(n(\omega t + \alpha))$$

$$a_{34} = k_0^{34} + \sum_{\substack{n=48m\pm1 \\ m=0,1}} k s_n^{34} \sin(n(\omega t + \alpha)) + k c_n^{34} \cos(n(\omega t + \alpha))$$

where,

$$k_0^{14} = 0, \quad ks_1^{14} = \frac{3506}{681}, \quad kc_1^{14} = 0, \quad ks_{47}^{14} = -\frac{178}{1625}$$

$$kc_{47}^{14} = 0, \quad ks_{49}^{14} = -\frac{311}{2960}, \quad kc_{49}^{14} = 0$$

$$k_0^{24} = 0, \quad ks_1^{24} = -\frac{1753}{681}, \quad kc_1^{24} = -\frac{807}{181}, \quad ks_{47}^{24} = \frac{89}{1625}$$

$$kc_{47}^{24} = -\frac{253}{2667}, \quad ks_{49}^{24} = \frac{311}{5920}, \quad kc_{49}^{24} = \frac{403}{4429}$$

$$k_0^{34} = 0, \quad ks_1^{34} = ks_1^{24}, \quad kc_1^{34} = -kc_1^{24}, \quad ks_{47}^{34} = ks_{47}^{24}$$

$$kc_{47}^{34} = -kc_{47}^{24}, \quad ks_{49}^{34} = ks_{49}^{24}, \quad kc_{49}^{34} = -kc_{49}^{24}$$

Coefficients a_{41} , a_{42} and a_{43} have the same structure as a_{14} , a_{24} and a_{34} , respectively, except that constants k_0^{14} , k_0^{24} and k_0^{34} are equal to 2.

A Fundamental Equation of Thermodynamics that Embraces Electrical and Magnetic Potentials

Salama Abdel-Hady

Department of Mechanical Engineering, CIC, Cairo, Egypt.
Email: salama_hady@cic-cairo.com

Received November 8th, 2009; revised December 6th, 2009; accepted December 15th, 2009.

ABSTRACT

This paper introduces an energy-analysis of the flow of electrical charges and magnetic flux in addition to the flow of heat into a thermodynamic system. The analysis depends on the results of a held experiment on a magnet that attracted iron balls and a Faraday's discovery as well as similarities between the laws characterizing the flow of electric charges, magnetic flux and heat. As the electric charge and magnetic flux produce entropy changes in some applications as magnetic hysteresis and capacitive deionization, we may express the electric charges and magnetic flux in terms of entropy changes times their corresponding potentials by analogy to expressing heat as a product of temperature and entropy changes. Introducing such postulates into the held energy-analysis; a new fundamental equation of thermodynamics that embraces the flow of electric charges and magnetic flux in terms of the electric and magnetic potentials was derived. The derived equation proved its truth in numerous studies of general energy interactions. Such postulates help also in defining the electric charge and magnetic flux as categories of electromagnetic waves of assigned electric or magnetic potentials and offer plausible explanations of newly discovered phenomena in the fields of electromagnetism and thermodynamics as Kerr effect and magnetic expansion.

Keywords: First and Second Laws of Thermodynamics, Electromagnetic Waves, Heat Flux, Electric Charge, Magnetic Flux

1. Introduction

A simple experiment was run on a control mass that encloses a permanent magnet immersed in a water basin. The magnet was allowed to attract iron-balls moving steadily toward the magnet along an inclined plane. The results of such experiment show a reduction in the temperature of the water. Such decrease in temperature or internal energy of the magnet and the system is considered as a result of a work done by the magnet on the moving balls. So, it is possible to postulate the magnetic flux as a form of energy or electromagnetic waves similar to the heat emitted from a hot body. Reviewing Faraday's discovery when inserting dielectric slabs between the plates of a condenser, the energy stored in the capacitor circuit decreased by the same ratio of increase of the electric charge on the condenser plates [1]. Such result proves also that the electric charge transferred to the dielectrics increases by the same ratio the stored energy of the inserted dielectrics.

According to Maxwell's comments regarding his equations [2], electricity and magnetism were supposed to be of a wave-like nature as the electromagnetic waves since an oscillating electric field generates an oscillating

magnetic field and the oscillating magnetic field in turn generates an oscillating electric field, and so on. In former researches [3,4], it was discussed also common features of the magnetic flux and electric charges. In this article, it is reviewed the similarities between laws characterizing electric charges, magnetic flux and heat flow to prove, analytically, their identity as special categories of electromagnetic waves. The processing of substances in magnetic refrigeration cycles led to a defined description of the produced magnetic-hysteresis in terms of increase of the system's entropy and temperature [5]. Similarly, thermodynamic work required to separate solutions during capacitive deionization processes is fully expressed in terms of decrease of the system's entropy [6]. According to such conclusions; it is possible to postulate the magnetic flux and electric charges in terms of entropy change times a corresponding potential by analogy to heat flux which is expressed in terms of temperature, as a thermal or heat potential, and the corresponding change of entropy. Introducing such postulates into the first law of thermodynamics led to a fundamental equation that embrace electric charge and magnetic flux as mechanisms of energy transfer and that proved its "trueness".

Many references defined the time's arrow as a property of entropy alone [7]. According to such definition, the time coordinate in Maxwell Equations and solutions was fuzzily substituted by entropy. Accordingly; the areas bounded by the oscillating electrical and magnetic potentials in the electromagnetic waves could represent the electrical and magnetic energy imparted by such electromagnetic waves. Such approach helped in postulating the electric charges and magnetic flux as special categories of electromagnetic waves of assigned potentials. Such postulates offer many plausible explanations for phenomena in the fields of thermodynamics and electromagnetism [8] as the magnetic expansion [9], Kerr effect [10] and the phenomena of discharge of clouds, colours of charges and magnetic dipole moments.

2. Experimental Analysis of the Magnetic Flux

As an approach to prove similarity of the heat emitted from a hot body and the magnetic flux emitted from a magnet; a permanent magnet was immersed in an insulated water basin and was allowed to attract polished iron balls of along an inclined smooth glass plane, **Figure 1**. The temperature of water was recorded. As the magnet performed a mechanical work, a decrease in the water temperature was measured by a digital thermometer. By applying the first law of thermodynamics on the magnet-water closed-system [11], we get the following equation:

$$C_F \frac{\Delta t}{\Delta \tau} = n m_b g s \sin \varphi \quad (1)$$

where C_F is the flask's heat capacity, n is the number of attracted balls along the inclined plane per unit time, m_b is the mass of any iron ball, g is the gravity acceleration, s is the length of the path of the iron ball along the inclined smooth plate; φ is angle of inclination of the smooth plate and Δt is the change of temperature during the time interval " $\Delta \tau$ ".

(Experimental data: thermal capacity of the flask = 1.26 kJ/deg, mass of each iron ball = 0.3 kg, number of attracted balls per minute = 42 balls, $s = 20$ and $\varphi = 30$ deg.)

Figure 2 shows the results as calculated from Equation (1) and as recorded during the attraction process. As a conclusion, there is a loss of the magnet's internal energy during attraction of the iron balls. Such energy was substituted by decrease in the temperature or internal energy of the system. Such conclusion proves the behavior of a magnet emitting magnetic flux is similar to a hot body emitting heat or electromagnetic radiation. So, the magnetic flux may be considered as a form of energy or electromagnetic waves.

3. Analysis of Electric Flux

According to the Faraday's discovery [1], when the space

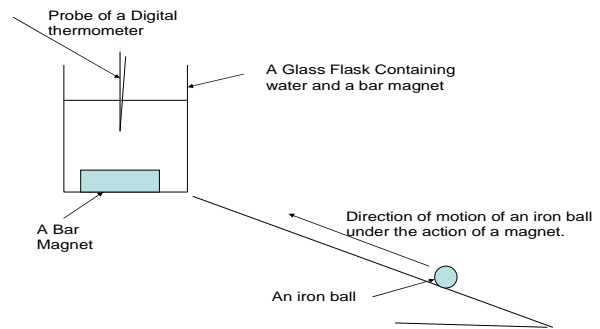


Figure 1. Measurement of magnet's work during attraction of iron balls

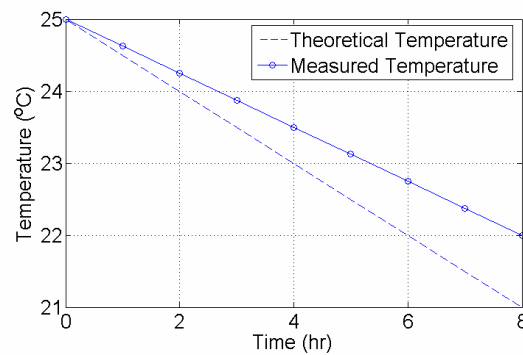


Figure 2. Measurement and calculation results of the system temperature

between the capacitor plates was filled by a dielectric material, the capacitance of the capacitor increased by a dielectric constant κ defined as follows:

$$C = \kappa C_{\text{air}} \quad (2)$$

Faraday found also that the addition of such dielectric material between the plates increased the initial charge on the plates of a capacitor, q_i to a final value q_f defined by the equation [1]:

$$q_f = \kappa q_i \quad (3)$$

By comparing the initial and final energies stored in the capacitor's circuit, U_i and U_f , it was found that the initial energy decreased by the same coefficient κ according to the equation [12]:

$$U_f = \frac{U_i}{\kappa} \quad (4)$$

According to Equations (3) and (4); the coefficient κ equals the ratios of increase of the electric charge on the capacitor plates and the decrease of the internal energy of the capacitor circuit due to insertion of the dielectric material. Such result shows that the loss of the stored energy in the capacitor circuit is absorbed as an electric charge on the capacitor plates. According to the energy – conserva-

tion principles; the electric charge can be considered as a form of energy that is transferred to or from the dielectrics and causes the simultaneous increase of the capacitor charge and decrease of the internal energy of its circuit.

4. Maxwell Waves

Regarding the origin of the electromagnetic wave equations; Maxwell combined displacement current with some of the other equations of electromagnetism and obtained a second-order partial differential equation that describes the propagation of electromagnetic waves through free space or a medium. The homogeneous form of such equation is written in terms of the electric field E and the magnetic field B as follows [12]:

$$(\nabla^2 - \frac{1}{c^2} \frac{\partial^2}{t^2})E = 0 \quad (5)$$

$$(\nabla^2 - \frac{1}{c^2} \frac{\partial^2}{t^2})B = 0 \quad (6)$$

where c is the speed of light in the free space ($c = 299,792,458$ m/second), and t is the time.

The general solution of such electromagnetic wave equation is a linear superposition of waves of the form [13]

$$E(r, t) = g(\varphi(r, t)) = g(\omega t - k \cdot r) \quad (7)$$

$$B(r, t) = g(\varphi(r, t)) = g(\omega t - k \cdot r) \quad (8)$$

Virtually, both forms represent a well-behaved function “ g ” of dimensionless argument “ φ ” where

ω : is the angular frequency (in radians per second), and

k : is the wave vector (in radians per meter).

In addition, for a valid solution, the wave vector and the angular frequency are not independent; they must adhere to the dispersion relation [13]:

$$k = |k| = \frac{\omega}{c} = \frac{2\pi}{\lambda} \quad (9)$$

where: k is the wave number and λ is the wavelength.

Maxwell commented the results of his solutions as follows; the agreement of the results seems to show that light and magnetism are affections of the same substance, and that light is an electromagnetic disturbance propagated through the field according to electromagnetic laws [12]. Such comment considers magnetism of the same substance as electromagnetic waves. Similarly, Maxwell derived a wave form of the electric and magnetic equations, revealing a wave-like nature of electric and magnetic fields. According to Maxwell [13], electricity and magnetism were considered of a wave-like nature as electromagnetic waves, since an oscillating electric field generates an oscillating magnetic field and the magnetic field in turn generates an oscillating electric field, and so

on. Finally; according to Maxwell comments electric charge and magnetic flux may be considered also as forms of electromagnetic waves or energy as they are components of such waves.

5. Similarity of Fluxes

Energy is restricted in this research to the heat radiation propagating as electromagnetic waves or, according to quantum mechanics, as photons. Similarities between such forms of energy as heat, electric charge and magnetic flux are primarily found into their common quantization and conservation properties. The energy is generally quantized into photons of quanta \mathbf{v} , where \mathbf{h} is the Planck's constant [13,] which is conserved according to principles of energy conservation. The electric charge is quantized and conserved too. The elementary charge of a single electron or proton is found experimentally as follows [12]:

$$e = 1.60 \times 10^{-19} \text{ Coulomb,}$$

It is found that any positive or negative charge q show has a quantized value that is expressed as follows [12];

$$q = ne, \text{ where } n = \pm 1, \pm 2, \pm 3, \dots (n \in \mathbb{Z}) \quad (10)$$

The fact that electric charge is quantized may be considered as one of the most profound mysteries of the physical world. However, considering the charge as a form of energy, which are naturally quantized, removes such mystery. Similarly, it is found that the charge is conserved as the net charge in a system or object is preserved too.

The magnetic flux is also quantized into quanta expressed generally as [12]:

$$\Phi_e = n \frac{h}{2e}, \text{ where } n = \pm 1, n = \pm 2, n = \pm 3 \quad (n \in \mathbb{Z}) \quad (11)$$

It is also found that many laws characterizing energy transfer, as heat, are similar to the laws that characterize the transfer of electric charges and the magnetic flux. The heat transfer by conduction is expressed as [14]:

$$\frac{\dot{Q}}{A} = \frac{k}{\Delta x} (T_1 - T_2) = \frac{1}{k / \Delta x} (T_1 - T_2) \quad (12)$$

Similarly, the charge transferred is expressed by Ohm's law as [11]:

$$I = \frac{\dot{Q}_e}{A} = \frac{1}{R} (V_1 - V_2) \quad (13)$$

Equations (12) and (13) show an analogy between the energy transfer by heat and electricity. Heat transfer in the first equation is driven by the difference in temperature and in the second equation the charge transfer is driven by the difference in electrical potentials. However, the laws concerning the transfer of magnetic flux are not

yet formulated, but there is an approach to its formulation as a magnetic flux emergence in the sun is directly traced on the solar surface (in visible-white light) by the presence of dark, mainly round-shaped areas, called sunspots, surrounded by brighter regions of higher magnetic potential called plagues [15]. Measurements of magnetic fields at the solar surface shows that sunspots tend to be grouped in pairs, one with positive and one with negative magnetic polarity which may be characterized by flow of magnetic flux according to similar equations as Equations (12) and (13). Such similarities between heat, electric charge and magnetic flux prove they are forms of energy or electromagnetic waves.

6. A Fundamental Energy Equation

The first and second laws of thermodynamics may lead to a fundamental equation of thermodynamics in the form [14]

$$dU = T dS - p dV + E de + \sigma d\Omega + \sum \mu_i dn_i \quad (14)$$

where:

dU : Change in internal energy of a T.D. system;

$T dS$: Thermal Energy imparted to a system represented as the product of the temperature and the change of entropy;

$p dV$: work of expansion of volume (dV) under the pressure p ;

$\sigma d\Omega$: energy imparted by new surface area formation $d\Omega$ at the surface tension σ ;

$\sum \mu_i dn_i$: work of chemical change dn_i at given chemical potential μ_i .

However, Equation (14) does not include the magnetic energy that may be transferred to any system. In addition, its R.H.S. includes the term “ $E de$ ” that corresponds to the electric energy imparted to the system. This term assumes the parameters “ E ” and “ e ” are properties that define the state of a general thermodynamic system and de is an exact differential or a differential of a property. According to former analysis, the electric charges “ e ” transferred to the system represent energy in transfer of a similar nature as heat and it should not be considered as a property of a thermodynamic system. So, Equation (15) is incorrect according to the principles of thermodynamics.

Introducing the electric charge, magnetic flux and heat flux as mechanisms of energy transfer to a thermodynamic system; a modified form of Equation (14) can be written as follows:

$$dU = \delta Q_{th} + \delta Q_{elect} + \delta \Phi_{mag} - p dV + \sigma d\Omega + \sum \mu_i dn_i \quad (15)$$

The processing of substances in magnetic refrigeration cycles leads to a defined description of the produced magnetic hysteresis in terms of an entropy increase and the system temperature [4]. So, temperature and entropy changes were actually achievable by the flow of magnetic flux into a system. In this context, the fact that the working material displays hysteresis [16], calls for a better physical understanding of the role of irreversibility in the magnetization process. Such understanding can be based on describing the magnetic flux by similar terms as heat flux, *i.e.* in terms of magnetic potential times a corresponding entropy increase. Such representation removes the ambiguity found in Bill queries [9]. Similarly; revising the work of Biesheuvel in the thermodynamic cycle analysis of capacitive deionization, [6], where the thermodynamic work required in solutions separation during capacitive deionization processes was fully utilized to decrease the entropy of the system. Such analysis implements also the expression of the electric charge in terms of the product of electric potential times the corresponding entropy increase.

According to the second law of T.D., the flow of heat into a system generates an entropy increase of such system expressed by the relation [10]:

$$Q_{thermal} = \int T dS_{thermal} \quad (16)$$

According to the previous analysis and the derived similarities, the electric charge can be expressed by a similar expression as follows.

$$Q_{elect} = \int E dS_{electric} \quad (17)$$

where Q_{elect} is electric charge imparted to a system, E is the electrical field intensity or potential, in analogy to temperature as the thermal potential, and $dS_{electric}$ is the entropy increase associated by such transferred electric energy or charge.

According to modern literatures [12], the term “ B ” represents the magnetic flux density. However, such density can be assumed proportional to the magnetic field intensity, H , according to the following relation (in free space) [12]:

$$B = \mu_0 H \quad (18)$$

where $\mu_0 (= 4\pi \times 10^{-7})$ is called permeability of free space or magnetic space constant. Such direct proportionality allows introducing the magnetic field intensity to replace the magnetic flux density in Maxwell’s solution which is analogous to the electric field intensity.

So, the magnetic flux can be expressed as follows:

$$\Phi_{mag} = \int H dS_{magnetic} \quad (19)$$

where Φ_{mag} is the magnetic flux imparted to a system, H is the magnetic field intensity and $dS_{magnetic}$ is the

generated entropy by the transferred magnetic flux. By substituting Equations (16), (17) and (19) into Equation (14); a modified fundamental equation of thermodynamics can be expressed as follows:

$$dU = T (dS)_{th} + E (dS)_{el} + H (dS)_{mag} - p dV + \sigma d\Omega + \sum \mu_i dn_i \quad (20)$$

where $T (dS)_{th}$, $E (dS)_{el}$ and $H (dS)_{mag}$ correspond to the thermal, electric and magnetic energies imparted to the system, respectively, and $(dS)_{th}$, $(dS)_{el}$ and $(dS)_{mag}$ represent the entropy productions by the corresponding transferred thermal, electric and magnetic energies. The main corollary of such fundamental equations is the possibility of representing the electric charges transferred or imparted to a system into an E-s diagram and the magnetic flux imparted to a system into an H-s diagram similar to the T-s diagram that represent the heat transferred to such system.

7. Maxwell Equations

The arrow of time is found as property of entropy alone [7]. Accordingly; time in Maxwell Equations (5) and (6) may be replaced by entropy. Such transformation leads to modified solutions of Maxwell equations that may be stated as follows:

$$E(r,t) = s(\varphi(r,s)) \quad (21)$$

$$H(r,t) = s(\varphi(r,s)) \quad (22)$$

Accordingly, the electromagnetic waves can be represented in E-s and B-s planes by replacing the time axis in **Figure 3** by entropy. In such representation; the areas enclosed by the oscillating fields, electric or magnetic, represents the imparted electric and magnetic energies as postulated in Equations (17) and (19).

Searching for a plausible answer of a frequently asked question: If the electromagnetic waves are considered, according to the quantum mechanics, as photons; then, how the photon can have a charge or a magnetic polarity [14]? The answer implements a modified solution of Maxwell Equations which is not identical to that stated by Equations (7) and (8). In the following solution it is assumed a non-zero initial electrical potential " ΔE_i " in the electric component of the electromagnetic wave. Hence, the following solution may satisfy the postulated Maxwell's Equations (21) and (22), where the time is replaced by entropy:

$$E(r,t) = s(\varphi(r,s)) + / - \Delta \bar{E} \quad (23)$$

$$H(r,t) = s(\varphi(r,s)) \quad (24)$$

Such solution assumes some categories of electromagnetic waves whose electric potential is oscillating

around a specified value of non-zero electric potential but its magnetic potential is oscillating about a zero magnetic potential. The graphical representation of such solution is seen in **Figures 4** and **5**, where **Figure 4** represents a positive charge and **Figure 5** represents a negative charge.

The net charge in each imparted sinusoidal wave has a value which may be positive or negative according to the sign of the charge found by the following integral in a complete wave:

$$Q_{elect} = \int_0^{2\pi} \bar{E} dS_{elect} \quad (25)$$

The given integration may represent an electric charge of a positive or negative potentiality according to the direction of the wave oscillations if it is around positive or negative values of $\Delta \bar{E}$.

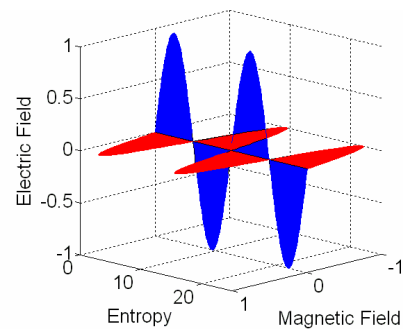


Figure 3. Electromagnetic waves in E-s and H-s planes

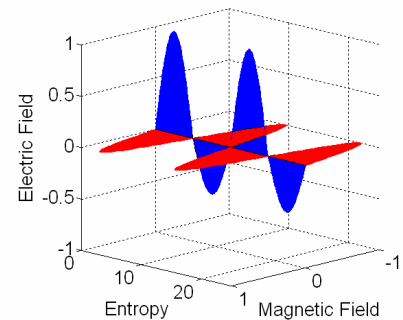


Figure 4. Graphical representation of a positive electric charge

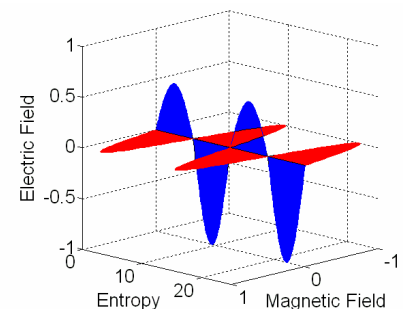


Figure 5. Graphical representation of a negative electric charge

Similarly, it is assumed in the following solution a non-zero initial magnetic potential “ $\Delta \bar{H}$ ” in the magnetic component of the electromagnetic wave. So, the following modified Maxwell’s solution may represent flow of magnetic flux:

$$H(r,t)=s(\varphi(r,t))+/-\Delta \bar{H} \quad (26)$$

$$E(r,t)=s(\varphi(r,t)) \quad (27)$$

Such solution is represented graphically in **Figure 6** where the net bounded area has a non-zero magnetic potential. So, the net magnetic flux in each imparted sinusoidal wave has the value:

$$\Phi = \int_0^{2\pi} \bar{H} dS_{mag} \quad (28)$$

So, the postulated solutions of Maxwell Equations and the introduced definitions of electric charges and heat flux assign definite potentials for such fluxes in terms of ($\Delta \bar{E}$) and ($\Delta \bar{H}$), with definite polarity or direction. The units of the electric charge or the magnetic flux are stated as forms of energy in Joules. Hence the units of dS_{elect} and dS_{mag} will be in Joule/Volt and Joule/Oersted respectively in analogy to the units of $dS_{thermal}$ in Joule / K [6]. Such definitions remove confusions in the units of magnetism and electricity.

8. Reviewing the Introduced Fundamental Equation

As previously mentioned, the definitions of the electric charge and magnetic flux, as modified forms of EM waves, can be directly concluded from Maxwell’s statements and the similarity of the laws governing such entities. However, such definitions introduce also plausible explanations to many discovered phenomena. The definition of the electric charge as electromagnetic waves explains the behavior of the cathode rays as waves in the famous Crookes tube [15], where the cathode rays, defined previously as flow of electric charges or electrons,

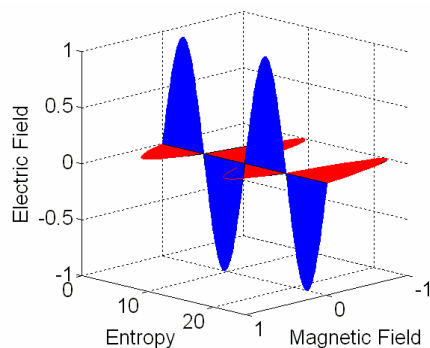


Figure 6. Graphical representation of magnetic flux

travelled in straight lines, produce a shadow when obstructed by objects and the rays could pass through thin metal foils without disturbing them (Tested by New Zealander Ernest Rutherford using gold foil [15]). Hertz maintained it also was a wave. Hence, the introduced definition of electric charge as a flow of modified EM waves offer more plausible explanations of the found characteristics of the Cathode rays as a form of electromagnetic waves.

Similarly, the introduced definitions of the electric charges and the magnetic flux as special categories of electromagnetic waves find plausible explanations to the “Kerr Effect” [9]. Such phenomena detect effects of electric and magnetic fields on the flow of electromagnetic waves. In case of electric fields, a quadratic electro-optic effect (QEO effect) is detected. In case of magnetic fields, a magneto-optic Kerr effect (MOK effect) is detected. The QEO effect is identified by a change in the refractive index of all materials when they are crossed by electromagnetic waves in the presence of an applied AC or DC electric fields. Similarly; MOKE effect may be recognized, in some cases, by rotation of the plane of polarization of the transmitted light under the influence of magnetic field [9]. According to the introduced definitions, the light gains by the applied electric or magnetic fields the potentials differences ($\Delta \bar{E}$) or ($\Delta \bar{H}$), that converts the light waves into electric charges or magnetic flux of different index of refraction or rotated plane of polarization.

Replacing the time axis by an entropy axis in the Maxwell’s solutions and considering the propagating EM waves as propagations of electric and magnetic energies of limited entropy production and energy quanta proves the description of photons as tiny bundle of electric and magnetic fields [18].

Introducing entropy, as a probability measure of disorder [18], to replace the time in Maxwell equations lead to a probabilistic Maxwell’s solution that is analogous to probabilistic wave solution $\Psi(x, t)$ of the Schrodinger’s equation. The introduced fundamental equation can be valuable in studies that apply Poisson-Nernst-Planck theory to investigate ion permeation and related transport processes [19].

Assigning a value of a definite electric potential for the charge, according to the stated definitions of electric charges, is similar to the assigned thermal potential, temperature, for the heat. Such electrical potential explains the phenomena of colored charges where each charge may have a different potential [8] and explain the phenomena of charging of clouds [12].

9. Conclusions

Reviewing experimentally and analytically the similarity and analogy between heat, electric charges and magnetic

flux, the electric charge and magnetic flux were proved as special categories of energy or modified forms electromagnetic waves that have electrical or magnetic potentials. Previous analysis served also in expressing the magnetic flux and electric charges in terms of entropy change times a corresponding potential by analogy to heat flux. Introducing such postulates into the first law of thermodynamics led to a modified fundamental equation that embrace electric charge and magnetic flux as mechanisms of energy transfer. Considering time's arrow as a property of entropy alone [7], the time in the Maxwell equation is replaced by entropy such that the areas bounded by the oscillating electrical and magnetic potentials represent the electrical and magnetic energies imparted by the electromagnetic wave. Such representation helps in expressing the qualities or potentials for the electric charge and the magnetic flux in analogy to the heat quality (temperature). The offered postulates lead to modified definitions of electric charge and magnetic flux in addition to plausible explanations of newly discovered phenomena in the fields of electromagnetism and thermodynamics as Kerr effect and magnetic expansion.

REFERENCES

- [1] D. T. Ryan, "Toward a cognitive-historical understanding of Michael Faraday's research: Editor's introduction," *Perspectives on Science*, Vol. 14, No. 1, 2006.
- [2] J. D. Jackson, "Classical electrodynamics," 3rd Ed., Wiley, New York, 1998.
- [3] S. Abdelhady, "Thermodynamic analysis of electric charges and magnetic flux," Cairo 11th International Conference on Energy and Environment, Ghurgada, pp. 175–185, March 2009.
- [4] S. Abdelhady, "A fuzzy approach to the physics of electromagnetic waves and atomic particles," Cairo 10th International Conference on Energy and Environment, Luxor, pp. 234–241, March 2007.
- [5] V. Basso, *et al.*, "Effect of material hysteresis in magnetic refrigeration cycles," *International Journal of Refrigeration*, Vol. 29, No. 8, pp. 1358–1365, December 2006.
- [6] P. M. Biesheuvel, "Thermodynamic cycle analysis for capacitive deionization," *Journal of Colloid and Interface Science*, Vol. 332, No. 1, pp. 258–264, April 2009.
- [7] J. J. Halliwell, J. Pérez-Mercader, and W. H. Zurek, "Physical origins of time asymmetry," Cambridge University Press, London, 1994.
- [8] A. E. Shabad and V. V. Usov, "Electric field of a point-like charge in a strong magnetic field and ground state of a hydrogenlike atom," *Physical Review D*, Vol. 77, No. 2, 2008.
- [9] F. X. Hu, *et al.*, "Magnetoresistances and magnetic entropy changes associated with negative lattice expansions in NaZn₁₃-type compounds LaFeCoSi," *Chinese Physics*, Vol. 14, No. 11, pp. 2329–2334, 2005.
- [10] T. J. Englert, B. H. Chowdhury, and E. A. Grigsby, "Laboratory investigation of the electro-optic Kerr effect for the detection of transmission line faults," *IEEE Transactions on Power Delivery*, Vol. 6, No. 3, pp. 979–988, 1991.
- [11] A. C. Yunus and A. B. Michael, "Thermodynamics: An engineering approach," McGraw-Hill Science Engineering, 2006.
- [12] D. Haaiday, R. Resnick, and J. Walker, "Fundamentals of physics," 7th Ed., John Wiley & Sons, New York, 2004.
- [13] C. F. Stevens, "The six core theories of modern physics," MIT Press, London, 1965.
- [14] H. B. Callen, "Thermodynamics and an introduction to themostatistics," John Wiley & Sons, New York, 1985.
- [15] P. K. Shukla, *et al.*, "Equivalent electric charge of photons in an electron – positron plasma," *Physica Scripta*, Vol. 62, No. 2–3, 2000.
- [16] M. N. O. Sadiku, "Elements of electromagnetics," Oxford University Press, Oxford, 2006.
- [17] B. Benny, "How do you reconcile EM fields with frequency of light?" April 2009. <http://www.physicsforums.com/showthread.php?p=2161363>
- [18] D. J. Griffiths, "Introduction to quantum mechanics," Benjamin Cummings Publishing Company, San Francisco, 2004.
- [19] S. A. Zhou and M. Uesaka, "Modeling of transport phenomena of ions and polarizable molecules: A generalized Poisson–Nernst–Planck theory," *International Journal of Engineering Science*, Vol. 44, No. 13–14, pp. 938–948, 2006.

Energy and Momentum Considerations in an Ideal Solenoid

Sami Mohammad AL-Jaber^{1,2}

¹Department of Physics, An-Najah National University, Nablus, Palestine; ²Palestine Technical University (PTU), Kadoorie, Palestine.

Email: Jaber@najah.edu

Received November 4th, 2009; revised December 8th, 2009; accepted December 15th, 2009.

ABSTRACT

The electromagnetic linear momentum and the energy balance in an infinite solenoid with a time-dependant current are examined. We show that the electromagnetic linear momentum density and its associated force density are balanced by the hidden momentum density and its associated hidden force density respectively. We also show that exactly half the energy delivered by the power supply appears as stored magnetic energy inside the solenoid. The other half is lost against the induced electromotive force that appears in the windings of the solenoid during the time through which the current is building up towards its final value. This energy loss, which is found in other analogue situations, is necessary to transfer the system from an initial non-equilibrium state to a final equilibrium one.

Keywords: Electromagnetic Linear Momentum, Energy Balance, Hidden Momentum

1. Introduction

The electromagnetic Poynting vector has long been of considerable interest over the years [1–9]. This is so because it is directly related to the electromagnetic (EM) energy flux and the electromagnetic linear momentum. In recent years, the role of EM linear momentum in total momentum balance has attracted the attention of many authors [10–16]. Furthermore, the EM energy flux carried by the Poynting vector has been the subject of many workers in the context of energy conservation in electromagnetic systems [17–21]. In recent years, it was shown that when a charged capacitor is connected to another uncharged identical one, exactly half the stored energy disappears after the equilibrium state is achieved. This also happens when a capacitor is charged by a battery, where only half the supplied energy is stored in the capacitor. This pedagogical problem has been a topic of interest by several authors [22–27]. When dealing with energy conservation in EM systems, one has to consider all the possible channels through which energy is transported through as the system transforms from an initial non-equilibrium to a final equilibrium state. For example, it was shown [23] that when charging a capacitor half the work done by the power source is stored in the capacitor while the other half is carried by the Poynting vector which crosses the surface of the connecting wires. The purpose of this paper is to shed some light on the dy-

namics of the electromagnetic momentum and the energy needed when an electromagnetic system transforms from non-equilibrium to equilibrium states. This gives a fruitful and an illustrative example to students in electrodynamics course and helps them for a deep understanding of basic concepts in the subject. To that end, we consider an infinitely long solenoid which is fed by a current that varies linearly in time for a time period T after which it reaches its final constant value. The paper is organized as follows: In Section 2, we consider the electromagnetic momentum. In Section 3, we examine electromagnetic energy. Section 4 is devoted for conclusions.

2. Electromagnetic Momentum for an Ideal Solenoid

We consider an infinitely long solenoid (ideal) of radius R and with number of turns per unit length n . The purpose is to examine the dynamics of the linear momentum balance during a time period, say T , through which the current is linearly increasing towards its final constant value, say I_0 . Our system is assumed to be force-free which means that the total linear momentum (mechanical momentum and electromagnetic momentum) is constant, which could be taken to be zero. Therefore, we assume that the battery connected to the solenoid gives a time-dependent current $I(t)$ given by:

$$I(t) = \begin{cases} \frac{I_0}{T} t & 0 \leq t \leq T \\ I_0 & t \geq T \end{cases} \quad (1)$$

Faraday's law of induction suggests an induced electric field whose value satisfies its integral form

$$\oint \vec{E} \cdot d\vec{l} = -\frac{d\phi}{dt} \quad (2)$$

where \vec{E} is the induced electric field and ϕ is the magnetic flux inside the solenoid.

Choosing a circular loop of radius r inside the solenoid, and using $\vec{B} = \mu_0 n I(t) \hat{z}$, for the magnetic field inside the solenoid, one gets

$$E(2\pi r) = -\frac{d}{dt}(\pi r^2 B(t)) = -\pi r^2 \mu_0 n \frac{d}{dt} I(t) \quad (3)$$

and thus

$$\vec{E}(r) = \begin{cases} -\frac{\mu_0 n I_0}{2T} r \hat{\phi} & 0 \leq t \leq T \\ 0 & t > T \end{cases} \quad (4)$$

The Poynting vector inside the solenoid, during the time T , is given by

$$\vec{S} = \frac{1}{\mu_0} \vec{E} \times \vec{B} = -\frac{\mu_0 I_0^2 n^2}{2T^2} t r \hat{r} \quad (5)$$

and therefore the electromagnetic linear momentum density is

$$\vec{p}_{EM} = \epsilon_0 \mu_0 \vec{S} = -\frac{\epsilon_0}{2} \left(\frac{\mu_0 I_0 n}{T} \right)^2 t r \hat{r} \quad (6)$$

The total electromagnetic linear momentum, \vec{p}_{total} , can be computed as follows: writing $\hat{r} = \cos\varphi \hat{i} + \sin\varphi \hat{j}$, we get

$$\vec{p}_{total} = -\frac{\epsilon_0}{2} \left(\frac{\mu_0 I_0 n}{T} \right)^2 t \int_0^R r^2 dr \int_0^\ell dz \int_0^{2\pi} (\cos\varphi \hat{i} + \sin\varphi \hat{j}) d\varphi = 0 \quad (7)$$

since the φ integral vanishes. Equation (6) gives a force density

$$\vec{f} = \frac{d\vec{p}_{EM}}{dt} = -\frac{\epsilon_0}{2} \left(\frac{\mu_0 I_0 n}{T} \right)^2 r \hat{r} \quad (8)$$

which gives a vanishing total force once the integration over φ is carried out. This force density is needed to bend the current in its circular loops that, due to inductive inertia, otherwise would move in a straight line. As we will see in a moment, the reaction force density (hidden force density as we will see shortly) to the above

force density causes the radius of the circular loop to increase. So our result shows that during the period T , through which the current is increasing, the total electromagnetic momentum and the total force are both zeros but yet they have non-vanishing density values that are directed towards the axis of the solenoid. This result needs explanation since initially (for $t < 0$) the system has no momentum density. We show below that the electromagnetic linear momentum density is exactly balanced by hidden momentum density that arises during the time period T . Assuming the solenoid has a radius R with its axis aligned along the z -axis and the current flows counterclockwise ($+\hat{\phi}$ direction), then following Babson *et al.* [28], the hidden momentum (which is of relativistic origin) is given by

$$\vec{p}_{hidden} = \frac{1}{c^2} (\vec{m} \times \vec{E}) \quad (9)$$

where \vec{m} is the magnetic dipole moment of the current loop(s) and \vec{E} is the electric field. Now, for a length ℓ of the solenoid, the number of turns is $n\ell$ and thus the magnetic dipole moment $\vec{m} = n\ell \pi R^2 (I_0 t / T) \hat{z}$. Using Equation (4) for the induced electric field, with $r = R$, we get

$$\vec{p}_{hidden} = +\frac{\epsilon_0}{2} \left(\frac{\mu_0 I_0 n}{T} \right)^2 t \pi R^3 \ell \hat{r}, \quad (10)$$

where we used $1/c^2 = \epsilon_0 \mu_0$. Therefore, the hidden momentum density is

$$\vec{p}_{hidden}^{dens} = +\frac{\epsilon_0}{2} \left(\frac{\mu_0 I_0 n}{T} \right)^2 t R \hat{r} \quad (11)$$

which exactly cancels the electromagnetic linear momentum density at the loops of the solenoid, as can be seen from Equation (6) with $r = R$. Back to the force density given in Equation (8), this force density is related to the pressure gradient. As it was shown in [28], the relativistic relation between the force density and the pressure gradient is

$$\vec{f} = \gamma^2 \nabla P \quad (12)$$

where γ^2 is the usual Lorentz factor. It is interesting to note that the time derivative of the hidden momentum density (given in Equation (11)) gives the so-called the hidden force density which is exactly the negative of the force density evaluated at the surface of the solenoid, $r = R$ (see Equation (8)). Therefore, at any time t during the time period T , the electromagnetic force density is exactly canceled by the hidden force density.

2. Energy Considerations

The purpose of this section is to examine energy balance which is involved in the process of establishing a current

in an infinite solenoid. It is well-known that the stored magnetic energy in a length ℓ of an infinite solenoid that carries a current I is

$$U(t) = \frac{1}{2} L I^2 = \frac{1}{2} \mu_0 \pi \left(\frac{n R I_0}{T} t \right)^2 \ell \quad (13)$$

where we used Equation (1) and the self-inductance $L = \mu_0 \pi R^2 n^2 \ell$, for a length ℓ of the solenoid. When the current reaches its final value I_0 , at $t = T$, the stored magnetic energy becomes

$$U = \frac{1}{2} \mu_0 \pi (n R I_0)^2 \ell \quad (14)$$

The question to be answered is how much work is needed to be done by the power supply in order to store the magnetic energy given in Equation (14). During the time – period T , the electromagnetic power per unit area that crosses the surface of the solenoid is given by the Poynting vector \vec{S} evaluated at the solenoid's surface. Thus using Equation (5) with $r = R$, we get

$$\vec{S} = -\frac{\mu_0}{2} \left(\frac{n I_0}{T} \right)^2 R t \hat{r} \quad (15)$$

The electromagnetic energy E_{EM} that is transmitted inside a length ℓ of the solenoid is

$$\begin{aligned} E_{EM} &= \oint \vec{S} \cdot d\vec{a} \, dt \\ &= -\frac{\mu_0}{2} \left(\frac{n I_0}{T} \right)^2 R \int_0^{2\pi} \int_0^\ell \hat{r} \cdot R d\varphi dz \hat{r} \int_0^T t \, dt \\ &= -\frac{1}{2} \pi \mu_0 (R n I_0)^2 \ell \end{aligned} \quad (16)$$

which has the same magnitude as the stored magnetic energy given in Equation (14). Therefore, the energy that was carried by the Poynting vector has been stored as magnetic energy inside the solenoid. To see other forms of energy involved in the process of establishing the current in the solenoid, the time-dependence of the magnetic field gives an induced electromotive force (ε). This induced electromotive force is given by Faraday's law, namely

$$\begin{aligned} \varepsilon &= -N \frac{d\phi}{dt} = -n \ell \pi R^2 \frac{d}{dt} \left(\frac{\mu_0 n I_0 t}{T} \right) = \\ &= -\pi R^2 \mu_0 n^2 \ell \frac{I_0}{T} \end{aligned} \quad (17)$$

The power done by this induced electromotive force is thus

$$\varepsilon I = -\pi R^2 \mu_0 n^2 \ell \left(\frac{I_0}{T} \right)^2 t \quad (18)$$

and therefore, the work done is

$$\begin{aligned} \int_0^T \varepsilon I \, dt &= \int_0^T -\pi R^2 \mu_0 n^2 \ell \left(\frac{I_0}{T} \right)^2 t \, dt \\ &= -\frac{1}{2} \mu_0 \pi (n R I_0)^2 \ell \end{aligned} \quad (19)$$

The above Equation clearly shows that the work done by the power supply against the induced electromotive force (which is the negative of Equation (19)) is exactly equal to the stored magnetic energy given by Equation (14). Therefore, the total energy delivered by the power supply is twice the stored magnetic energy. It should be emphasized that the work done against the induced electromotive force is necessary for the current to reach its final equilibrium value. So our result shows that the stored magnetic energy (which is exactly half the work done by the power supply) comes from the Poynting vector that crosses the surface of the solenoid. The other half of the work done is the price that one must pay in order to achieve a final equilibrium state for the current. This other half of the work done finds its way as work done against the induced electromotive force in the windings of the solenoid.

This is exactly analogue to the case of charging a capacitor by a power supply, in which it was shown [23] that the stored electric energy in the capacitor comes from the energy carried by the Poynting vector that crosses the plates of the capacitor, and this energy is exactly half the energy delivered by the power supply. While the other half is carried by the Poynting vector that crosses the connecting wires. Another analogue case is the two capacitor problem: When a charged capacitor is connected to an uncharged one with the same capacitance, exactly half the stored energy disappears after the charge transfer is completed. In these analogue cases, it was noted in earlier work that if the presence of nonzero resistance in the circuit is assumed, the amount of Joule heat loss in the resistor becomes exactly the same as the missing energy [29]. Others [25,27,30] used superconducting wires and have tried different mechanisms to explain this energy loss and they arrived at the same conclusion. Another example in mechanics: if a particle collides, in a completely inelastic collision, with another stationary particle of the same mass then exactly half the initial kinetic energy will be lost in the collision. Our solenoid problem is another one, but here the energy loss is due to the work done against the induced electromotive force. Therefore, regardless of the nature of the mechanism, the amount of the energy loss should always be exactly half the supplied energy of the power supply. It must be emphasized that this energy loss, in all the above cases and possible similar ones, is necessary (or the price that one must pay) to transform the system from an initial

non-equilibrium state to a final equilibrium one [23,26]. We must note that our results do not change if one chooses a different function for the current, in which case the reader can easily verify this.

4. Conclusions

We considered an infinite solenoid which is fed by a current that increases linearly in time over a time period T , after which the current reaches its final value. Our results showed that during that period, the electromagnetic linear momentum density is exactly balanced by the hidden momentum density. In other words, the electromagnetic force density is exactly balanced by the hidden force density. This keeps the total linear momentum density and the total force density zeros at any time during that period. Which is consistent with the situation before the current is turned on. It was also shown that the stored magnetic energy inside the solenoid is exactly half the energy delivered by the power supply. This stored magnetic energy is just the energy which is carried by the Poynting vector that crosses the surface of the solenoid. The other half is consumed against the induced electromotive force which is needed to transfer the system to a final equilibrium state. The system we considered is analogue to other systems: In the process of charging a capacitor by a power supply, half the energy delivered by the power supply appears as electric energy inside the capacitor. In the two capacitor problem, half the initial energy is lost (when the capacitances of the two capacitors are the same). In mechanics, the completely in-elastic collision is another example, in which half the initial kinetic energy is lost when an incident particle collides with another stationary similar particle. In our present solenoid problem and in all the above mentioned systems, the missing energy is necessary in order to transfer the system from an initial non-equilibrium state to a final equilibrium state.

REFERENCES

- [1] J. Sod-Hoffs and V. S. Manko, "The Poynting vector of a charged magnetic dipole: two limiting cases," *Journal of Physics: Conference Series*, Vol. 91, No. 1, pp. 2011–2015, 2007.
- [2] J. L. Jimenez, I. Campos, and N. Aquino, "Exact electromagnetic fields produced by a finite wire with constant current," *European Journal of Physics*, Vol. 29, No. 1, pp. 163–175, January 2008.
- [3] X. Zangcheng, G. Changlin, Z. Zongyan, T. Fukamachi, and R. Negishi, "The relationship between the Poynting vector and the dispersion Surface in the Bragg case," *Journal of Physics: Condensed Matter*, Vol. 9, No. 18, pp. 75–78, 1997.
- [4] N. Morton, "An introduction to the Poynting vector," *Physics Education*, Vol. 14, No. 5, pp. 301–304, 1979.
- [5] V. S. Manko, E. D. Rodchenko, B. I. Sadovnikov, and J. Sod-Hoffs, "The Poynting vector of axistationary electrovac space times reexamined," *Classical and Quantum Gravity*, Vol. 23, No. 27, pp. 5385–5395, 2006.
- [6] J.-Y. Ji, C.-W. Lee, J. Noh, and W. Jhe, "Quantum electromagnetic fields in the presence of a dielectric microsphere," *Journal of Physics B: Atomic, Molecular and Optical Physics*, Vol. 33, No. 21, pp. 4821–4831, 2000.
- [7] P. Seba, U. Kuhl, M. Barth, and H. Stöckmann, "Experimental verification of the topologically induced vortices inside a billiard," *Journal of Physics A: Mathematical and General*, Vol. 32, No. 47, pp. 8225–8230, 1999.
- [8] N. R. Sadykov, "Evolution equation of the Korteweg – de Vries type for the Poynting vector amplitude," *Quantum Electronics*, Vol. 27, No. 2, pp. 185–187, 1997.
- [9] D. F. Nelson, "Generalizing the Poynting vector," *Physical Review Letters*, Vol. 76, No. 25, pp. 4713–4716, June 1996.
- [10] A. L. Kholmetskii and T. Yarman, "Apparent paradoxes in classical electrodynamics: A fluid medium in an electromagnetic field," *European Journal of Physics*, Vol. 29, No. 6, pp. 1127–1134, 2008.
- [11] A. Gsponer, "On the electromagnetic momentum of static charge and steady current distributions," *European Journal of Physics*, Vol. 28, No. 5, pp. 1021–1042, 2007.
- [12] J. M. Aguirregabiria, A. Hernández, and M. Rivas, "Linear momentum density in quasi static electromagnetic systems," *European Journal of Physics*, Vol. 25, No. 4, pp. 555–567, 2004.
- [13] X. S. Zhu and W. C. Henneberger, "Some observations on the dynamics of the Aharonov-Bohm effect," *Journal of Physics A: Mathematical and General*, Vol. 23, No. 17, pp. 3983–3990, 1990.
- [14] D. G. Lahoz and G. M. Graham, "Experimental decision on the electromagnetic momentum expression for magnetic media," *Journal of Physics A: Mathematical and General*, Vol. 15, No. 1, pp. 303–318, 1982.
- [15] S. M. Kim and G. Gbur, "Momentum conservation in partially coherent wave fields," *Physical Review A*, Vol. 79, No. 3, pp. 3844–3849, March 2009.
- [16] M. Mansuripur and A. R. Zakharian, "Maxwell's macroscopic equations, the energy-momentum postulates, and the Lorentz law of force," *Physical Review E*, Vol. 79, No. 2, pp. 6608–6617, 2009.
- [17] G. N. Gaidukov and A. A. Abramov, "An interpretation of the energy conservation law for a point charge moving in a uniform electric field," *Physics-Uspekhi*, Vol. 51, No. 2, pp. 163–166, 2008.
- [18] A. B. Pippard, "Change of energy of photons passing through rotating anisotropic elements," *European Journal of Physics*, Vol. 15, No. 2, pp. 79–80, 1994.
- [19] A. L. Kholmetskii and T. Yarman, "Energy flow in a bound electromagnetic field: Resolution of apparent paradoxes," *European Journal of Physics*, Vol. 29, No. 6, pp. 1135–1146, 2008.

- [20] M. F. Bishop and A. A. Maradudin, "Energy flow in a semi-infinite spatially dispersive absorbing dielectric," *Physical Review B*, Vol. 14, pp. 3384–3393, 1976.
- [21] F. Richter, M. Forian, and K. Henneberger, "Poynting's theorem and energy conservation in the propagation of light in bounded media," *Europhysics Letters*, Vol. 81, No. 6, pp. 7005–7009, 2008.
- [22] R. A. Powell, "Two-capacitor problem: A more realistic view," *American Journal of Physics*, Vol. 47, No. 5, pp. 460–462, May 1979.
- [23] S. M. AL-Jaber and S. K. Salih, "Energy consideration in the two-capacitor problem," *European Journal of Physics*, Vol. 21, No. 4, pp. 341–345, 2000.
- [24] A. M. Sommariva, "Solving the two capacitor paradox through a new asymptotic approach," *IEE Proceedings of Circuits Devices Systems*, Vol. 150, No. 3, pp. 227–231, 2003.
- [25] D. P. Korfiatis, "A new approach to the two-capacitor paradox," *WSEAS Transactions on Circuits Systems*, Vol. 6, pp. 76–79, 2007.
- [26] A. M. Abu-Labdeh and S. M. AL-Jaber, "Energy consideration from non-equilibrium to equilibrium state in the process of charging a capacitor," *Journal of Electrostatics*, Vol. 66, No. 3–4, pp. 190–192, 2008.
- [27] K. Lee, "The two-capacitor problem revisited: a mechanical harmonic oscillator model approach," *European Journal of Physics*, Vol. 30, No. 1, pp. 69–74, 2009.
- [28] D. Babson, P. Reynolds, R. Bjorkquist, and D. J. Griffiths, "Hidden momentum, field momentum, and electromagnetic impulse," *American Journal of Physics*, Vol. 77, No. 9, pp. 826–833, 2009.
- [29] C. Cuvaj, "On conservation of energy in electric circuits," *American Journal of Physics*, Vol. 36, No. 10, pp. 909–910, 1968.
- [30] T. B. Boykin, D. Hite, and N. Singh, "The two capacitor problem with radiation," *American Journal of Physics*, Vol. 70, No. 4, pp. 415–420, 2002.

Exact Solutions of Equations for the Strongly-Conductive and Weakly-Conductive Magnetic Fluid Flow in a Horizontal Rectangular Channel

Mingjun Li¹, Xinrong Zhang², Hiroshi Yamaguchi³

¹School of mathematics and computational Science, Xiangtan University, Xiangtan, China; ²Department of Energy and Resources Engineering, College of Engineering, Peking University, Beijing, China; ³Faculty of Mechanical Engineering, Doshisha University, Kyoto, Japan.
Email: limingjun@xtu.edu.cn, alimingjun@163.com

Received April 1st, 2009; revised May 5th, 2009; accepted June 23rd, 2009.

ABSTRACT

This paper presents the results of exact solutions and numerical simulations of strongly-conductive and weakly-conductive magnetic fluid flows. The equations of magnetohydrodynamic (MHD) flows with different conductivity coefficients, which are independent of viscosity of fluids, are investigated in a horizontal rectangular channel under a magnetic field. The exact solutions are derived and the contours of exact solutions of the flow for magnetic induction modes are compared with numerical solutions. Also, two classes of variational functions on the flow and magnetic induction are discussed for different conductivity coefficients through the derived numerical solutions. The known results of the phenomenology of magnetohydrodynamics in a square channel with two perfectly conducting Hartmann-walls are just special cases of our results of magnetic fluid.

Keywords: Magnetic Fluid, Variational Function, Conductivity Coefficient, Strongly-Conductive, Weakly-Conductive

1. Introduction

The first classical study of electro-magnetic channel flow was carried out by Hartmann in the 1930s [1]. Hartmann's well-known exact solution can be applied to very closely related problems in magneto-hydrodynamics (MHD) to appreciably simplify physical problems and give insights into new physical phenomena.

In magnetic fluids, the fluid dynamic phenomena with magnetic induction create new difficulties for the solution of the problems under consideration. The classical Hartmann flow can be further generalized to include arbitrary electric energy extraction from or addition to the flow. In general, classical MHD flows are dealt with using the exact solution of the Couette flow which is presented when the magnetic Prandtl number is unity [1].

The exact solutions of appropriately simplified physical problems provide estimates for the approximate solutions of complex problems. In view of its physical importance, the flow in a channel with a considerable length, rectangular, two-dimensional, and unidirectional cross section, which is assumed steady, pressure-driven

of an incompressible Newtonian liquid, is the simplest case to be considered. In such a flow, taking into account the symmetrical planes $y=0$ and $z=0$ and an exact solution is obtained by using the separation of variables. The solution indicates that, when the width-to-height ratio increases, the velocity contours become flatter away from the two vertical walls and that the flow away from the two walls is approximately one-dimensional (the dependence of u_x on y is weak) [2].

If all walls are electrically insulating, $\sigma_w = 0$, Shercliff (1953) has investigated principle sketch of the phenomenology of Magnetohydrodynamics (MHD) channel flow of rectangular cross-section with Hartmann walls and side walls [3]. For perfectly conducting Hartmann walls, $\sigma = \infty$, Hunt (1965) gave velocity profile and current paths for different Hartmann number. They found that the current density is nearly constant in most of channel cross sections, the velocity distribution is flat, and the thickness of the side layers decreases with increasing intensity of \mathbf{B} , i.e. increasing Hartmann number [3]. Recently, Carletto, Bossis and Ceber defined the ratio magnetic energy of two

aligned dipoles to the thermal energy $\mathcal{G} = \pi\mu_0\beta^2 a^2 H_0^2 / kT$, and their theory well predicts the experimental results in a constant unidirectional field [4]. Further results can be found in reference [5].

Other flow configurations in basic MHD may include Hele-Shaw cells. Wen *et al.* [6,7] were motivated to visualize the macroscopic magnetic flow fields in a square Hele-Shaw cell with shadow graphs for the first time, taking advantage of its small thickness and corresponding short optical depth. Examples of applications of MHD include the chemical distillatory processes, design of heat exchangers, channel type solar energy collectors and thermo-protection systems. Hence, the effects of combined magnetic forces due to the variations of magnetic fields on the laminar flow in horizontal rectangular channels are important in practice [8–10].

In the present study, we consider the characteristics of magnetic fluids in a horizontal rectangular channel under the magnetic fields and use the flow equations with a conductivity coefficient. The exact solutions of the strongly-conductive and weakly-conductive magnetic fluids are considered using the series expansion technique in order to obtain the relationship between the flow and magnetic induction. Also, a quadratic function on flow and magnetic induction is studied to verify the characteristic of flow field using the obtained solutions.

2. The Exact Solution of the Magnetic Fluid Equations

The configuration of the flow geometry is illustrated in **Figure 1**. The problem considered in this study is an incompressible steady flow in the positive x -direction with a magnetic field applied in the positive z -direction. The cross-section of the channel is given by the flow region $2a$ and $2b$ while the channel length is $2c$. The system of basic magnetic fluid equations is given as follows [5]

$$\nabla \cdot \mathbf{U} = 0 \quad (1)$$

$$\rho \frac{D\mathbf{U}}{Dt} = -\nabla p + \eta \nabla^2 \mathbf{U} + \mathbf{j} \times \mathbf{B} + (\mathbf{M} \cdot \nabla) \mathbf{H} + \mathbf{M} \times (\nabla \times \mathbf{H}) + \mathbf{F} \quad (2)$$

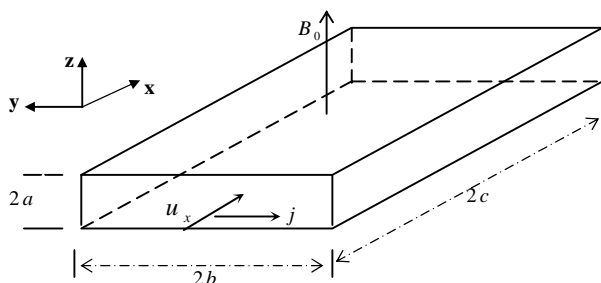


Figure 1. Illustration of flows in a rectangular channel

The Maxwell's equations in their usual form

$$\nabla \cdot \mathbf{B} = 0, \nabla \times \mathbf{E} = -\frac{\partial \mathbf{B}}{\partial t}, \nabla \cdot \mathbf{E} = -\frac{\rho_e}{K_0} \quad (3)$$

with the relation equations and the Ohm's law given as

$$\mathbf{B} = \mu_0 \mathbf{H} + \mathbf{M} = (\mu_0 + \chi_m) \mathbf{H} \quad (4)$$

$$\mathbf{j} = \sigma(\mathbf{E} + \mathbf{U} \times \mathbf{B}) \quad (5)$$

where μ_0 is the permeability of free space, χ_m is the magnetic susceptibility (H/m), σ is the conductivity, \mathbf{B} is the magnetic induction, \mathbf{H} is the magnetic field (A/m), and \mathbf{M} is the magnetization (A/m).

We choose the x axis such that the velocity vector of the fluid is $\mathbf{U} = (u_x, 0, 0)$ and from the continuity Equation (1), we have $u_x = u_x(y, z)$. We also choose $\mathbf{B} = \mathbf{B}_0 + \mathbf{b} = (b_x, 0, B_0)$, where B_0 is a constant representing magnetic induction.

Applying the Maxwell's equation $\nabla \cdot \mathbf{B} = 0$ and $\partial b_x / \partial x = 0$, we have $b_x = b_x(y, z)$. To simplify our presentations, the following assumptions are made for related variables:

$$\mathbf{U} = (u_x, 0, 0), \mathbf{j} = (0, j_y, j_z) \quad (6)$$

$$\mathbf{E} = (0, E_y, E_z), \mathbf{B} = \mathbf{B}_0 + \mathbf{b} = (b_x, 0, B_0) \quad (7)$$

$$\mathbf{H} = (H_x, 0, H_0) \quad (8)$$

$$\mathbf{M} = (M_x, 0, M_0), \mathbf{F} = (F_x, 0, 0) \quad (9)$$

And $\nabla \cdot \mathbf{E} = 0$, Equation (3) is satisfied. As there is no excess charge in the fluid, then, by using (5), \mathbf{j} is obtained as follows

$$\begin{aligned} \mathbf{j} &= (0, j_y, j_z) = (0, \sigma(E_y - u_x B_0), \sigma E_z) \\ &= (0, \frac{1}{\mu_0} \frac{\partial b_x}{\partial z}, -\frac{1}{\mu_0} \frac{\partial b_x}{\partial y}) \end{aligned} \quad (10)$$

$$\frac{\partial E_z}{\partial y} = \frac{\partial E_y}{\partial z} \quad (11)$$

The magnetic fluid boundary conditions considered here are

$$b_x = 0 \text{ at } y = \pm b, z = \pm a$$

$$u_x = 0 \text{ at } y = \pm b, z = \pm a$$

We shall also assume that all quantities are independent of time t , that is to say, the fluid we consider here is in a steady state.

2.1 The Strongly-Conductive Fluid

The magnetic fluid is called strongly-conductive if the term $\mathbf{M} \times (\nabla \times \mathbf{H})$ appears [8]. Under the condition of strongly conductive, the coefficient $\mathbf{M} \times (\nabla \times \mathbf{H})$ is much

larger than the Kelvin force density $(\mathbf{M} \cdot \nabla)\mathbf{H}$ so that $\mathbf{J} \times \mathbf{B}$ is considered while $(\mathbf{M} \cdot \nabla)\mathbf{H}$ is neglected. Using the steady-state assumption, i.e., $\partial/\partial t = 0$, Equation (2) can be written as follows

$$\eta \left(\frac{\partial^2 u_x}{\partial y^2} + \frac{\partial^2 u_x}{\partial z^2} \right) = \frac{\partial(p' - f'_x)}{\partial x} - (1 - \mu_0 \chi_m (\mu_0 + \chi_m)^{-2}) j_y B_0 \quad (12)$$

$$\frac{\partial p'}{\partial y} = j_z b_x \quad (13)$$

$$\frac{\partial p'}{\partial z} = -j_y b_x \quad (14)$$

where $p' = p - 1/2 \chi_m H_x^2$. Note that Sutton and Sherman [1] gave an incorrect result in their equation (10.85) which should be the above Equation (14).

For Hartmann flow, it is feasible to replace E_y by $K \bar{u}_x B_0$ for a simple model, then $j_y = \sigma B_0 (K \bar{u}_x - u_x)$

where $\bar{u}_x = \frac{1}{4ab} \int_{-a}^a \int_{-b}^b u_x(y, z) dy dz$.

The axial pressure gradient $-\partial(p' - f'_x)/\partial x$ is taken to be $K\eta'$ if the gravitational field is neglected, and $\partial f'_x/\partial x = 0$, where $\eta' = \eta(1 - \mu_0 \chi_m (\mu_0 + \chi_m)^{-2})^{-1}$ is the viscosity of magnetic fluid. Combining Equations (12)–(14) yields

$$\eta' \left(\frac{\partial^2 u_x}{\partial y^2} + \frac{\partial^2 u_x}{\partial z^2} \right) + \frac{B_0}{\mu_0} \frac{\partial b_x}{\partial z} + K \eta' = 0 \quad (15)$$

$$B_0 \mu_0 \sigma \frac{\partial u_x}{\partial z} + \left(\frac{\partial^2 b_x}{\partial y^2} + \frac{\partial^2 b_x}{\partial z^2} \right) = 0 \quad (16)$$

Let

$$u_1 = u_x + \frac{b_x}{\mu_0 \sqrt{\sigma \eta'}}, \quad u_2 = u_x - \frac{b_x}{\mu_0 \sqrt{\sigma \eta'}} \quad (17)$$

then Equations (15) and (16) are reduced to

$$\frac{\partial^2 u_1}{\partial y^2} + \frac{\partial^2 u_1}{\partial z^2} + \frac{H_a \sqrt{\eta'^{-1} \eta}}{a} \frac{\partial u_1}{\partial z} + K = 0 \quad (18)$$

$$\frac{\partial^2 u_2}{\partial y^2} + \frac{\partial^2 u_2}{\partial z^2} - \frac{H_a \sqrt{\eta'^{-1} \eta}}{a} \frac{\partial u_2}{\partial z} + K = 0 \quad (19)$$

where the Hartmann number H_a is defined as $H_a = B_0 a \sqrt{\sigma \eta'^{-1}}$.

The solution for u_1 is obtained by expressing K over the range $-b < y < b$ as a cosine Fourier series,

$$K = \frac{4k_0}{\pi} \sum_{n=0}^{\infty} \frac{(-1)^n}{2n+1} \cos \frac{(2n+1)\pi y}{2b} \quad (20)$$

where k_0 is a constant. The solution for u_1 is then written

$$u_1 = \frac{16Kb^2}{\pi^3} \sum_{n=0}^{\infty} \frac{(-1)^n}{(2n+1)^3} \left[1 + \frac{e^{m_1 z} \sin hm_2 a - e^{m_2 z} \sin hm_1 a}{\sin h(m_1 - m_2)a} \right] \quad (21)$$

where m_1 and m_2 are given as

$$m_{1,2} = \frac{-H_a \sqrt{\eta'^{-1} \eta} b \pm \sqrt{b^2 H_a^2 \eta'^{-1} \eta + a^2 (2n+1)^2 \pi^2}}{2ab} \quad (22)$$

It should be pointed out that the solution for u_2 is just the same function as u_1 in which m_1 and m_2 are displaced by m_3 and m_4 , respectively, which are given by

$$m_{3,4} = \frac{H_a \sqrt{\eta'^{-1} \eta} b \pm \sqrt{b^2 H_a^2 \eta'^{-1} \eta + a^2 (2n+1)^2 \pi^2}}{2ab} \quad (23)$$

2.2 The Weakly-Conductive Fluid

If the fluid is weakly-conductive and the field \mathbf{E} is not time-dependent, the term $\mathbf{M} \times (\nabla \times \mathbf{H})$ will disappear as shown in equations (104) [8]. Considering Equation (2) through (4) and making use of the assumptions mentioned above, the following relations are obtained,

$$\eta \left(\frac{\partial^2 u_x}{\partial y^2} + \frac{\partial^2 u_x}{\partial z^2} \right) = \frac{\partial(p - f'_x)}{\partial x} - j_y B_0 \quad (24)$$

$$\frac{\partial p}{\partial y} = j_z b_x \quad (25)$$

$$\frac{\partial p}{\partial z} = -j_y b_x \quad (26)$$

Replacing E_y with $K \bar{u}_x B_0$, we have $j_y = \sigma B_0 (K \bar{u}_x - u_x)$ as well as in Subsection 2.1. Then, as the axial pressure gradient $-\partial(p - f'_x)/\partial x$ is taken to be $K\eta$, where

$$K = \frac{4k_0}{\pi} \sum_{n=0}^{\infty} \frac{(-1)^n}{2n+1} \cos \frac{(2n+1)\pi y}{2b} \quad (27)$$

where k_0 is a constant. Let

$$u_1 = u_x + \frac{b_x}{\mu_0 \sqrt{\sigma \eta}}, \quad u_2 = u_x - \frac{b_x}{\mu_0 \sqrt{\sigma \eta}} \quad (28)$$

Thus, the solution of Equation (28) for u_1 as in (17) is also obtained

$$u_1 = \frac{16Kb^2}{\pi^3} \sum_{n=0}^{\infty} \frac{(-1)^n}{(2n+1)^3} \left[1 + \right.$$

$$\frac{e^{m_1 z} \sin h m_2 a - e^{m_2 z} \sin h m_1 a}{\sin h(m_1 - m_2)a}] \times \cos \frac{(2n+1)\pi y}{2b} \quad (29)$$

where m_1 and m_2 are as follows

$$m_{1,2} = \frac{-H_a b \pm \sqrt{H_a^2 b^2 + a^2 (2n+1)^2 \pi^2}}{2ab} \quad (30)$$

Note that the solution for u_2 is the same function as u_1 in which m_1 and m_2 are given as follows

$$m_{3,4} = \frac{H_a b \pm \sqrt{H_a^2 b^2 + a^2 (2n+1)^2 \pi^2}}{2ab} \quad (31)$$

For a weak-conductive fluid, its solution is simply the solution of the conductive fluid with a conductive coefficient $\lambda = \sqrt{\eta'^{-1}\eta} = 1.0$ (for $\mu_0 = 0$). We find that $\lambda = \sqrt{\eta'^{-1}\eta} = \sqrt{1 - \mu_0 \chi_m (\mu_0 + \chi_m)^{-2}}$ which is obviously independent of the fluid viscosity.

2.3 Unidirectional Two Dimensional Flow without a Magnetic Field

Here we only consider a unidirectional two dimensional flow without a magnetic field, so that $H_a = 0$, Equations (18) and (19) are reduced to

$$\frac{\partial^2 u_x}{\partial y^2} + \frac{\partial^2 u_x}{\partial z^2} + K = 0 \quad (32)$$

The boundary conditions are as follows

$$\frac{\partial u_x}{\partial y} = 0 \quad \text{at } y = -b \quad (33)$$

$$\frac{\partial u_x}{\partial z} = 0 \quad \text{at } z = -a \quad (34)$$

$$u_x = 0 \quad \text{at } y = b, \quad z = a \quad (35)$$

In order to obtain an exact solution of Equation (32), comparing with our above results, we have

$$K = \frac{4k_0}{\pi} \sum_{n=0}^{\infty} \frac{(-1)^n}{2n+1} \cos \frac{(2n+1)(y+b)\pi}{2b} \quad (36)$$

where k_0 is a constant. The problem consisting Equation (32) and its conditions are solved similarly using the separation of variables, which has the solution as follows [9]

$$u_x(y, z) = \frac{Ka^2}{2} \left(1 - \left(\frac{z+a}{2a} \right)^2 + 4 \sum_{n=0}^{\infty} \frac{(-1)^n}{a_n^3} \cosh \left[\frac{a_n(y+b)}{2a} \right] \right) \left[\cosh \left(\frac{a_n b}{2a} \right) \right]^{-1} \cos \left[\frac{a_n(z+a)}{2a} \right] \quad (37)$$

where

$$a_n = (2n-1) \frac{\pi}{2}, \quad n = 1, 2, \dots \quad (38)$$

2.4 The Solutions, Flow Field and Discussions

In the present study, the flow fields and their associated functions are presented in the flow region with $a=1$, $b=1$. Since H_a ranges from 10 to 100 in most practical problems, the initial magnetic induction is taken to be $B_0 = 10 \text{ (kg.s}^{-2}.\text{A}^{-1}\text{)}$, $\mu_0 = 4\pi 10^{-7} \text{ (H/m)}$, $H_a = 50$ and the constant $k_0 = 10$.

Figure 2 depicts the solutions for $\lambda = 0.02, 0.2$ and 1.0 , where $\lambda = \sqrt{\eta'^{-1}\eta}$ is the conductivity coefficient. The velocity contours are displayed in **Figure 2(a)** for different values of the conductivity coefficient. It is shown that the velocity gradients become larger gradually near four vertical walls as the conductivity coefficient increases for different magnetic fluids. On the contrary, in the region of (0,0), the velocity gradients lower gradually as the conductivity coefficient increases. For the case of a constant Hartmann number, the magnetic fluid are shown in **Figure 2(b)** for different values of the conductivity coefficient, and as indicated, the strength of magnetic induction dampens horizontal away from the plane $z=0$ and the walls $z=\pm 1$ as the conductivity coefficient increases. On the contrary, near the walls $y=\pm 1$, the magnetic induction becomes gradually low as the conductivity coefficient increases. For conductivity coefficient $\lambda = 0.02$, the flow contours are similar to those in the reference [10] for the magnetic Rayleigh number $Ram = 0.0$ and the Rayleigh number $Ra = 1,000$. Our analysis shows that the flow field changes with different conductivity coefficients.

Figure 3 shows the velocity fields for steady, unidirectional flows in a rectangular channel and K is a cosine Fourier series of y and conductivity coefficient $\lambda = 0$. The velocity contours are similar to those given by Papanastasiou et al. for the width-to-height ratio 1:1 [2].

In **Figures 4(a)** and **4(b)**, the development of the velocity profile in y and z directions are shown for various values of the conductivity coefficient λ . For the symmetry, we only consider two cases: (a) $0 \leq y \leq b$, $-a \leq z \leq a$; and (b) $0 \leq z \leq a$, $-b \leq y \leq b$. Several interesting observations are readily made from the results. The cooperate process of y and z is shown in the above analysis. In order to clearly show the self-governed process of y and z , the contours of the velocity versus coordinate y , and the velocity versus coordinate z are given. It is clear that the velocity gradients increase quickly near the boundary walls $z=\pm a$ and $y=\pm b$ as λ is increased. On the other hand, the exact solutions are multiple hyper-cosine functions of z , and cosine functions of y . Therefore, the velocity gra-

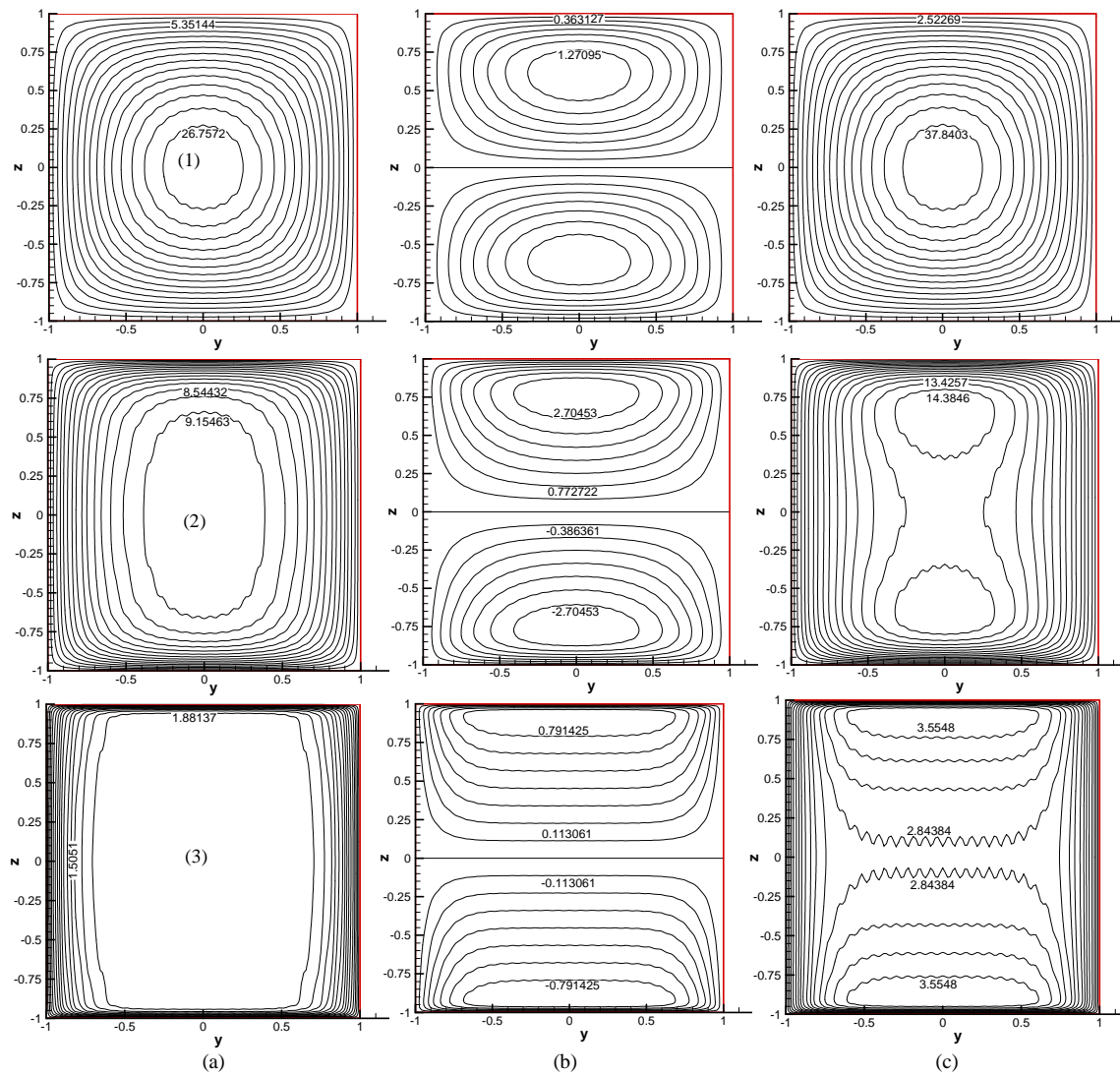


Figure 2. The distribution of flow field and magnetic induction. (a) Velocity contours u_x ; (b) Magnetic induction distributions b_x ; and (c) The velocity composition function F . (1) $H_a = 50$, $\lambda = 0.02$; (2) $H_a = 50$, $\lambda = 0.2$; and (3) $H_a = 50$, $\lambda = 1.0$

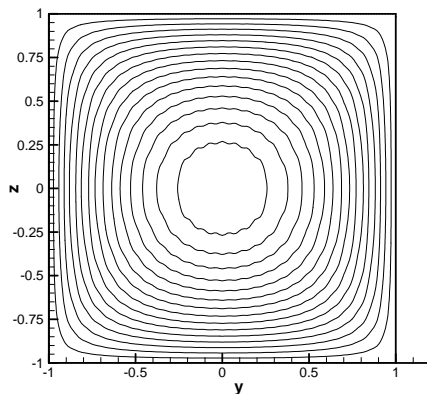


Figure 3. Velocity field with a cosine Fourier series K of y for conductive coefficient $\lambda = 0$

dient is larger near the boundary walls $y = \pm b$ than that near the boundary walls $z = \pm a$ for a given λ .

For a given Hartmann number, comparing **Figure 2** of this paper with Figures 3.2, 3.3 and 3.4 of Reference [3], current density distribution magnetic fluid and magneto-hydrodynamics (MHD) are the same. Comparing **Figure 2** of this paper with Figure 3.1 of Reference [3], the velocity profile of the phenomenology is also same for magnetic fluid and MHD. Of course, magnetic fluid and MHD have different equations and formulations of the Hartmann number. For magnetic fluid, the constitutive equation is $\mathbf{B} = \mu\mathbf{H} + \mathbf{M}$, the Hartmann number $H_a = B_0 a \sqrt{\sigma\eta^{-1}}$ and conductivity coefficient λ are introduced in our work. The flow and magnetic induction

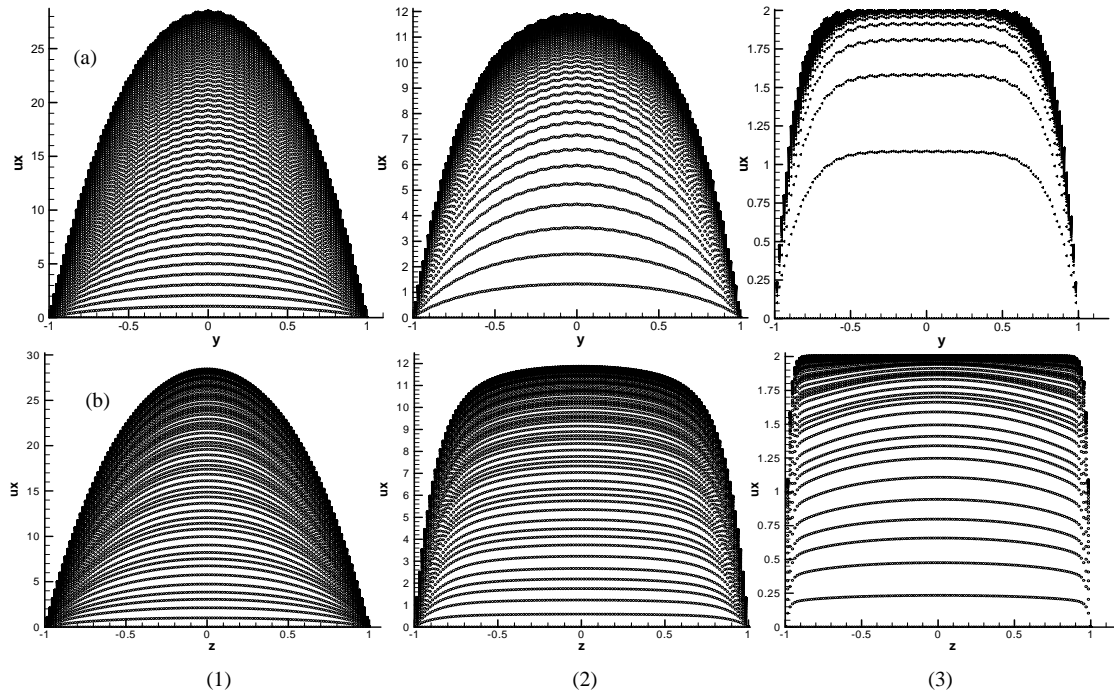


Figure 4. The development of the velocity profile (a) The u_x vs y -axis; (b) u_x vs z -axis. (1) $H_a = 50$, $\lambda = 0.02$; (2) $H_a = 50$, $\lambda = 0.2$; (3) $H_a = 50$, $\lambda = 1.0$

change with different λ . Differently, in MHD, Shercliff and Hunt considered the induction equation $\frac{\partial \mathbf{B}}{\partial t} + (\mathbf{V} \cdot \nabla) \mathbf{B} = \frac{1}{\mu \sigma} \nabla^2 \mathbf{B} + (\mathbf{B} \cdot \nabla) \mathbf{V}$ and used only the linear constitutive equation $\mathbf{B} = \mu \mathbf{H}$ with Hartmann number $H_a = LB_0 \sqrt{\sigma / \rho \mu}$. They gave velocity profile and current paths for different Hartmann number.

3. Two Class of Variational Functions on the Flow and Magnetic Induction

For many years the variation techniques have been effectively applied to problems in the theory of elasticity. However, they are rarely used in fluid dynamic problems. The great utility in elasticity problems are due to the fact that they can be conveniently applied to linear problems. This, of course, explains why they are not frequently used in fluid dynamics since most such problems are nonlinear [10,11].

For the conductive fluid problems of the type being considered here, we recall the governing Equations (15) and (16) which are linear for u_x and b_x and the variation technique may be tried. Firstly, consider the following integral [12]

$$I(u_x, b_x; \lambda) = \iint_s F(y, z, \lambda; u_x, b_x, \lambda) dy dz \quad (39)$$

where F is some given function of u_x, b_x, λ . Clearly, the value of the integral depends on the choice of the functions $u_x(y, z, \lambda)$, $b_x(y, z, \lambda)$ and λ . Now, let us pose the following problem: to obtain functions u_x, b_x and λ to minimize the value of I . As is well known from variational calculus, the necessary conditions that u_x, b_x and λ for minimized I are the Euler equations:

$$\frac{\partial F}{\partial y} - \frac{\partial}{\partial y} \left(\frac{\partial F}{\partial u_x} \right) - \frac{\partial}{\partial y} \left(\frac{\partial F}{\partial b_x} \right) = 0 \quad (40)$$

$$\frac{\partial F}{\partial z} - \frac{\partial}{\partial z} \left(\frac{\partial F}{\partial u_x} \right) - \frac{\partial}{\partial z} \left(\frac{\partial F}{\partial b_x} \right) = 0 \quad (41)$$

$$\frac{\partial F}{\partial \lambda} - \frac{\partial}{\partial \lambda} \left(\frac{\partial F}{\partial u_x} \right) - \frac{\partial}{\partial \lambda} \left(\frac{\partial F}{\partial b_x} \right) = 0 \quad (42)$$

3.1 Decomposition and Composition Functions on the Flow and Magnetic Induction

Simply, let the parameters be fixed at λ , then $s = [-a, a] \times [-b, b]$. According to u_1 and u_2 in the Equation (17), we only considered the function of u_x, b_x and λ in order to minimize the special function as follows

$$F = ((u_a)^2 + (u_b)^2)^{1/2}$$

$$= \frac{1}{2} \left(\left(u_x + \frac{b_x}{\mu_0 \sqrt{\sigma \eta}} \right)^2 + \left(u_x - \frac{b_x}{\mu_0 \sqrt{\sigma \eta}} \right)^2 \right)^{1/2} \quad (43)$$

where $u_x = u_x(y, z, \lambda)$ and $b_x = b_x(y, z, \lambda)$ are considered as the function of y , z and $\lambda = \sqrt{\eta^{-1} \eta}$, $-a \leq z \leq a$, $-b \leq y \leq b$, and $0 < \lambda_1 < \lambda < \lambda_2$.

Let $u_a = u_1/2 = (u_x + \tilde{c} b_x)/2$, $u_b = u_2/2 = (u_x - \tilde{c} b_x)/2$, then $u_x = u_a + u_b$. The expressions of u_a and u_b are called the velocity decompositions of the magnetic induction b_x and the flow field u_x with a variable coefficient \tilde{c} of the flow and the magnetic induction, where $\tilde{c} = (\mu_0 \sqrt{\sigma \eta})^{-1}$. From **Figure 5**, it is easy to show that $u_a \rightarrow u_x/2$, $u_b \rightarrow u_x/2$, and $F \rightarrow \sqrt{2}/2 u_x$ as $b_x \rightarrow 0$, where F is the velocity composition of the flow field and the magnetic induction.

It is also easy to know that $F = F(y, z, \lambda)$ has the same variation characteristic as the following function

$$\tilde{F} = \left(u_x + \frac{b_x}{\mu_0 \sqrt{\sigma \eta}} \right)^2 + \left(u_x - \frac{b_x}{\mu_0 \sqrt{\sigma \eta}} \right)^2 \quad (44)$$

The differential of \tilde{F} on λ is given by

$$\tilde{F}_\lambda = 2(u_x u'_{x,\lambda} + \frac{b_x}{\mu_0 \sqrt{\sigma \eta}} b'_x b'_{x,\lambda}) \quad (45)$$

It is obvious that \tilde{F}_λ is a nonlinear function of λ , and is very complex to study the variation characteristics of \tilde{F} by using the method of mathematical analysis.

With Equation (45), the variation characteristics of the function \tilde{F} is determined by flow and magnetic induction as a function of λ .

3.2 A Total Energy Variational Function on the Flow and Magnetic Induction

Based on the above analysis of Equation (17), let $u_1 = u_x + \tilde{c} b_x$, $u_2 = u_x - \tilde{c} b_x$ with $\tilde{c} = (\mu_0 \sqrt{\sigma \eta})^{-1}$, we call $\tilde{c} b_x$ the velocity of magnetic fluid flow, which is equivalence to the velocity of magnetic fluid flow evoked by magnetic force. A total energy function is defined by

$$e = e_1 + e_2 = \frac{1}{2} \rho u_x^2 + \frac{1}{2} \rho (\tilde{c} b_x)^2 \quad (46)$$

where e_1 is the kinetic energy, e_2 is the magnetic energy.

By the calculus of variations, we have

$$e'_\lambda = e'_{1,\lambda} + e'_{2,\lambda} = \rho u_x u'_{x,\lambda} + \rho \tilde{c} b_x b'_{x,\lambda} \quad (47)$$

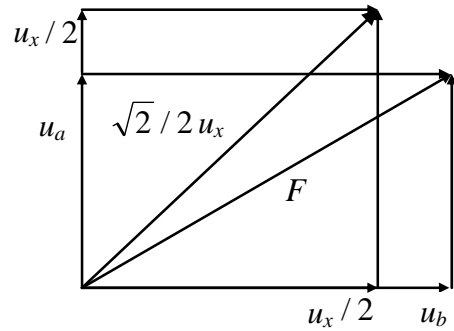


Figure 5. The sketch map of the composition function F of flow and magnetic induction

As u_x and b_x are nonlinear functions of λ , it is very complex to study the variational characteristics of e'_λ by using the method of mathematical analysis.

3.3 Numerical Calculations and Discussions

As seen in **Figures 2(a)** and **2(c)**, in a region of $(0,0)$, the contour of the function F is more similar to that of the flow for $\lambda = 0.02$. Furthermore, the gradient of flow which is larger than that of magnetic induction, the distribution value of F is largely affected depending on the flow. On the contrary, for $\lambda = 1.0$, the gradient of magnetic induction is larger than that of flow as F is largely affected depending upon the gradient of the magnetic induction.

It is observed that the difference of flow and magnetic induction are almost the same for $\lambda = 0.2$ in a region of $(0,0)$, where the distribution of the function F is determined by the gradients of both the magnetic induction and the flow in this region. Furthermore, near $y = \pm 1$ and $z = \pm 1$ for any λ , the difference of flow is acute singularly and the function F is also changed singularly. It is noted that F has only one limit point for $\lambda < 0.2$, and F has two limit points for $\lambda > 0.2$.

As seen in **Figure 6**, the gradient of the total energy is decided by the kinetic energy in the region $(0,0)$ for different values of λ , and near $y = \pm 1$ and $z = \pm 1$ for $\lambda = 0.02$. That is to say, the gradient of the magnetic energy is very large near $z = \pm 1$ for $\lambda = 0.02$, and its value is very small which does not affect the gradient of the total energy. Then, the gradient of the total energy will be affected by the magnetic energy near $z = \pm 1$ for $\lambda = 0.2$ and it will be affected by the magnetic energy near $y = \pm 1$ and $z = \pm 1$ for $\lambda = 1.0$.

4. Concluding Remarks

1) For magnetic fluid of this work and Magnetohydrodynamics (MHD) of Reference [3], the constitutive equa-

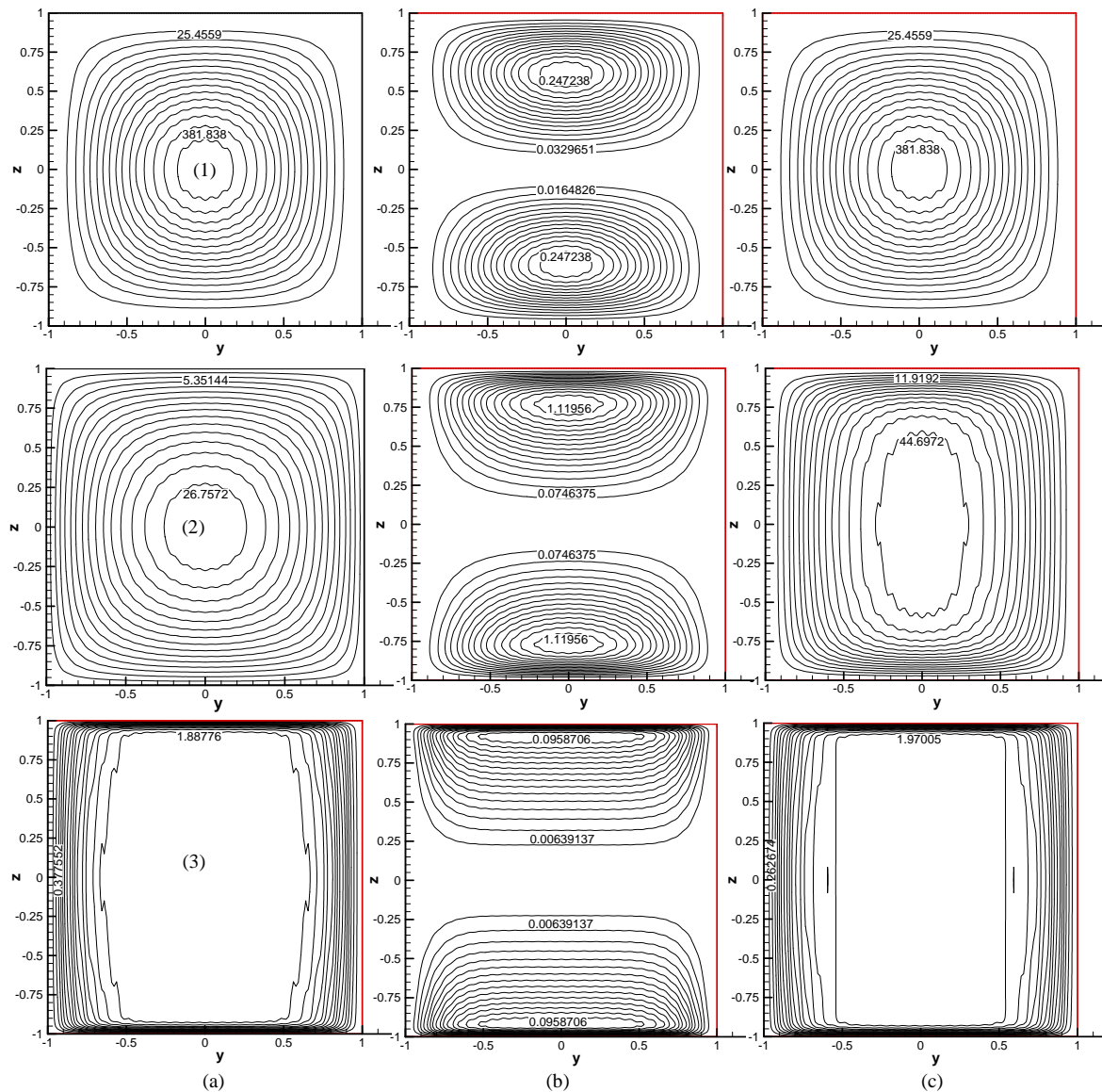


Figure 6. Illustration of energy function (a) The kinetic energy e_1 ; (b) The magnetic energy e_2 ; and (c) The total energy e .
(1) $H_a = 50$, $\lambda = 0.02$; (2) $H_a = 50$, $\lambda = 0.2$; (3) $H_a = 50$, $\lambda = 1.0$

tions are different, the Hartmann numbers are also different. For magnetic fluid, conductivity coefficient λ is an important coefficient to analyze the flow and the current. For MHD, Hartmann number H_a is the controlling coefficient, Shercliff and Hunt studied velocity profile and current paths for different Hartmann number [3–5].

2) For conductivity coefficient $\lambda = 0$, the velocity contours for steady unidirectional flow is shown in a rectangular channel with K a cosine Fourier series function of y . Our result is in agreement with published findings.

3) A velocity decomposition and composition function

F , and a total energy variational function e , on the flow and magnetic induction are considered. The variational characteristics of F are analyzed only using the characteristics of the resultant flow field and the magnetic induction, and the number of its limit points changes as λ changes. It is shown in numerical simulations that the gradient of total energy e is affected by the kinetic energy and the magnetic energy as λ changes.

4) Theoretically, the strongly-conductive and weakly-conductive magnetic fluid flows are studied on different conductivity coefficients which are independent of fluid viscosity in a horizontal rectangular channel.

Table 1. Nomenclature

a	channel length	H_a	Hatmann number
b	channel height	K	dimensionless variable $E_y/\bar{u}_x B_0$
C	channel width	k_0	constant
\mathbf{B}	magnetic induction	\mathbf{M}	magnetization (A/m)
B_0	initial magnetic field	M_0	initial magnetization
b_x	magnetic induction of x -direction	M_x	magnetization of x -direction
\tilde{c}	coefficient $\tilde{c} = (\mu_0 \sqrt{\sigma \eta})^{-1}$	u_x	velocity of x -direction
E	electric field with respect to Lab.	\bar{u}_x	average velocity
e	total energy	u_1	first exact solution
e_1	kinetic energy	u_2	second exact solution
e_2	magnetic energy	χ_m	the magnetic susceptibility
F	velocity composition function	μ_0	the magnetic susceptibility
F	force on a particle	σ	conductivity
\mathbf{H}	magnetic field(A/m)	η	viscosity of fluid
H_0	initial magnetic field	η'	the correctional viscosity of fluid
H_x	magnetic field of x -direction	λ	conductive coefficient $\lambda = \sqrt{\eta'^{-1} \eta}$

5. Acknowledgments

This work was supported in part by a grant to the research Centre for Advanced Science and Technology at Doshisha University from the Ministry of Education, Japan; the National Natural Science of China (10771178, 50675185, 10676031); the Research Fund for the Doctoral Program of Higher Education (20070530003), Program for New Century Excellent Talents in University (NCET 06-0708) and the Scientific Research Foundation for the Returned Overseas Chinese Scholars of State Education Ministry of China. The authors thank readers for giving references [3–5] and suggestions on comparison with analytical solutions.

REFERENCES

- [1] G. W. Sutton and A. Sherman, "Engineering Magnetohydrodynamics," McGraw-Hill Book Company, New York, 1965.
- [2] T. C. Papanastasiou, G. C. Georgiou, and A. N. Alexandrou, "Viscous fluid flow," CRC Press LLC, New York, 2000.
- [3] U. Mueller and L. Buehler, "Magnetofluidynamics in channel and containers," Springer-Verlag, Berlin, 2001.
- [4] P. Carletto, G. Bossis, and A. Cebers, "Structures in a magnetic suspension subjected to unidirectional and rotating field," International Journal of Modern Physics B, Vol. 16, No. 17–18, pp. 2279–2285, 2002.
- [5] E. Blums, A. Cebers, and M. M. Maiorov, "Magnetic fluids," Walter de G Gruyter, Berlin, 1997.
- [6] C.-Y. Wen and W.-P. Su, "Natural convection of magnetic fluid in a rectangular Hele-Shaw," Journal of Magnetism and Magnetic Materials, Vol. 289, pp. 299–302, March 2005.
- [7] C.-Y. Wen, C.-Y. Chen, and S.-F. Yang, "Flow visualization of natural convection of magnetic fluid in a rectangular Hele-Shaw cell," Journal of Magnetism and Magnetic Materials, Vol. 252, pp. 206–208, November 2002.
- [8] R. E. Rosensweig, "Ferrofluids: Magnetically controllable fluids and its applications," In: S. Odenbach, Ed., Basic Equations for Magnetic Fluids with Internal Rotations, Springer-Verlag, New York, p. 61, 2002.
- [9] T. H. Kuehn and R. J. Goldstein, "An experimental study of natural convection heat transfer in concentric and eccentric horizontal cylindrical annuli," ASME Journal of Heat Transfer, Vol. 100, pp. 635–640, 1978.
- [10] H. Yamaguchi, Z. Zhang, S. Shuchi, and K. Shimad, "Heat transfer characteristics of magnetic fluid in a partitioned rectangular box," Journal of Magnetism and Magnetic Materials, Vol. 252, pp. 203–205, November 2002.
- [11] G. B. Arfken and H. J. Weber, "Mathematical methods for physicists," 6th Edition, Elsevier Academic Press, New York, p. 1037, 2005.
- [12] H. Yamaguchi, "Engineering fluid mechanics," Springer-Verlag, New York, 2008.

A New Analysis Method for Locating the Focus and for Estimating the Size of the Focus of the Backscatter Light of a LIDAR System

Nianwen Cao¹, Weiyan Wang³, Yonghua Wu², Fred Moshary², Zhongrong Chen¹, Jiansong Huang¹

¹School of Atmospheric Physics, Nanjing University of Information Science & Technology, Nanjing, China; ²Department of Electrical Engineering, City College and Graduate School, City University of New York, New York, USA; ³Toshiba Stroke Research Center, University at Buffalo, New York, USA.
Email: nwcao@yahoo.com.cn

Received October 13th, 2009; revised November 14th, 2009; accepted November 19th, 2009.

ABSTRACT

This paper presents a new analysis method for locating the focus and estimating the size of the focus of the backscatter light of a Lidar system. The formula for calculating the uncertainty of the location of the focus of backscatter light of a Lidar system is given, and the estimation of the size of the focus is also presented. This calculation coincides with the analysis result of ZEMAX software. By the analysis, the experiment to exactly locate the focus of the backscatter light of Lidar is carried out.

Keywords: Backscatter Light, Focus, Telescope

1. Introduction

In traditional Lidar systems without optical fiber application and not eye-safe, the low-optical efficiency is due to: 1) The weak optical signal, especially, the Raman return signal; 2) The background noise. In eye-safe Lidar system, the active area of infrared detector (infrared photodiode) is very small, compared with photomultiplier-tube (PMT), only several millimeters [1]. Therefore, to focus the backscatter light completely on the active area of the detector and remove the background noise becomes very important. The size of the field stop (aperture) of telescope at the location of the focus defines the field of view (FOV) of the telescope, dominates the background noise. Smaller field stop greatly reduces the active area of the primary mirror of a telescope [2]; Therefore, the smaller field stop reduces the amount of the Lidar return signal reaching the detector and results in the inefficiency of the Lidar system. Field stop coupling with the size of focus of backscatter light can optimize the optical efficiency of a Lidar system.

Optical fiber has been conveniently and widely used in Lidar measurements. For instance, optical fiber is used in conical-scanning time-correction Lidar system to easily measure wind speed in different directions [3]. Recently, the optical fiber is well used in multi-wavelength Raman-Lidar system for aerosol measurements in the troposphere. The existing fiber to telescope match is dis-

cussed in reference [4] in detail. In Lidar measurements, especially, optical fiber-based Raman Lidar measurements, how to improve the Signal to Noise Ratio is a critical issue which has been investigated by many researchers. A novel rotational Raman and Rayleigh Lidar system incorporate a fiber-based optical element to analyze the narrow Raman spectral feature [5]. For non-coaxial Lidar system, how to match the telescope to optic fiber is analyzed in reference [6].

The combination of the Numerical Aperture (NA) (NA defines the maximal acceptance cone of the optical fiber as $n \sin \theta_{\max} = \sqrt{n_1^2 - n_2^2}$, where n_1 is the refractive index of the fiber core, and n_2 is the refractive index of the fiber cladding) of optical fiber and the size of the focus of a telescope can dominate the field of view (FOV) of a telescope, therefore, the maximal couple efficiency of the optical fiber and the telescope can be obtained. Reversely, the Numerical Aperture (NA) of optical fiber can also be designed by the size of focus of telescope.

Therefore, accurately locating the focus of the backscatter light of the Lidar system and estimating the size of the focus will contribute to the improvement of the optical efficiency in traditional Lidar system, and in optical fiber coupled telescope Raman or wind Lidar system, as well as in the infrared Lidar system with infrared photodiode.

In general, the researchers estimate the size of the focus of the backscatter light of a Lidar system by the

limitation of the diffraction (airy disk) of the primary mirror of the telescope to collimate backscatter light of Lidar to the active area of the detector or the optical fiber. Actually, the size of the focus of the backscatter light is much larger than the airy disk. In this case, much energy of backscatter light will be lost. To locate the focus of a telescope, researchers have considered pointing the telescope to the moon; however, it is not convenient [7]. Furthermore, the location of the focus is not accurate and the observed focus is blurry.

This paper presents a new analysis method and relative experiment to accurately locate the focus of the backscatter light of a Lidar system and to estimate the size of the focus.

2. Theoretic Analysis for Locating the Focus and Estimating the Size of the Focus of the Backscatter Light of a Lidar System

Theoretically, the size of the focus of the backscatter light of a Lidar system is identical to the airy disk, relative to the wavelength of the backscatter light and diameter of the primary mirror of a telescope (the size of airy disk is defined as $x = 1.22 \frac{\lambda f}{d}$, where d is the diameter of the primary mirror, λ is the wavelength of backscatter light, f is the focus of telescope). Actually, the blurry of image (or image error) of telescope optical systems always occurs. The divergence of incident light is not zero; therefore, the field of view of a telescope is not zero. The size of the focus of a telescope is much larger than the size of airy disk; therefore, we cannot regard the actual focus as an airy disk. This paper analyzes the location uncertainty of backscatter light's focus and the uncertainty of the focus size, according to the image optical path of a telescope.

For easy discussion, the optical path of Newtown telescope is shown in **Figure 1**. The refraction index of the object space and the image space is n ; the object space and image space of Newtown telescope overlap completely; the propagation direction of incident light in object space reverses in image space. **Figure 1** shows that the image distance variation is $\Delta x'$ and the image height variation is dh' from the variation of incident angle du . $\Delta x'$ and dh' will be close to zero when du is close to zero. Variation Δx ($\Delta x > \Delta x'$) is introduced for easy discussion. From **Figure 1**, Equations (1) and (2) can be easily deduced as follows:

$$du' \Delta x = dh' \quad (1)$$

$$du' (s' - \Delta x) = dh \quad (2)$$

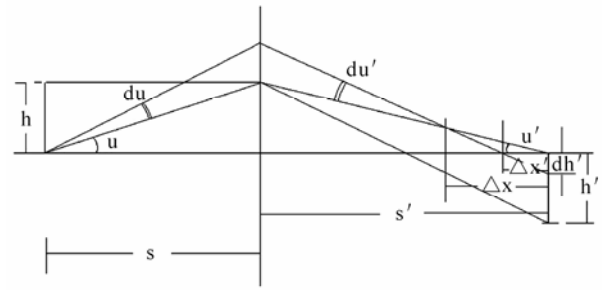


Figure 1. Analysis of optical path of telescope (h : the object height, h' : image height, u : incident angle, u' : the angle in image space corresponds to u in object space, du : variation of incident angle, du' : corresponds to du in object space, s : object distance, s' : image distance, $\Delta x'$: variation of image distance, Δx : variation introduced for easy discussion)

Equation (3) can be obtained from the combination of Equations (1) and (2):

$$dh' = du' s' - dh \quad (3)$$

s' is the image distance.

The refraction index in object space is identical to that in image space, Equation (4) exists.

$$hu = h'u' \quad (4)$$

Combine differential calculation of Equations (4) and (3), Equation (5) or (6) is obtained at $h = u's'$

$$\begin{aligned} dhu + hdu &= du' s' u' - dh u' + h' du' \\ &= hdu' - dh u' + h' du' \end{aligned} \quad (5)$$

$$dhu + hdu = hdu' - dh \frac{h}{s} + h' du' \quad (6)$$

Take $dh = sdu$, $h = us$ into account, Equation (7) can be obtained:

$$(2h + \frac{s}{s'} h) du = (h + h') du' \quad (7)$$

where s is the object distance,

$$h' = \beta h \quad (8)$$

β is amplification ratio of the image.

Equation (9) is obtained from the combination of (7) and (8).

$$du' = \frac{2 + \frac{1}{\beta}}{1 + \beta} du \quad (9)$$

when the object distance is very large, the amplification ratio of the image very small and we can assume it is

zero. In this case, $\frac{2+\frac{1}{\beta}}{1+\beta} \rightarrow \infty$ occurs. It can be seen in Equation (9) that du' is identical to a certain value when du is very small. (Incident beam is parallel.) It means that the parallel beam will be focused by telescope.

Equation (10) can be obtained by (2):

$$du'(s' - \Delta x) = sdu \quad (10)$$

(11) is obtained with consideration of (9):

$$\Delta x = s' - \frac{1+\beta}{2+\frac{1}{\beta}} s \quad (11)$$

Combine Equations (1) and (11), we get Equation (12):

$$dh' = du' \Delta x = \left(\frac{2+\frac{1}{\beta}}{1+\beta} s' - s \right) du \quad (12)$$

From the geometrical relationships of **Figure 1**, we have:

$$\Delta x du' = \Delta x' (u' + du') \quad (13)$$

According to Equations (9–13), we have Equation (14):

$$\Delta x' = \frac{\Delta x du'}{u' + du'} = \frac{\left(s' - \frac{1+\beta}{2+\frac{1}{\beta}} s \right) \times \frac{2+\frac{1}{\beta}}{1+\beta} du}{\frac{1}{\beta} u + \frac{2+\frac{1}{\beta}}{1+\beta} du} \quad (14)$$

According to the above equations, we build the curve showing the relationship between $\Delta x'$, the divergence, and the object distance, as well as the relationship between dh' , the divergence, and the objective distance. **Figure 2** shows the relationship between $\Delta x'$ and the divergence. The uncertainty of image distance $\Delta x'$ is proportional to the divergence of the incident beam; as a result, $\Delta x'$ becomes larger when the divergence of the incident beam becomes larger. And $\Delta x'$ is also relative to object distance. $\Delta x'$ becomes smaller at larger object distance. When object distance is 1000m (assume it is possible that the axis of the incident beam is parallel to the axis of telescope), uncertainty of image distance $\Delta x'$ is 1 millimeter at divergence of 1 mrad; if object distance is larger than 1000m, $\Delta x'$ is less than 1 millimeter. $\Delta x'$ is close to zero at object distance at ∞ . **Figure 3** shows the relationship between the uncertainty of the size of image disk (dh') and divergence of the

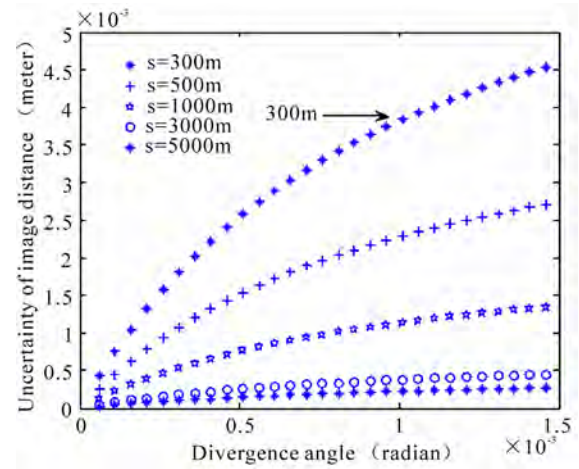


Figure 2. The relationship between $\Delta x'$ and divergence of incident beam

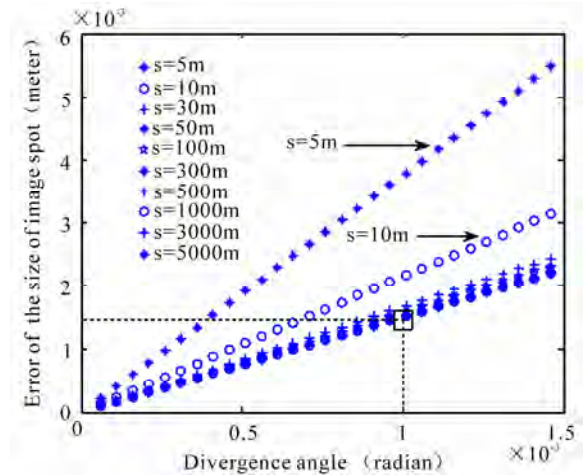


Figure 3. The relationship between dh' and divergence

incident beam. dh' is relative to object distance and is proportional to divergence of incident beam. dh' becomes larger at larger divergence of incident beam and becomes smaller at larger object distance.

3. Focus Size of Backscatter Light of a Lidar System

According to Equation (14), we can assume that the axis of the incident beam is parallel to the axis of the telescope in the case of $u \approx 0$, du is the divergence of the incident beam. In the case of large object distance (s is close to infinite), we put $\beta = \frac{s'}{s}$ into (14) to obtain

$\Delta x \rightarrow 0$. This indicates that the location of focus does not vary with the variation of divergence of incident

beam. In this case, we obtain $dh' = 2fdu$ by Equation (12), the uncertainty of the size of focus is double of focal length times divergence of incident beam. The size of focus is 0.3 millimeter at divergence of 0.1 mrad (mili-radian) at $f = 1.5m$. According to diffraction limitation (airy disk), the diffraction angle is about 10^{-5} rad (radian) if the diameter of laser beam is 10 millimeter, and the radius of the airy disk is about 0.015 millimeter. The actual size of focus is much larger than that of the airy disk; it is about 10~200 times of the airy disk.

Figure 4 presents the uncertainty of the location and the size of the focus. **Figure 5** corresponds to **Figure 4**, it is image disk at different image distance analyzed by ZEMAX software which is powerful, accurate and affordable software for all aspects of optical system design. The middle image disk 3 TSA (min) (Transverse spherical aberration) corresponds to the focus of the laser beam [5]. Compared **Figure 3** to **Figures 4** and **5**, **Figure 3** is analysis result by the above optical path, it shows the size of image disk relative to object distance; the image disk is smaller if the object distance larger; the smallest image disk is the size of focus, corresponding to object distance at infinity. From **Figures 4** and **5**, we can see that the image disk 3 is smaller than image disk 1, 2, 4, and 5; the image disk 3 correspond to the smallest Transverse spherical aberration, the focus spot. **Figure 3** coincides with **Figures 4** and **5** analyzed by ZEMAX software.

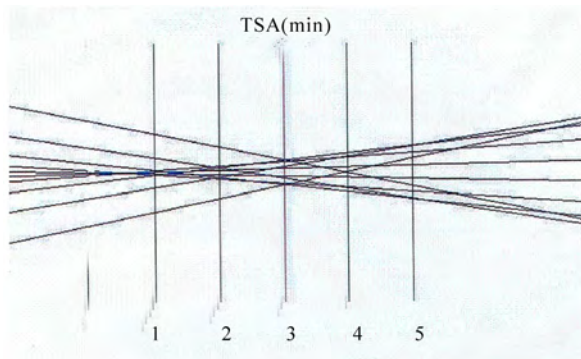


Figure 4. The optical path distribution near TSA

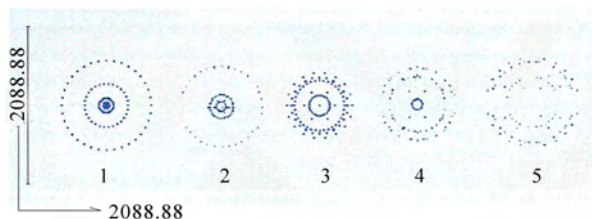


Figure 5. The image disks near TSA analyzed by ZEMAX software

4. Experiment

According to above analysis, the focal spot is the smallest image disk. In principle, the location of the focus of backscatter light of a Lidar system can be decided by focusing one laser beam with telescope, but it does not provide enough accuracy. We use three identical parallel laser beams that distributed in one circle symmetrically to accurately locate the focus of the Newton telescope. The design is shown in **Figure 6**. The He-Ne laser (Melles Griot company) beam is separated to three beams by two beam splitters (with about 50% transmission, about 50% reflection) and two reflect mirrors, the three beams are reflected respectively by three 45° reflect mirrors and transmit down vertically, the three 45° reflect mirrors distribute in one circle symmetrically. **Figure 7** shows the experimental setup: the He-Ne laser, the beam splitters, and the reflect mirrors are all fixed on an optical table with 50 cm length and 45 cm width, and the center of all mirrors and beam splitters are all at identical height to the optical table. The He-Ne laser beam was aligned to make all separated beams incident at the center of these optical components. The laser beams reflect at 45° incident angle and then transmit down vertically through the

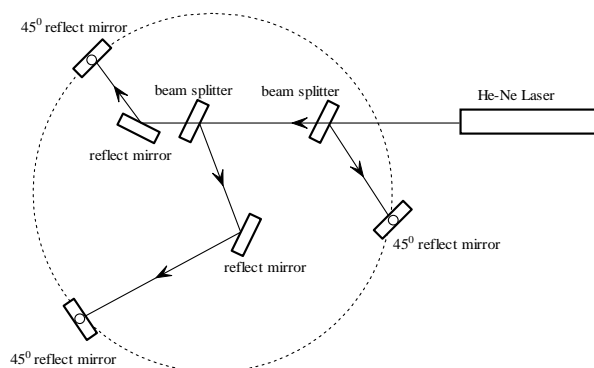


Figure 6. Schematic diagram for three parallel beams generation

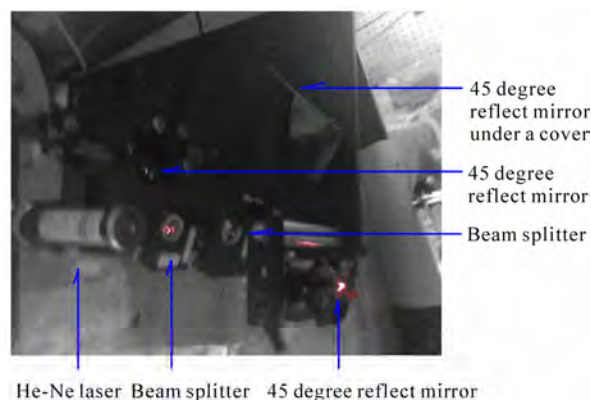


Figure 7. Experimental setup for three parallel beams generation

pinhole of the optical table. After finely beam alignment, the optical table with these optical components is fixed directly above the telescope at the height of 10 meters from the center of the primary mirror. The three beams transmit downwards vertically to the primary mirror of the telescope and focus at the focal points of the telescope.

5. Alignment of the Three Parallel Beams

In order to ensure the three beams are parallel to each other and transmit down vertically, we performed the alignment as follows. The optical table with the experiment setup is fixed at the top of a tower at the height of 4 meters. **Figure 8** is the setup of the tower fixed on the big optical table in the laboratory. We first aligned the He-Ne laser beam and the angle of the 45° reflect mirror to make the three beams transmit downward vertically by the pinhole of the optical table. The three beam spots on the big optical table in the laboratory should distribute in one circle. Then we performed the fine alignment. At the bottom of the tower, we put reflect mirror at the beam spot on the big optical table in the laboratory, to reflect the laser beam and make the beam transmit reversely on the optical path. We can observe the beam spot in the incident path and the beam spot in the reflect path by using lens paper in the optical path. We then finely aligned the optical components, and tried to move the lens paper along the optical path, to make the incident beam spot overlap with the beam spot in the reflect path, as shown in the **Figure 9**. It means that the incident beam overlaps with the reflect beam completely; in other word, the laser beam transmit downward vertically; We aligned the other two laser beams in the same way. It ensures the three beams are parallel to each other and transmit downward vertically.

After the alignment, the three laser beams are parallel to each other and transmit downward vertically. In this

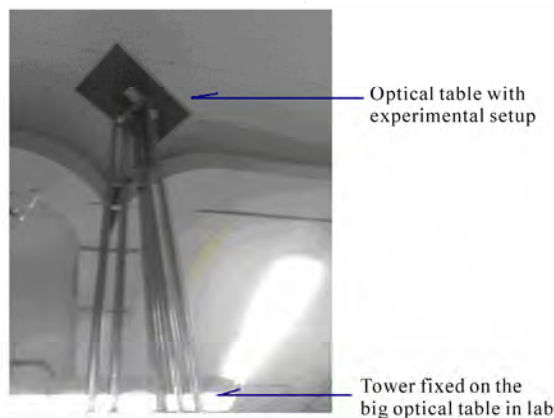


Figure 8. The tower for the three parallel beams alignment

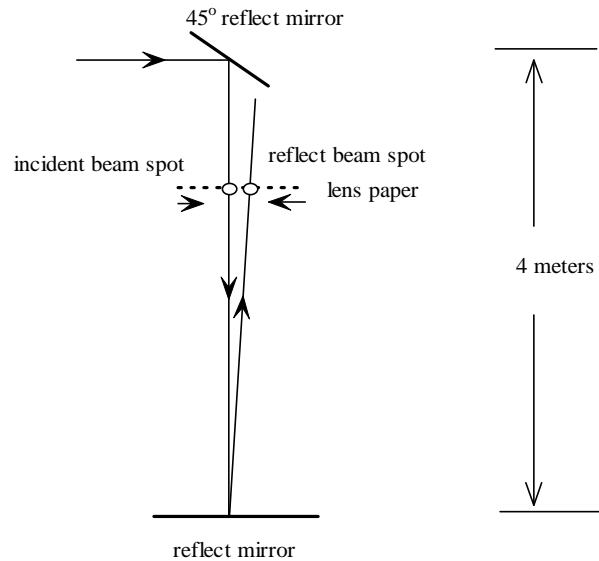


Figure 9. Schematic diagram for parallel beams alignment

case, fix the optical table on the roof directly above the telescope 10m high to the center of the primary mirror. The cavity length of the He-Ne laser is: $L = 30$ cm, and the wavelength is $\lambda = 0.6328\mu\text{m}$. According to the

divergence calculation equation [8]: $\theta = 2\sqrt{\frac{\lambda}{\pi L}}$, the di-

vergence angle is calculated as $\theta \approx 2.0 \times 10^{-3} \text{ rad}$. Thus, the diameter of the incident beam spot on the surface of primary mirror of the telescope is about 20 millimeters; the diameter of airy disk should be 0.0286 millimeter (if the focal length is 1.5 meter). Actually, according to the above analysis, the size of the focus is 3 millimeters, as shown in **Figure 3**, which is much larger than the size of the airy disk. The three laser beams transmit downward vertically, reflected by the primary mirror and secondary mirror of the telescope, and then focus at the focal spot of the telescope. The beam spot can be detected by using lens paper in the optical path, and distance between the three beam spots varies with the lens paper movement: the distance between the three beam spots becomes smaller while the lens paper moving toward the focus spot, eventually, the three beam spots exactly overlap at the focus spot. According to this experimental result (three beam spots overlap at the focus spot), we can locate the focus of backscatter light of a Lidar system.

6. Conclusions

According to this theoretic analysis, the uncertainty of focus location is close to zero when the backscatter light is from infinity; and the size of focus is relative to object distance and divergence of incident beam (corresponding

to the field of view of telescope). The relationship between the size of focus and divergence of backscatter light can be quantificationally described as $dh' = 2fdu$ which coincide with the analysis in reference [6]. Compared with the analysis result by ZEMAX software, this calculation is also quite reasonable. Therefore, we can exactly locate the focus and obtain the size of the focus of backscatter light of a Lidar system by combination of this calculation and experiment.

7. Discussion (Future Plan for Experiment Modification)

1) In the experiment of alignment of three parallel beams (shown in **Figures 8** and **9**), in order to make the reflect mirror on the big optical table in lab perfectly horizontal to the earth surface, we are going to use an oil cup instead of the reflect mirror to ensure the three beams exactly parallel and transmit down vertically.

2) According to the calculation in above paragraph, the divergence angle of He-Ne laser is about 2 mrad; to improve the beam quality of He-Ne laser, a beam expander should be housed in the optical path in front of He-Ne laser (shown in **Figures 6** and **7**) to reduce the divergence angle of He-Ne laser beam to increase the experimental accuracy.

8. Acknowledgements

Authors thank Prof. Barry Gross for great supports in this work.

REFERENCES

- [1] N. W. Cao, R. L. Collins, and C. F. Cahill, "An eye-safe Lidar for studies of urban ice fog," A Report Prepared under the Program, University Partnering for Operational Support (UPOS), Geophysical Institute, University of Alaska Fairbanks, January 2003.
- [2] Y. Suematsu, S. Tsuneta, K. Ichimoto, T. Shimizu, M. Otsubo, Y. Katsukawa, M. Nakagiri, M. Noguchi, T. Tamura, Y. Kato, H. Hara, M. Kubo, I. Mikami, H. Saito, T. Matsushita, N. Kawaguchi, T. Nakaoji, K. Nagae, S. Shimada, N. Takeyama, and T. Yamamuro, "The solar optical telescope of solar-B (Hinode): The optical telescope assembly," *Solar Physics*, No. 249, pp. 197–220, 2008.
- [3] I. Matsui, N. Sugimoto, Y. Sasano, and H. Shimizu, "Wind profiling by a conical-scanning time-correction Lidar," *Japanese Journal of Applied Physics*, Vol. 29, No. 2, pp. 441–444, February 1990.
- [4] P. Kokkalis, G. Georgoussis, A. Papayannis, D. Hatzidimitriou, J. Porteneuve, R. E. Mamouri, and G. Tsaknakis, "Optimization-through optical design-of a multi-wavelength fiber-based Raman-Lidar system in the near field for vertical aerosol measurements in the troposphere," *Proceedings of the 8th International Symposium on Tropospheric Profiling*, The Netherlands, October 2009.
- [5] G. Andersen, J. K. Brasseur, R. J. Knize, and P. Haris, "Raman and Rayleigh holographic Lidar," *Applied Optics*, Vol. 41, No. 9, pp. 1798–1804, 2002.
- [6] G. Chourdakis, A. Papayannis, and J. Porteneuve, "Analysis of the receiver response for a noncoaxial Lidar system with fiber-optic output," *Applied Optics*, Vol. 41, No. 15, pp. 2715–2723, 2002.
- [7] <http://www.answerbag.com/articles/how-to-view-the-moon-with-a-telescope/32b45360-b7f0-f3f8-5c5d-cc6c6e59fba0>
- [8] K. X. Yu and T. L. Jiang, "Laser theory and technology," Beijing Technology University Book Concern, pp. 195–196.

Design of the Control System about Central Signals in Electric Vehicle

Qianqian Zhang, Yan Wang, Tianming Yin

Electrical Engineering School, Beijing Jiaotong University, Beijing, China.
Email: zhang.q_0401@126.com, yanwang@mail.bjtu.edu.cn

Received December 1st, 2009; revised January 6th, 2010; accepted January 10th, 2010.

ABSTRACT

Based on the development demand of electric vehicles, this paper studies the communication network in electric vehicles based on CAN bus after analyzing the LCD (liquid crystal display) in electric vehicles and the status quo of research and development trend about communication network. This system uses TMS320LF2407 DSP as the controller of the control system about central signals. It has also developed the LCD system based on CAN bus and the experiment platform which is applied pure electric vehicles.

Keywords: CAN Bus, DSP, Electric Vehicle, LCD System, SCI

1. Introduction

Field bus is one hot topic in the developing technology in the automatic field. It is praised as Regional Network of Computers in the automatic field. Its appearance provides powerful technical support for DCS (Distributed Control System) to realize real-time and reliable data communication between each node. CAN (Control Area Network) belong to the category of field bus. It was developed by Germany BOSCH Company in early 1980s to solve data interchange between numerous control and test instruments in vehicles. Because of its outstanding reliability, real-time and flexibility, CAN bus is approved and applied in the industry. And it became the international standard and industry standard formally in 1993 [1]. It also is praised as one of the most promising field buses. The application of bus technology with CAN as the representative in vehicles not only reduces the harness of the car but also increases the reliability of the car.

Motor meter is the alternation interface between the user and the vehicle. It can provide necessary information such as operating parameters, warning and mileage for drivers. Therefore, motor meter is the requisite part. However, traditional meter can only provide a small number of necessary data information for drivers. This is far from the requirement of new technology and high speed in modern vehicles. Motor meter should not only display information simply but also control all kinds of operation conditions of the vehicle through the monitoring of parameters in every part in the vehicle. With the development of modern electron technology, meter with

multifunction, high accuracy, high sensitivity, direct and reliable reading and picture display has been applied in the vehicle gradually. Therefore, electronic instrument will replace conventional electromechanical instrument gradually.

This paper applies CAN bus technology in the control system of electric car and combines it with LCD system. It has realized to improve the performance of the control system in the electric vehicle.

2. The Application of Can Bus in Electric Vehicles

CAN bus which belongs to the category of field bus is a kind of serial communication network which supports distributed control or real-time control effectively.

Currently, many existing auto network standards have different emphasis about their functions. SAE traffic network committee classified the data transmission network into three kinds including A type, B type and C type for convenient study, design and application, design and application [2]. A type turns towards Low Speed Network controlled by sensors or actuators. The bit rate of data transmission usually is only 1~10kb/s. They are mainly used to control the electric windows, seat adjust and lamplight illumination. B type turns toward the moderate speed network of data sharing between independent modules. The bit rate usually is 10~100kb/s. They are mainly used in systems such as information centre of electronic vehicle, fault diagnosis, instrument display and air bag to reduce redundant sensors and other

electronic units. C type turns toward the multipath transmission with high speed and real-time closed-loop control. The highest bit rate is 1Mb/s. They are mainly used in systems such as suspension control, traction control, advanced motor control and ABS to simplify the distributed control and the harness further. As so far, only CAN protocol satisfy the demand of C type in the auto control LAN.

3. Design of the Vehicle Communication System Based on Can Bus

3.1 Schematic Diagram of the System

This system is mainly made up of control modules, motor drive module, BMS module, service module and meter display module. TMS320LF2407 is the processor [3]. Because there is a controller of CAN, only one transceiver of CAN is needed. The information channel between each module will be realized through CAN bus. Except for the sending and receiving of instructions, the basic status information of vehicles is the requisite data obtained by most control modules. Control modules send data to the bus using broadcast mode. If all control units send data to the bus at the same time, it will cause data collision in the bus. Therefore, CAN bus protocol proposed the bus arbitration which used identifier to identify the priority of data. **Table 1** presents data types that will be received or sent by ECU in electric vehicles and the sharing of other units about these information.

3.2 CAN Bus Design

3.2.1 CAN Bus

The gross structure of CAN bus shows as **Figure 2**. There are two resistances with the value of $120\ \Omega$ in each side

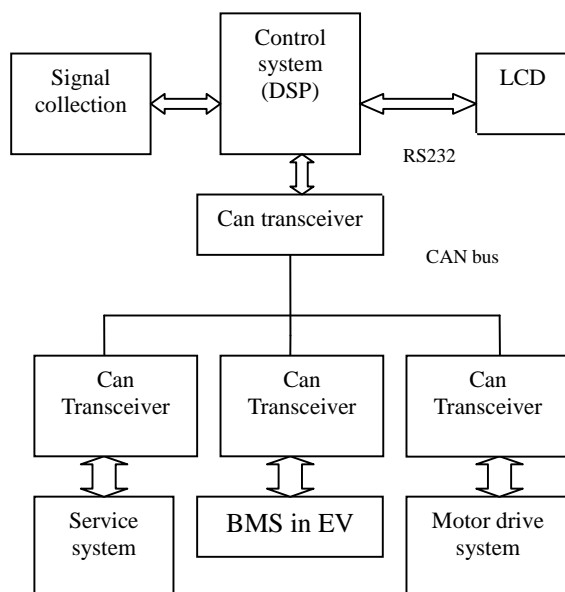


Figure 1. Schematic diagram

Table 1. Data types sent or received by ECU

Signal type	Central signal control	Motor drive control	Battery management module	Service facilities inside cars	LCD unit
Motor speed	R&T	T			R
Motor temperature	R&T	T			R
Regenerative braking		In			
Motor error	R&T	T			R
Forward /reverse	T	R			
Speed	R&T	T			R
Remaining battery power	R&T		T		R
Battery charging status	R&T		T		R
Temperature inside cars	R&T			T	R
LCD switching	T				R

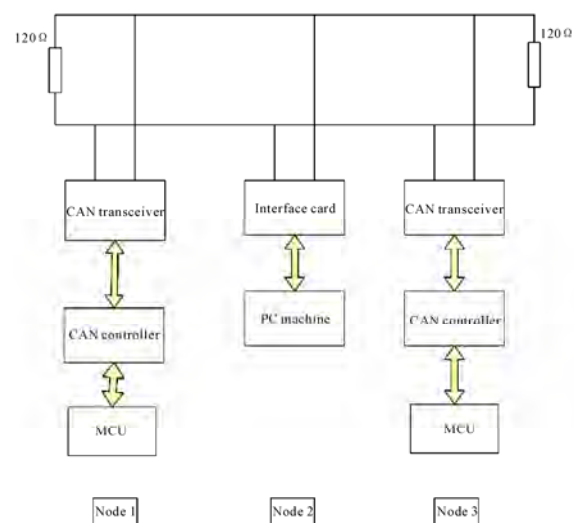


Figure 2. Structural diagram of CAN bus system

of the bus. They are resistances matching the bus. They can increase the stability and the capacity of resisting disturbance of bus transmission and reduce the error rate in the process of data transmission [4]. The node structure of CAN bus can be classified into two kinds: the first is to connect the CAN adapter with PC machine to realize the communication between the host computers and CAN bus; the other is made up of microcontroller, CAN controller and CAN actuator. It transmits data with CAN bus as one kind of node. In this system, CAN controller is SJA1000 produced by Philips as the send and receive buffer to realize the data transmission between the main

controller and the bus [5]; CAN transceiver is PCA82C250 chip which is the interface of CAN controller and physical bus. It can provide differential send ability for the bus and differential receive ability for the CAN controller.

3.2.2 CAN Bus Transceiver PCA82C250

PCA82C250 is the interface of CAN protocol controller and physical bus. It can provide differential send ability and receive ability of the bus. Different operation modes can be chose through pin 8 (RS): high speed, slope control and stand by. In the operation mode of high speed, the output transistor of the transmitter conducts or cuts off as soon as possible. In this mode, no measure is needed to limit the rising and descending slope. UTP (unshielded twisted pair) or parallels can be used as the bus in the situation of lower speed or shorter bus. The rising and descending slope should be limited to reduce RF interference. And they can be controlled by the earth resistance in pin 8. The operation mode of slope is used in this system. In the network made up of PCA82C250, when the input in the TXD side of PCA82C250 is high level, its output sides CANH and CANL are all in high-impedance state in which PCA82C250 has no influence on the whole network. Then, this node is in concession state; when the input of TXD is low level, CANH and CANL output high level and low level respectively. Then this node decides the nature of the transmission data in the whole network. The output level of RXD in PCA82C250 is consistent with the level of RXD which plays the dominating role in the network.

The circuit of CAN interface is shown as **Figure 3**.

In this figure, B0505LD is the Power Isolated Module which can isolate the power in the bus from the power supply of DSP and play the role of protection. In the auto environment, voltage often changes instantly. If there is protection measure, it is very possible that electronic devices can be destroyed by the instant change of the voltage. In order to suppress the instant change of voltage, capacitance can be added between CAN bus and the ground wire to filter out noise and make signals more stationary.

4. Design of Color LCD

4.1 Main Display Function and Plan

Comprehensive display interface: set the state of speed, mileage, alarm message, battery state, whole power of batteries, whole voltage of batteries and SOC [6].

Combined transformation interface: in order to display the information of electric motor and battery, both interface of motor state and interface battery will be set. They will display information of the two modules respectively in detail and give alarms.

Information display methods include analog display (change and trend), digital display (direct and correct),

graphic symbol display (vivid) and text display (implication) [7].

Expected display interface of comprehensive information is shown as **Figure 4**: vehicle speed, motor speed, remaining power of batteries and fault information will be displayed in this interface. At the bottom of the screen, the interface will be switched to information interface of battery, electric motor and service facilities respectively.

4.2 Program Design of Serial Communication of LCD Module

LCD adopts standard RS232 communication interface and works in serial interface mode. The receiver and transmitter of SCI is double buffering. Each has its separate enabling and interruption flag bit. Both can work alone in the full-duplex mode at the same time. SCI uses even parity check, overtime detection and error frame detection to ensure correct transmission of data. Two external pins of SCI including SCITXD and SCIRXD can be used as common I/O when they are not used in the communication. The subprogram of serial communication is shown as **Figure 5**.

After disabling all interruptions and clearing interrupt

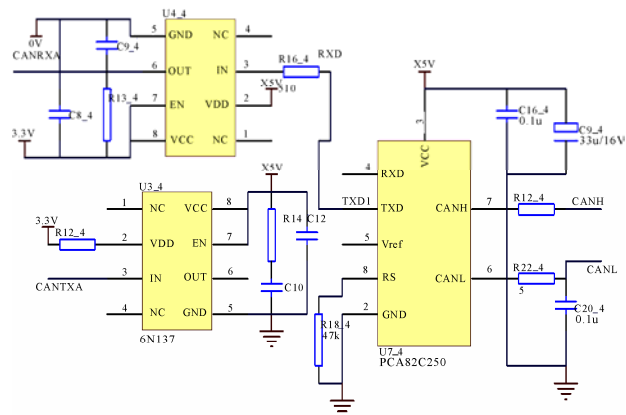


Figure 3. Interface circuit of TMS320LF2407

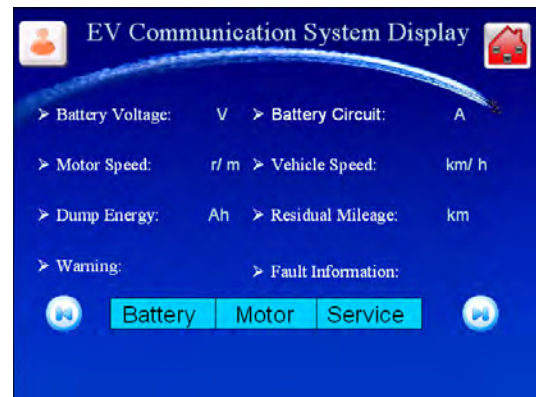


Figure 4. Display interface of comprehensive information

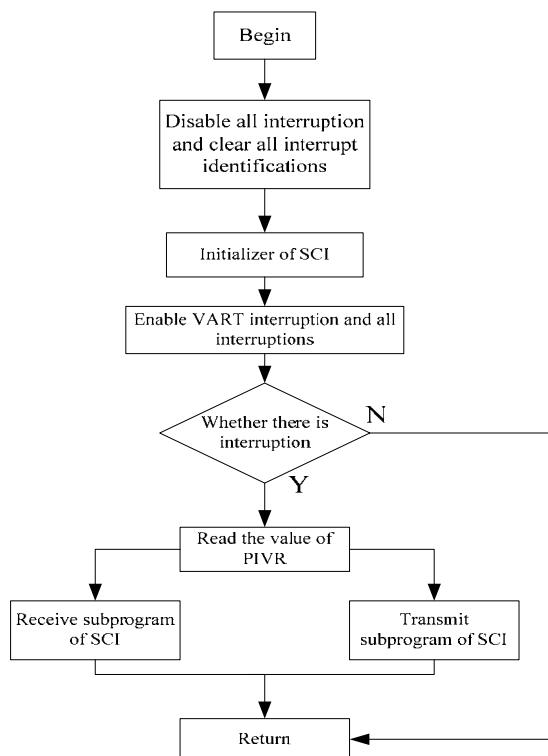


Figure 5. Flow chart of serial communication subprogram

identifications, the procedure will start the initializer of SCI which includes the setting of communication controller SCICCR of serial communication interface. For example, one stop bit, disable parity check, idle line and multiprocessor mode and 8 bits character. After the initializer, SCI interruption INT5 will be enabled. When the interruption is coming, judge the value of the register PIVR of the interrupt vector. If PIVR is 6, then receiving interruption happened and receiving service program will be executed; if PIVR is 7, transmitting interruption happened and transmitting service program will be executed.

5. Experiment Results

The physical connection diagram on the test bench is shown as **Figure 6** in which the upper is the LCD; the left is the BMS module; the right is the control system about central signals with DSP as the core chip; the UTP between the two modules is the CAN bus.

The node of the host computer is made up of CAN interface card, PC machine and monitoring software. Among them CAN interface card is one kind of unintelligent adapter of CAN developed by Beijing Run Quan scientific and technological company. It is a kind of unintelligent adapter connecting CAN communication protocol with PC machine. Besides, it can satisfy the requirement of high real-time of the network. Meters with CAN communication interface and controlling equipments in industrial field can be monitored through CAN card.

The data received by CAN bus can be displayed on the color LCD in real time. The color LCD can dynamically display information such as the speed, mileage, whole power of batteries, temperature of the battery, remaining power and battery state in real time. The result is shown in **Figure 7**.


To get the information of EV in detail, the system interface will be available by pressing button , the display interface is shown as **Figure 8**.



Figure 6. Test system connection

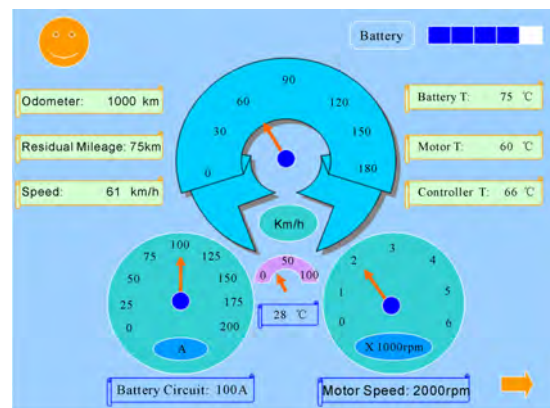


Figure 7. Information in the dashboard

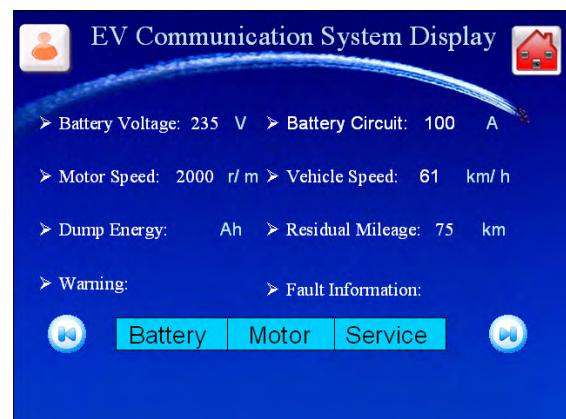



Figure 8. Liquid crystal display of communication system


In this experiment, some analog signals are given to the controller (DSP) in the control system about central signals. Through SCI communication, they are all shown in the LCD successfully as shown in **Figure 8**.

The Dashboard interface will be available again by pressing button .

The battery interface will be available by pressing button “Battery”, the display interface is shown as **Figure 9** and **Figure 10**.

As shown in **Figure 9** and **Figure 10**, there are 20 batteries in EV. The monomer battery voltage can be got through A/D sampling. Because the battery current will not change frequently, the current information will be only shown in the dashboard interface. This is realized successfully shown as **Figure 10**. However, the dump power is unable to obtain currently. In the future, it can be obtained through some algorithms.

Similarly, the motor interface and service interface will be available by pressing button “Motor” and “Service” respectively. The display interface is shown as **Figure 11** and **Figure 12** respectively.

Similarly, the dashboard interface will be available again by pressing .

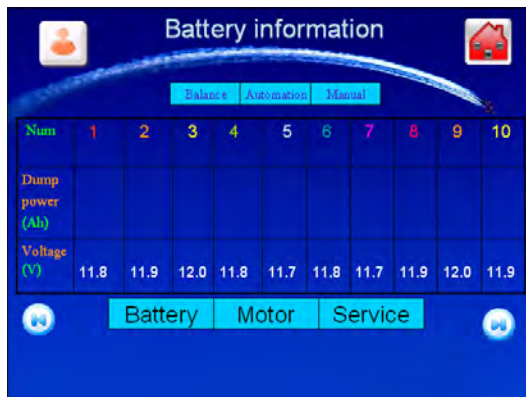


Figure 9. Battery information 1

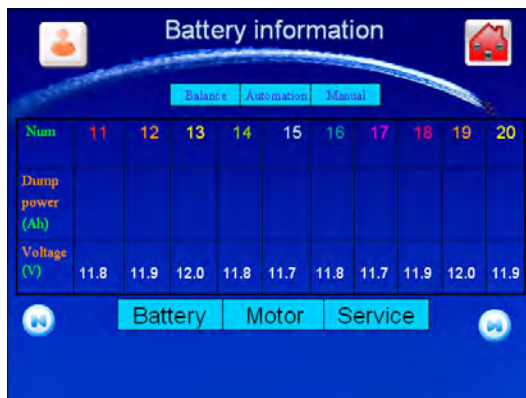


Figure 10. Battery information 2



Figure 11. Motor information

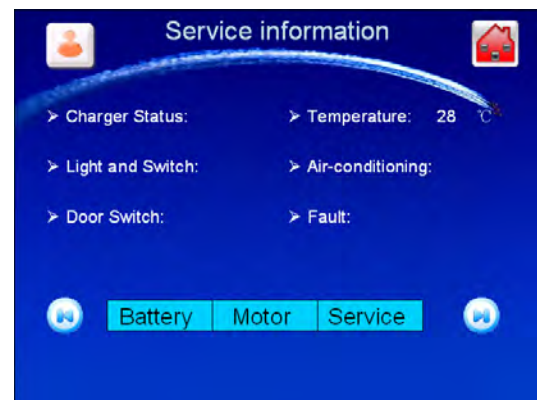


Figure 12. Service information

Currently, how to dispose some information about light and switch, charger status and door switch is still in the study.

6. Conclusions

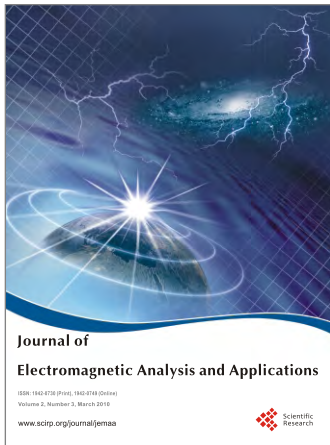
This paper introduced the features of CAN bus and its application in electric vehicles and designed the nodes of control system in the whole electric vehicle based on CAN bus. Finally it displayed the state information of the vehicle using liquid crystal display.

This paper also did corresponding experiment design on the electronic control system in the whole vehicle. Besides, it record and analyzed the results of the experiment. The results proved that this system was stable. The output waveform is stable of each node in CAN bus and the communication with electric motor and battery is normal. The information can be displayed on the liquid crystal screen. These satisfy the demands of the experiment.

REFERENCES

- [1] SAE J1939-13, “Off-board diagnostic connector,” Society of Automotive Engineers, USA, July 1999.
- [2] SAE J1939-31, “(R) Network layer,” Society of Automotive Engineers, USA, December 1994.

- [3] R. S. Hourani, "A performance analysis framework for the design of DSP systems," Dissertation Abstracts International, Vol. 69, No. 4, p. 2517, 2008.
- [4] G. P. Liu, "Anticipating system-level electromagnetic interference using numerical methods and measurement techniques," Dissertation Abstracts International, Vol. 65, No. 8, p. 4195, 2004.
- [5] H. Huang, "Electrical two speed transmission and advanced control of electric vehicles," Dissertation Abstracts International, Vol. 60, No. 7, p. 3455, 1998.
- [6] F. Fang, "A solid state relay battery management system for series connected batteries," Dissertation Abstracts International, Vol. 63, No. 8, p. 3640, 2002.
- [7] F. S. Zhou, "Reflective and transfective liquid crystal displays," Dissertation Abstracts International, Vol. 67, No. 1, p. 341, 2005.



Journal of Electromagnetic Analysis and Applications (JEMAA)

ISSN: 1942-0730 (Print), 1942-0749 (Online)
www.scirp.org/journal/jemaa

JEMAA is a professional journal in the field of electromagnetic analysis, testing and application. The goal of this journal is to provide an international platform for engineers and academicians all over the world to promote, share, and discuss various new issues and developments in the field of electromagnetic. This journal is edited to encourage deeper understanding and greater effectiveness in theory analysis, testing, numerical calculation and engineering application that relevant electromagnetic fields.

Editors-in-Chief

Prof. James L. Drewniak
Prof. Yuanzhang Sun

Electrical Engineering and Materials Science and Engineering, Missouri-Rolla, USA
School of Electrical Engineering, Wuhan University, China

Subject Coverage

JEMAA publishes four categories of original technical reports: papers, communications, reviews, and discussions. Papers are well-documented final reports of research projects. Communications are shorter and contain noteworthy items of technical interest or ideas required rapid publication. Reviews are synoptic papers on a subject of general interest, with ample literature references, and written for readers with widely varying background. Discussions on published reports, with author rebuttals, form the fourth category of JEMAA publications. Topics of interest include, but are not limited to:

- Electromagnetic Numerical Analysis
- Multiphysics Coupled Problems
- Electromagnetic Inverse Problems
- Electromagnetic Structure Optimization
- Test Electromagnetic Analysis Method
- Workshop Benchmark Problems
- Electromagnetic Devices
- Electromagnetic Compatibility
- Electromagnetic Nondestructive Testing
- Electromagnetic Material Modelling

Notes for Intending Authors

Submitted papers should not be previously published nor be currently under consideration for publication elsewhere. Paper submission will be handled electronically through the website. All papers will be peer reviewed. For more details about the submissions, please access the website.

Website and E-Mail

<http://www.scirp.org/journal/jemaa>

jemaa@scirp.org

TABLE OF CONTENTS

Volume 2 Number 3

March 2010

A Microwave-Based Invisible “Watermarking” Emulated by an Embedded Set of Electromagnetic Material in a Plastic Card	
P. Neelakanta, S.-H. Lim.....	121
The Additional Criterion for the Determination of the Time of Minimum of a Solar Cycle	
H. I. Abdussamatov.....	128
Modeling of the Earth’s Planetary Heat Balance with Electrical Circuit Analogy	
H. I. Abdussamatov, A. I. Bogoyavlenskii, S. I. Khankov, Y. V. Lapovok.....	133
Analysis of the Electromagnetic Pollution for a Pilot Region in Turkey	
Ö. Genç, M. Bayrak, E. Yaldiz.....	139
Modeling of Multi-Pulse VSC Based SSSC and STATCOM	
P. Zuniga-Haro, J. M. Ramirez.....	145
A Fundamental Equation of Thermodynamics that Embraces Electrical and Magnetic Potentials	
S. Abdel-Hady.....	162
Energy and Momentum Considerations in an Ideal Solenoid	
S. M. AL-Jaber.....	169
Exact Solutions of Equations for the Strongly-Conductive and Weakly-Conductive Magnetic Fluid Flow in a Horizontal Rectangular Channel	
M. J. Li, X. R. Zhang, H. Yamaguchi.....	174
A New Analysis Method for Locating the Focus and for Estimating the Size of the Focus of the Backscatter Light of a LIDAR System	
N. W. Cao, W. Y. Wang, Y. H. Wu, F. Moshary, Z. R. Chen, J. S. Huang.....	183
Design of the Control System about Central Signals in Electric Vehicle	
Q. Q. Zhang, Y. Wang, T. M. Yin.....	189

